Preclinical evaluation of nanoparticle enhanced breast cancer diagnosis and radiation therapy

Dissertation

for the award of the degree

“Doctor rerum naturalium” (Dr. rer. nat.)

of the Georg-August-Universität Göttingen

within the doctoral program Molecular Medicine

of the Georg-August University School of Science (GAUSS)

submitted by

Jonas Albers

from Volkmarsen

Göttingen 2021

Members of the Thesis Committee:

Supervisor:	Prof. Dr. med. Frauke Alves Translational Molecular Imaging, Max-Planck-Institute for Experimental Medicine, Goettingen, Germany and Institute of Diagnostic and Interventional Radiology, University Medical Center Goettingen, Goettingen, Germany and Clinic for Hematology and Medical Oncology, University Medical Center Goettingen, Goettingen, Germany
Second member of the Thesis Committee:	Prof. Dr. med. Dörthe M. Katschinski Institute of Cardiovascular Physiology, University Medical Center Goettingen, Goettingen, Germany
Third member of the Thesis Committee:	Prof. Dr. rer. nat. Hubertus Jarry Deptartment of Research, Animal Welfare Officer, University Medical Center Goettingen, Goettingen, Germany

Date of Disputation: 22.06.2021

AFFIDAVIT

By this I declare that I independently authored the presented thesis: “Preclinical evaluation of nanoparticle enhanced breast cancer diagnosis and radiation therapy” and that I did not use other auxiliary means than indicated. Paragraphs that are taken from other publications, by wording or by sense, are marked in every case with a specification of the literary source. Furthermore, I declare that I carried out the scientific experiments following the principles of Good Scientific Practice according to the valid “Richtlinien der Georg-August-Universität Göttingen zur Sicherung guter wissenschaftlicher Praxis”.

_____

Jonas Albers

Göttingen, April 2021

Publications

Brun, F., Trapani, V.D., **Albers, J**., Sacco, P., Brombal, L., Dreossi, D., Rigon, L., Longo, R., Mittone, A., Dullin, C., Bravin, A., Delogu, P., 2020. Single-shot K-Edge Subtraction X-ray discrete Computed Tomography (KES-CT) with a polychromatic source and the Pixie-III detector. *Physics in Biology and Medicin*e 14, 8.

Albers, J., Svetlove, A., Alves, J., Kraupner, A., Lillo, F., Markus, A., Tromba, G., Alves, F., Dullin, C., 2021. Elastic transformation of histological slices allows precise co-registration with microCT data sets for a refined virtual histology approach. Scientific Reports accepted for publication

Abstract

Triple negative breast cancer (TNBC) is an aggressive type of cancer which makes up 15-20% of all newly diagnosed cases, lacking the main target molecules for tumor specific treatment. Surgery or systemic therapy by chemotherapy are frequently used in the clinic and combined with radiation therapy to improve locoregional control in breast cancer patients after surgery. With a poor prognosis, there is a clear need to explore new treatment options for TNBC. The aim of the here presented PhD project was to evaluate the feasibility to enhance the biological effect of radiation therapy and increase tumor contrast for diagnosis by applying an in vivo microCT imaging system in combination with barium nanoparticles (BaNPs) in a pH8N8 WAP-T-NP8 mouse model for TNBC. Characterization of the BaNPs revealed strong x-ray attenuation and no toxic effects in different cancer and normal cell lines. Furthermore, irradiation of cancer cells using low energy x-rays in the keV range by a microCT resulted in a significant reduction on colony formation capability. In vitro, this low energy irradiation effect on clonogenic tumor cell survival was enhanced in the presence of BaNPs. Next, a subcutaneous lung cancer mouse model in immunodeficient mice and an orthotopic syngeneic mouse model for breast cancer was applied for further in vivo evaluation. Once the treatment plan was optimized regarding the applied x-ray doses and the frequency of irradiation, low energy radiation therapy within a classical in vivo microCT significantly reduced tumor growth or even resulted in shrinkage of the tumors without visible side effects and weight loss in comparison to untreated controls. However, the intratumoral application of BaNPs was not able to increase the irradiation effect on tumor growth kinetics. This might be in part due to inhomogeneous distribution of BaNPs within the tumor observed by microCT imaging. K-edge subtraction imaging as well as x-ray fluorescence of explanted tumor samples confirmed these findings. To localize the BaNPs in 3D to specific sites within the tumor environment and to detect morphological alterations within the tumor due to irradiation in proximity to BaNPs an ex-vivo imaging based analytic platform was established, utilizing co-registration of microCT and histology data. This imaging approach co-localized BaNPs with CD68 positive phagocytic cells and revealed a non-uniform distribution of the BaNPs within the tumor, however with no signs of locally enhanced radiation effects. Furthermore, antibody functionalized BaNPs were generated for systemic application. Analysis of biodistribution revealed that EpCAM labeled BaNPs did not reach the tumor after intra-venous administration, but accumulated in liver and spleen, demonstrated by a strong CT contrast within these organs.

In summary, I showed that low energy radiation therapy by applying an in vivo microCT significantly reduced tumor volumes in comparison to untreated tumors in a syngeneic breast cancer tumor mouse model resembling TNBC. However, BaNPs while enhancing the effectiveness of irradiation on tumor cells in vitro, did not improve the irradiation effect on tumor growth in vivo.

Zusammenfassung

"Triple Negative Breast Cancer" (TNBC) is eine besonders agressive Form von Brustkrebs die 15-20% der diagnostizierten Fälle ausmacht und denen die Hauptzielmoleküle für die tumorspezifische Behandlung fehlen. Eine Operation oder systemische Therapie mittels Chemotherapie wird häufig in der Klinik eingesetzt und mit Strahlentherapie kombiniert, um die lokoregionale Kontrolle bei Brustkrebspatientinnen nach der Operation zu verbessern. Aufgrund der mit TNBC verbundenen schlechten Prognose besteht die Notwendigkeit, neue Behandlungsoptionen für zu untersuchen. Die hier vorgestellte Doktorabeit hatte zum Ziel eine solche Alternative: Niederenergetische Strahlentherapie unter Nutzung eines klassichen CT Systems in Kombination mit Barium Nanopartikeln (BaNPs) zur Verstärkung des Effekts zu etablieren. Diese Partikel sollen zusätzlich den CT Kontrast des Tumors erhöhen und somit seine Darstellung erleichtern. Dieses Konzept galt es in-vivo in einem pH8N8 WAP-T-NP8 Mausmodell für TNBC zu evaluieren.

Die neu geschaffenen BaNPs zeigten keinerlei toxische Effekte auf verschiedene Zelllinien und einen verstärkten Röntgenkontrast in-vitro. In Kombination mit Röntgenstrahlung im niederenergetischen keV-Bereich aus einem mikroCT wurde eine signifikante Reduktion der Poliferationsrate von pH8N8 Tumorzellen erzielt, die sich in einer eingeschränkten Fähigkeit zum Bilden von Kolonien manifestierte. Als nächstes wurden ein subkutanes Lungenkrebs-Mausmodell bei immundefizienten Mäusen und ein orthotop-syngenes Mausmodell für Brustkrebs zur weiteren In-vivo-Bewertung angewendet. Sobald der Behandlungsplan hinsichtlich der angewendeten Röntgendosen und des Bestrahlungsintervalls optimiert war, reduzierte eine energiearme Strahlentherapie innerhalb einer klassischen in vivo Mikro-CT das Tumorwachstum signifikant oder führte sogar zu einer Schrumpfung der Tumoren ohne sichtbare Nebenwirkungen und Gewichtsverlust in Vergleich mit unbehandelten Kontrollen. Die intratumorale Anwendung von BaNPs konnte jedoch den Bestrahlungseffekt auf die Tumorwachstumskinetik nicht erhöhen. Dies könnte teilweise auf die inhomogene Verteilung von BaNPs innerhalb des Tumors zurückzuführen sein, die durch Mikro-CT-Bildgebung beobachtet wurde. „K-edge subtraction imaging" und „x-ray fluorescence imaging" angewendet an explantierten Tumoren bestätigten diese Ergebnisse. Um die BaNPs in 3D an bestimmten Stellen innerhalb ihrer Tumorumgebung zu lokalisieren und morphologische Veränderungen innerhalb des Tumors aufgrund von Bestrahlung in der Nähe von BaNPs zu erkennen, wurde eine auf Ex-vivo-Bildgebung basierende Analyseplattform eingerichtet, bei der Mikro-CT- und Histologiedaten fusioniert wurden. Dieser bildgebende Ansatz lokalisierte

BaNPs zusammen mit CD68-positiven Phagozytenzellen und zeigte eine ungleichmäßige Verteilung der BaNPs innerhalb des Tumors, jedoch ohne Anzeichen lokal verstärkter Strahlungseffekte. Darüber hinaus wurden Antikörper-funktionalisierte BaNPs zur systemischen Anwendung erzeugt. Die Analyse der Bioverteilung ergab, dass EpCAM-markierte BaNPs nach intravenöser Verabreichung den Tumor nicht erreichten, sondern sich in Leber und Milz ansammelten, was durch einen starken CT-Kontrast dieser Organe gezeigt wurde.

Zusammenfassend konnte ich zeigen, dass eine Strahlentherapie mit niedriger Energie durch Anwendung eines in vivo Mikro-CT das Tumorvolumen im Vergleich zu unbehandelten Tumoren in einem syngenen Brustkrebs-Tumor-Mausmodell, das TNBC ähnelt, signifikant reduzierte. BaNPs verbesserten zwar die Wirksamkeit der Bestrahlung von Tumorzellen in vitro, verbesserten jedoch nicht den Bestrahlungseffekt auf das Tumorwachstum in vivo.

Table of content

List of figures

List of tables

List of abbreviations

2D	two dimensional
3D	three dimensional
Ab	antibody
AEC	aminoethylcarbazole
AI	artificial intelligence
ANOVA	analysis of variance
ATP	adenosine triphosphate
AuNP	gold nanoparticle
BaNPs	barium sulphate-based nanoparticles
BCS	breast-conserving surgery
BLI	bioluminescence imaging
BW	body weight
CAD	computer assisted diagnosis
CFA	colony forming assay
CMV	cytomegalovirus
csv	comma separated values
CT	computed tomography
DNA	deoxyribonucleic acid
EDTA	ethylenediaminetetraacetic acid
eGFP	enhanced green fluorescent protein
EGFR	epidermal growth factor receptor
EM	electron microscopy
EpCAM	epithelial cell adhesion molecule
EPR	enhanced permeability and retention
ER- α	estrogen receptor alpha
ERBB2	Erb-B2 receptor tyrosine kinase
EtOH	ethanol
FACS	fluorescence-activated cell sorting
FBP	filtered back projection
FCS	fetal calf serum
FOV	field of view
HD	high dose
HE	hematoxylin-eosin
HR	hormone receptor
i.p.	intraperitoneally
i.v.	intraveneously

IHC	immunohistochemistry
KES	k-edge subtraction imaging
LD	low dose
LINAC	linear accelerator
LSM	light sheet microscopy
MRI	magnetic resonance imaging
MTS	Masson Trichrome staining
NP	nanoparticle
OD	optical density
ON	over night
pAb	primary antibody
PBI	propagation-based imaging
PBS	phosphate-buffered saline
PCR	polymerase chain reaction
PEG	polyethylene glycol
PFA	paraformaldehyde
PR	progesterone receptor
Rb1	retinoblastoma protein-1
ROS	reactive oxygen species
RT	radiation therapy
sAb	secondary antibody
SDD	sample-to-detector distance
SRμCT	synchrotron radiation microCT
SV40	simian virus 40
SYRMEP	SYnchrotron Radiation for MEdical Physics
T-Ag	large T antigen
TAM	tumor associated macrophage
TIE	transport of intensity equation
TLD	thermoluminescence dosimeters
TNBC	triple negative breast cancer
TNM	Tumor-, Node-, Metastasis classification
Tp53	tumor protein p53
XRF	x-ray fluorescence
xVH	x-ray based virtual histology

1 Introduction

1.1 Breast cancer

Cancer is the 2nd leading cause of death worldwide. Breast cancer is by far the most common cancer type causing about 612.000 deaths per year worldwide[1]. The main risk factor for women to develop breast cancer is age[2]. Further risks are low parity, short breastfeeding phase and a long period from puberty to menopause[3,4]. There is increasing evidence that hormonal contraception can also increase the risk of breast cancer in certain cases[5,6]. These risk factors explain that women in industrialized countries are more likely to develop breast cancer[7]. In order to select the best possible therapy, the breast tumor must be fully characterized. Tumor classification includes the histopathological assessment and differentiation of breast carcinomas in grade one (G1, well differentiated), grade two (G2, moderately differentiated), grade three (G3, poorly differentiated) or grade four (G4, undifferentiated metastatic)[8]. In addition, the tumor is classified in the TNM system by the following three main criteria: I) the size and spread of the primary tumor (T), II) the absence or presence of local or adjacent lymph node metastases (N), and III) the presence of distant metastases (M)[9]. Figure 1 shows the large variability in molecular subtypes of breast cancer. Molecular biological methods enable the tumors to be further characterized by determining the Erb-B2 receptor tyrosine kinase (ERBB2), estrogen receptor alpha (ER-α) and progesterone receptor (PR) presence in connection with the molecular subtypes based on gene expression profiles: I) Luminal A, II) Luminal B, III) basal-like and IV) normal-like[10]. In 50–75% of the cases, the result of histological assessment is an invasive ductal carcinoma, followed by invasive lobular carcinoma in 5–15% of the cases. The remaining breast tumors are characterized by rare histologies[11]. The ER-α and PR, summarized here as hormone receptors (HR), are expressed in around 70% of invasive breast cancers[12]. Between 15–20% of breast cancers show increased activity or overexpression of the human epidermal growth factor receptor 2 (ERBB2), which is also known under the name HER2/neu and, if left untreated, are associated with a poor prognosis[13].

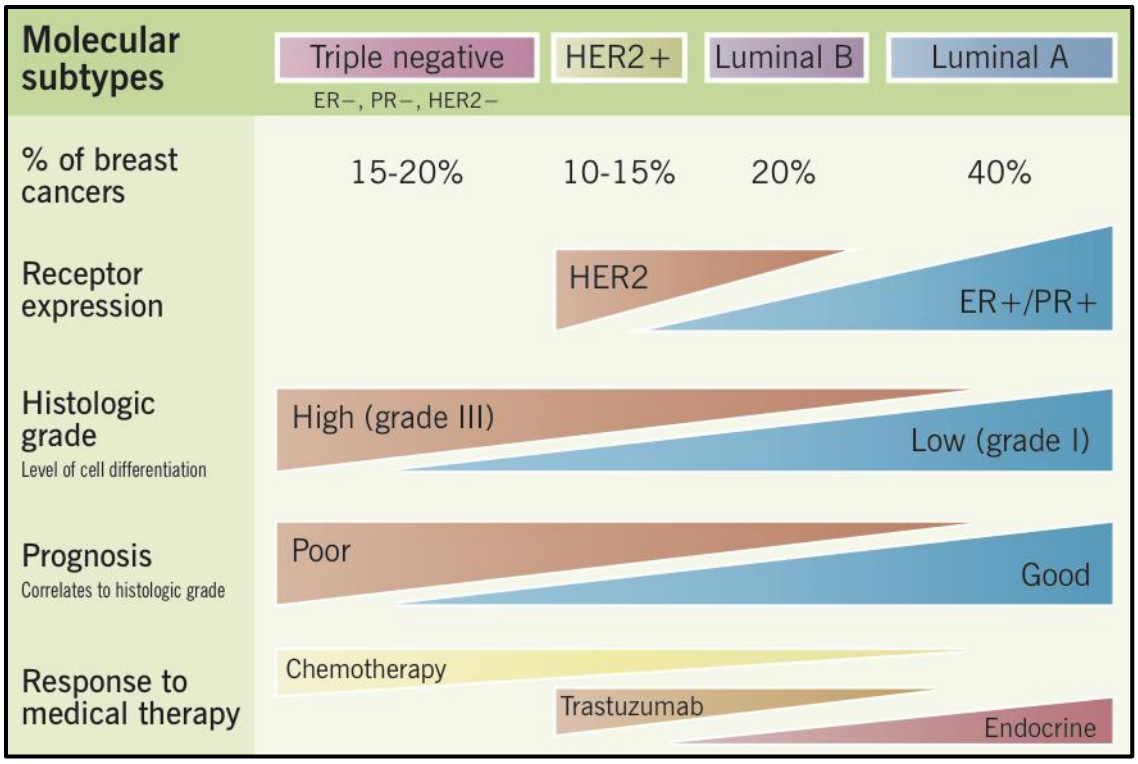

Figure 1: ***Molecular Subtypes of breast cancer***

Adapted from Eric Wong and Jenna Rebelo[14]

1.2 Triple negative breast cancer

Fifteen percent of all breast cancers, that lack the aforementioned receptors, are called triple negative breast cancers (TNBC)[15]. Thus, therapies specifically targeting the activity of ER-, PR- or HER2-receptors are inappropriate. TNBC has a mortality rate of 40% (within the first 5 years) versus ≤10% for all breast cancers and metastases in 46% of patients. It is a breast cancer type with a very poor prognosis, which occurs frequently in young and middle adulthood[16]. Patients with TNBC have a high risk of distant relapse (metastasis) occurring during the first three to five years after diagnosis and primary therapy[17]. The exact molecular biological pathophysiology of TNBC has so far been very poorly understood[18]. There are large differences in the five-year survival rates, which depend crucially on the degree of differentiation and the receptor status. For example, it is 99% for G1 tumors that are smaller than 2 cm and have a negative lymph node finding, for HR-positive breast carcinomas and for ERBB2-positive ones at 94% and for TNBC at 85%. Due to the triple negativity of the tumors TNBC lacks molecular targets for a specific treatment, thus chemotherapy is most commonly applied[19]. For non-metastatic cases, breast-conserving surgery (BCS), as well as mastectomies are performed. This is mostly done in combination with adjuvant chemotherapy or radiation treatment traditionally

given in TNBC to improve locoregional control in breast cancer patients following mastectomy or conservative breast surgery[20,21]. Even though there are much more refined treatment regimens for TNBC to this date, the prognostic outcome for the patients is still relatively poor. Therefore, there is a clear need for the evaluation of novel therapeutic strategies against TNBC including radiation therapy.

1.3 Imaging strategies for of breast cancer diagnosis

The breast is mainly composed of adipose and fibrous tissue. Detection of a tumor within this complex architecture remains challenging and is predominantly done by mammography - a planar x-ray imaging technique. Mammography has two main weaknesses: I) the entire internal structure of the breast is projected onto one plane and thus breast cancer can be obscured by other structures and II) comparably low x-ray absorption of the breast tissue leads to poor contrast. Moreover, mammography requires compression of the breast which leads to discomfort of the patient. Additionally, the high rate of false positive findings in mammography are of concern as they cause trauma for the patient and lead to costly follow up biopsies. Thus, mammography has been critically discussed for a long time[22]. Breast CT[23,24] and dedicated breast MRI[25,26] have been proposed as alternatives but have not reached a widespread use yet. Breast CT as a true 3D technique does not suffer from the projection problem of mammography but can only hardly be achieved at low x-ray doses. In addition, without the use of contrast agents the sensitivity and specificity of breast CT is only marginally above classical mammography[27]. However, in combination with contrast agents a clear depiction of the tumor can be reached in most cases as demonstrated in Figure 2. Since breast cancer presents a severe burden to public health, screening programs have been established in many countries in the last decades. Since breast CT and MRI are expensive and are not widely available, screening is solely done by mammography with all its outlined weaknesses. In addition to screening and diagnosis, imaging also needs to be performed for radiation treatment planning, staging of the tumor and evaluation of therapy response. Thus, a novel imaging strategy that shows an improvement of tumor delineation is of great interest and would benefit many patients.

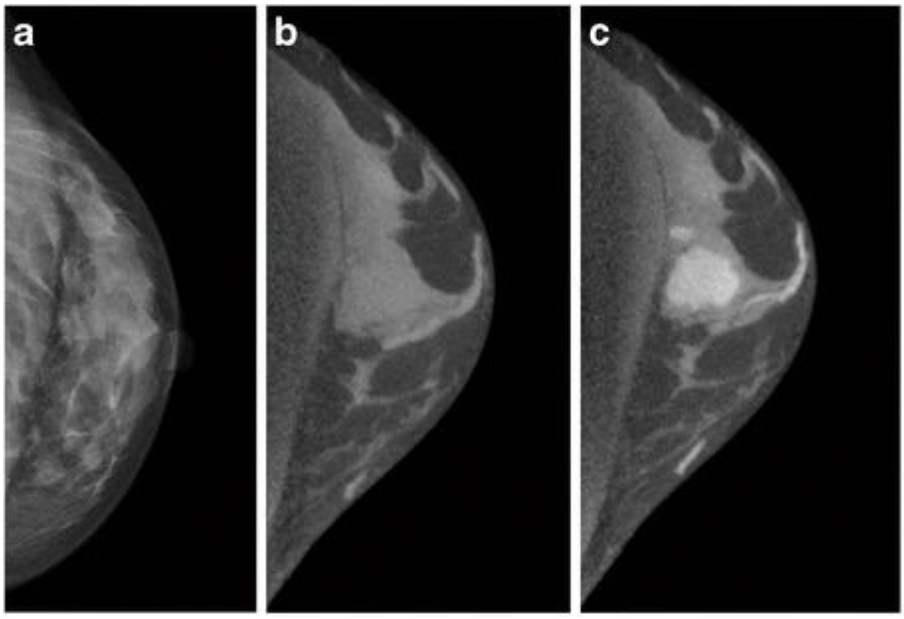

Figure 2: ***Comparison of mammography and breast CT on the example of an invasive ductal carcinoma.***

A) Mammography shows no presence of the tumor. B) Breast CT slice without the application of contrast agent. No tumor can be identified. C) Contrast enhanced breast CT clearly shows the tumor lesion. Modified from Wienbeck et al.[28]

1.4 Radiation therapy of breast cancer

Apart from surgical removal of the tumor, radiation therapy (RT) is commonly applied, especially in cases where the metastases cannot be easily removed or are too widespread for surgery[21]. RT is clinically used in several situations. After breast-conserving surgery (BCS) to reduce the chance of a tumor recurrence, after a mastectomy, if the cancer is found in many lymph nodes or in the surrounding tissue[29,30].

RT uses the fact that the fast dividing tumor cells have an impaired repair mechanism for radiation damage compared to healthy cells[31]. Thus, in RT the tumor regions are irradiated with high energy beams. Mostly x-ray beams with photon energies in MeV range are used, but also proton-beams can be utilized[32]. The main advantage of RT is therefore that it can be generally applied in all tumor entities in contrast to immunotherapy, which can only be used if the tumor expresses a certain antigen[33]. However, apart from the tumor cells, healthy cells also experience radiation damage, especially cell types with a high proliferation rate, such as the hematopoietic stem cells in the bone marrow. To spare the healthy tissue as good as possible RT is typically delivered from different angles that lead to overlapping irradiation fields within the tumor[34,35]. In addition, the high beam energies are used to reduce the absorption of the radiation in

superficial tissue like the skin. This concept has three consequences for the patient: I) in most cases a contrast enhanced CT image is needed for the irradiation planning , II) the high beam energies can only be delivered with special devices (linear accelerators, LINACs) and III) in the tumor region the absorption of the radiation is low due to the high energies.

Since the initial CT image is the basis of the irradiation plan, the delineation of the tumor margins and the position of the tumor in this scan is of utmost importance. However, the CT is performed in a different device than the RT, meaning that the patient needs to be repositioned between CT scan and RT, which makes it challenging to reproduce the exact location of the tumor, especially in the cases of soft-tissue tumors. In addition, RT and CT are usually carried out in different departments and the irradiation planning also requires some time. Thus, typically there are days between CT and first irradiation[36].

The mode of action of RT is a combination of direct radiation damage to the DNA causing apoptosis of the cells and the production of reactive oxygen species (ROS) due to ionization[37]. These ROS are then damaging the surrounding cells. In both cases the effect is proportional to the dose, the energy that is absorbed, delivered to the tumor. Thus, increasing the absorption of the cells should boost the efficacy of RT. Therefore, the potential use of contrast agents has been studied, using the same formulations that are used for contrast enhancement in CT[38]. However, at the typical beam energies in the MeV range, the increase in absorption by such contrast agents is only marginal. The use of elements with even higher atomic numbers is difficult to achieve due to various reasons such as: limited accessibility of those substances as well as toxicity issues. As an alternative a reduction of the beam energy has been proposed[39–41]. Low energy RT however also bears a higher risk of damaging healthy tissue in the light path. Thus, the ideal contrast agent should increase the efficacy of RT so much that the use of lower beam intensities is compensated by the favorable effect of the therapy. Such an approach - if realizable - would result in RT in an energy regime similar to that of CT and would therefore allow performing tumor diagnosis and treatment at the same time in the same system.

1.5 Physical basics of dose and dose measurement

As pointed out above the effect of RT is determined by the amount of absorbed energy / the applied dose. Therefore, understanding the definition of dose and how to measure dose is crucial. In physics, dose describes the work that is performed within matter by the absorbed radiation. This so-called absorbed dose ***D*** is measured in Gray [Gy] and is defined as 1 J of energy that has been absorbed by 1 kg of matter [Gy=J/kg]. Since the biological effect also

depends on the type of radiation the so-called equivalent dose ***H*** has been defined which includes a weighting factor for the type of radiation and is measured in Sievert [Sv]. The weighting factor for x-rays is 1 whereas for instance the factor for alpha-radiation is 20[42]. In addition, different organs have different susceptibilities for radiation damage. This is denoted in the so-called effective dose ***E*** which is also measured in Sievert [Sv] and includes weighting factors for specific organs, which add up to a weighting factor of 1 for whole-body exposure. The weighting factors take the stochastic dose effects - mostly the elevated cancer risk into account. Thus, they cannot directly be transferred to preclinical studies. In such studies virtually only the absorbed dose is discussed (if the dose is reported at all)[43].

Since the dose depends on several aspects such as the tissue composition, a reliable measurement is challenging. In addition, the tissue causes scattering of the x-rays that increases the absorbed dose. Thus, dose measurements should always be done in an appropriate phantom that mimics the properties of the animal/patient. However, dose measurements can only be used as an estimate, since a patient with a greater body mass will always receive a higher dose in comparison with a patient with a low body mass, even if exactly the same device settings are used. To measure the dose, an effect that converts absorbed photon energy into a measurable current need to be used, as in ionization chambers or Geiger-Müller counters. To measure the effective dose inside the experimental animal or even a patient is virtually impossible. One option to achieve this, at least in a dead animal, is the use of thermoluminescence dosimeters (TLDs). TLDs are small crystals that convert the absorbed dose into a permanent change of electron distribution and are commonly used in finger ring dosimeters. Due to their small size TLDs can be integrated in phantoms or for instance implanted in dead animals and will therefore provide a reliable readout of the absorbed radiation and the specific location within the body. When heated the crystal emits light proportional to the absorbed energy[44].

1.6 X-ray imaging and radiation therapy devices

CT is a 3D imaging modality based on radiography. The patient/object is radiographed, which projects the attenuation of the x-rays along their light paths onto a 2D detector. To recover the 3D information the inverse problem of these projections has to be solved[45]. In order to overcome the loss of the dimensionality from a 3D object to a 2D projection image, a reconstruction algorithm is applied which needs a set of (typically evenly) angularly distributed projection images as an input. Thus, CT is more dose dependent than planar radiography since a large number of images (most commonly in the range of thousands) needs to be taken, while either

the object is rotated, or the detector is circling around the object. Since the contrast in CT is based on the difference in the attenuation of x-rays between different tissues, which become marginal at higher photon energies, CT is usually performed with average energies in the range of 40-60 keV. These energies are large enough that an object as big as the human body can still be penetrated, but low enough to provide sufficient contrast. The x-rays are produced by an x-ray tube as shown in Figure 3 A. Figure 3 B shows the typical setup for a clinical CT system. Both the x-ray tube as well as the x-ray detector rotate around the patient on a so-called gantry. Figure 3 C shows an exemplary microCT system which is used for non-living samples. Due to the need for a high precision, the x-ray tube and the detector are fixed in place. To achieve projections from different angles, the sample is rotated.

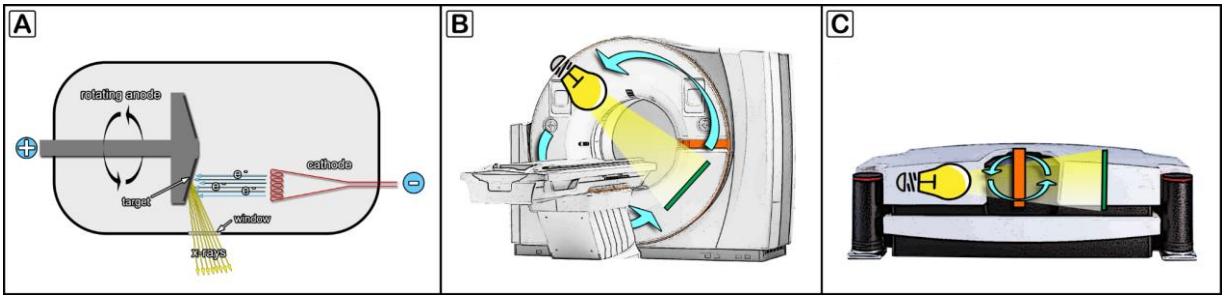

Figure 3: ***Overview of x-ray imaging techniques.***

A) Functional principle of an x-ray tube. Electrons are emitted by the cathode and hit the rotating tungsten target on the anode. X-rays are emitted. B) Schematic representation of a clinical CT scanner using a gantry configuration, where x-ray tube and detector rotate around the patient. C) Schematic representation of a microCT using a fixed geometry with a rotation sample.

To deliver radiation dose to the tumor site during RT, photons with high energies between 1 and 25 MeV are generated and used for irradiation of the patient. This principle is called external beam RT and is the most commonly applied method. At these high energies the absorption within the tissue is rather low, thus only a minimal dose is delivered to the skin. To ensure a sufficient dose deposition at the tumor site, RT is applied from different angles, however fewer than in CT. Such high intensity, high energy beams cannot be produced in an x-ray tube, the common x-ray source in CT. Therefore, linear accelerators (LINACs) must be employed. The functional principle of a LINAC is demonstrated in Figure 4 A. In comparison to classical x-ray tubes, producing higher energy x-rays requires additional electron acceleration. This is done by using alternating currents between so-called “drift tubes”. Figure 4 B shows a clinical LINAC as used for RT.

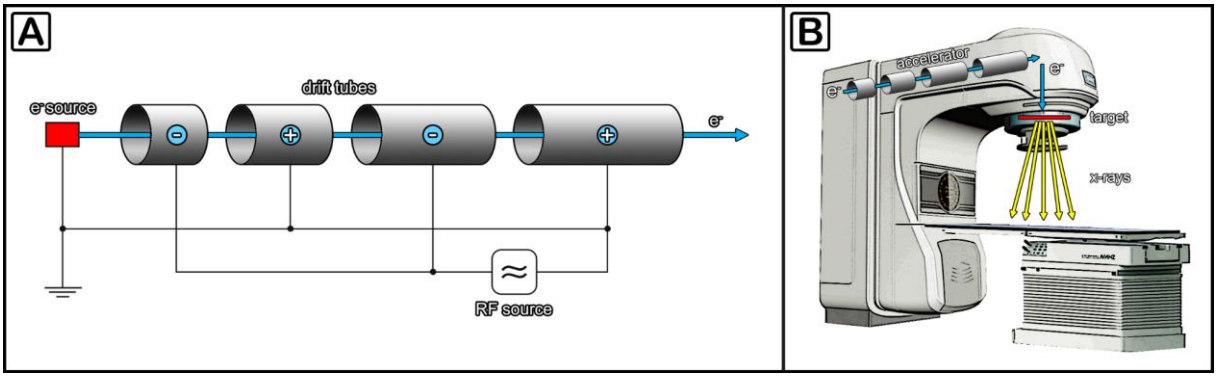

Figure 4: ***Basics of medical LINACs****.*

A) Functional principle of electron acceleration in a LINAC. Alternating currents between so-called drift tubes accelerate electrons. B) Medical LINAC for radiation therapy. Due to the accelerated electrons high energy x-rays are generated.

Due to the different requirements CTs and LINACs differ vastly in the properties of the radiation they produce and are therefore not interchangeable.

1.7 Nanoparticles in cancer diagnosis and therapy

Nanoparticles, by definition are particles with a diameter between 1 and 100 nm and distinguished from microparticles for which the diameter ranges from 1 to 1000 µm[46]. Here we will use the term nanoparticles (NPs) for particles with a diameter below 1 µm.

NPs have a broad spectrum usage in (bio-)medical applications[47]. Liposome and polymer based NPs are used as a vehicle for drug or gene delivery[48,49]. In addition, many different NPs are used for various imaging techniques[50]. Quantum dots for instance are inorganic semiconductor molecules used for optical imaging[51,52], while metallic or metal-containing NPs are used for CT and MRI[53–56].

Due to their size in the range or even below the wavelength of visible light they cannot be seen using standard light microscopes. Nowadays, a large variety of NPs can be generated, ranging from compact NPs like gold particles[57], crystal like structures[58] and particles composed by a core material encapsulated in a shell[59]. Due to their small size they can enter cells and can therefore be used as carriers for different compounds[60]. An example in CT imaging is the use of NPs with surface modifications to increase the blood half time, compared to classical contrast agents. The so-called “blood pool” agents were developed for clinical applications at a time

when CT acquisitions took much longer[61]. Nowadays, they are not used in clinical CT anymore. However, they experienced a renaissance in preclinical imaging as demonstrated in Figure 5, where a clear contrast enhancement of the tumor vasculature can be observed when using the blood pool contrast agent eXia160 in comparison with the clinical contrast agent Isovist300.

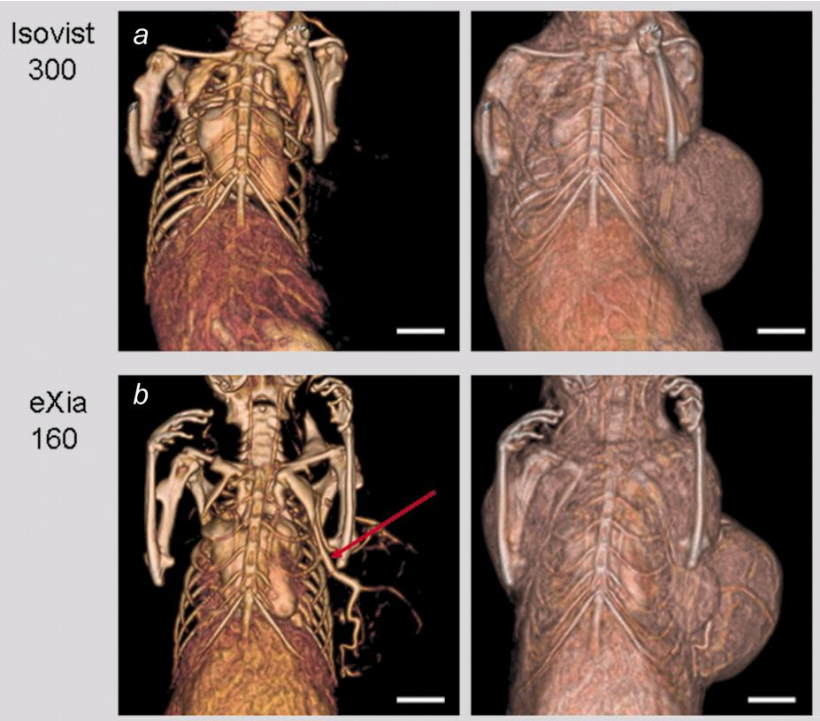

Figure 5: ***Contrast enhanced microCT for vascular imaging using iodine-based contrast agents.***

A) 3D rendering of a CT scan of a mouse injected with the clinical contrast agent Isovist 300. Visualization of the tumor vasculature is not possible because of the short blood half lifetime of the contrast agent. B) 3D rendering of a CT scan of a mouse injected with Exia160, a contrast agent optimized for preclinical imaging, showing a clear delineation of the tumor vasculature. Adapted from Jannasch et al.[62]

In the context of this work the NPs should boost the contrast for imaging as well as raise the efficacy of RT. Such a combined approach of diagnostics and therapy is typically called Theranostics. Several questions arise for the development of an effective RT enhancer: I) what the core material should be, II) how big should the particle be and II) how it can be functionalized to specifically target the tumor cells. Similar approaches are discussed by Choi et al.[63]. Typically, gold or gadolinium are used as core material[64]. To my knowledge, barium was not used as an element for RT enhancement yet. High Z-elements show a strong x-ray attenuation, which does not guarantee an increase in radiation dose delivered to tumor cells. However, the interaction of the particles with the incident x-ray beam triggers several effects,

mainly the production of primary photoelectrons, the generation of Auger-electrons as well as inelastic scattering of the x-ray photons[65]. These mechanisms typically result in an increased RT effect in close proximity of the particles[66]. Since I propose to use CT as the irradiation source, the comparably low photon energy of about 40-45 keV makes photo-electron emission the most dominant effect. If the emission of the photoelectron leads to an inner shell vacancy, highly cytotoxic Auger electrons can be emitted[67,68]. However, it can be expected that such effects are restricted to the immediate vicinity of the NPs. Thus, many studies reported dramatic increases in the efficacy of in-vitro RT in combination with NPs of sizes in the range up to 15 nm[69–72]. Particles, in this size range, are taken up by cells and will therefore be located close to the nucleus allowing the photo and Auger electrons to directly damage the DNA. However, it is very likely that such particles would also be taken up by healthy cells if applied systemically, thus they do not present a suitable approach for patient application.

Typically, CT imaging in small animals is done with a tube voltage of about 80-90 kV which (slightly depending on the type of x-ray source) results in an x-ray spectrum centered around 40-45 keV[73]. Depending on their atomic structure all elements show specific non-linearities in their x-ray absorption. The most dominant of these is the so-called k-edge, the energy for which a k-shell electron gets emitted. At this energy there is a maximum in the absorption. For iodine and barium, the k-edges are at 33.2 keV and 37.4 keV respectively[74]. The x-ray attenuation spectrum of barium and an estimated x-ray spectrum are visualized in Figure 6. Thus, especially barium is ideally suited for my purposes and was selected as core material for the RT enhancers used in my thesis.

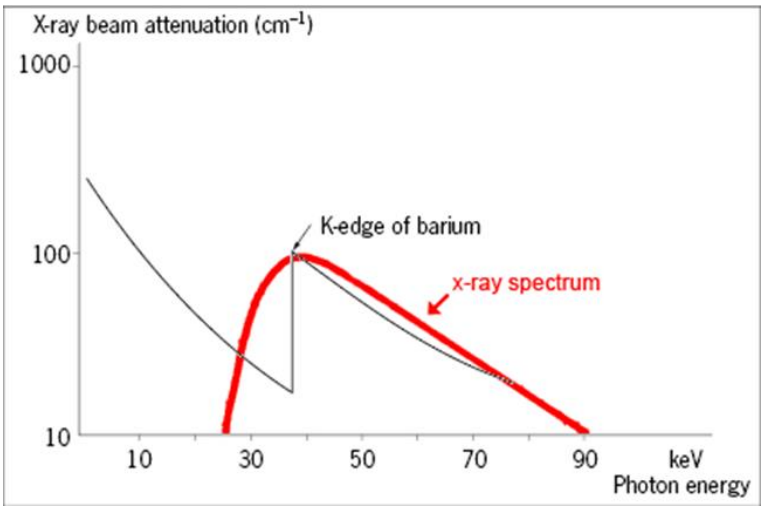

*Figure 6**: Energy dependence of x-ray attenuation of barium**.*

The black line depicts the x-ray attenuation of barium. A clear attenuation maximum is visible at the K-edge of barium at 37.4 KeV. The red line shows a typical x-ray spectrum of a standard x-ray tube. The maximum of the spectrum almost perfectly overlaps with the barium K-edge.

Regarding the size of an effective RT enhancer, it should present an optimization between being small enough for good biodistribution and large enough to provide effective absorption of x-rays. In my case, the size ranged between 120 and 300 nm as demonstrated by transmission electron microscopy images shown in Figure 7.

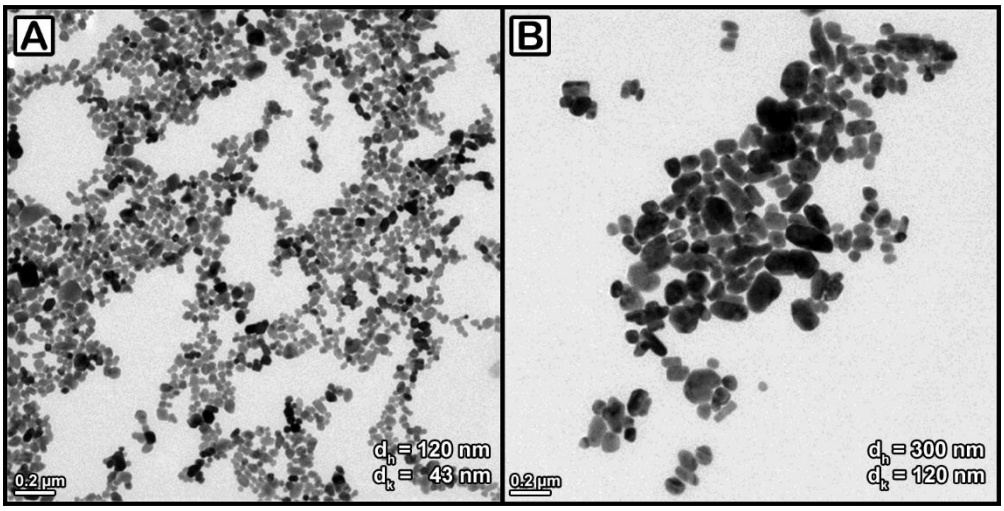

Figure 7: ***Transmission electron microscopy of BaNPs.***

A) Ba120 NPs with a hydrodynamic diameter of 120 nm and a core diameter of 43 nm. B) Ba300 NPs with a hydrodynamic diameter of 300 nm and a core diameter of 120 nm.

The barium core in the proposed NPs is protected by a polymer layer to avoid any toxic side effects. This polymer layer can also be used for functionalization with a tumor specific antibody (Ab). However, such an approach would eliminate the advantage of RT as a tumor entity independent therapy. Even if functionalized Abs are used, it is questionable if a sufficient concentration of NPs for RT enhancement is achievable. It is often claimed that even without functionalization, particle enrichment within the tumor can be obtained by the so-called enhanced permeability and retention (EPR) effect. But the extent to which the EPR effect improves the tumor NP enrichment is very controversial[60,75]. Thus, superficial tumor models were chosen for this thesis, which allow for a direct intra tumoral administration of NPs.

1.8 The WAP-T transgenic mouse model

In preclinical oncology, it is often difficult to find the right and clinically relevant tumor model to examine the complex biomedical processes of breast cancer as well as the systemic interaction with the tumor-bearing organism and its immune system. There is now an abundance of mouse models for breast carcinogenesis and tumor progression available. Because of the great anatomical and genotypic similarities between rodents and humans as well as the comparable development of the breasts, the murine breast is particularly suitable as a model for examining breast cancer and for the preclinical evaluation of new therapies[76–78].

For the presented animal experiments, the orthotopically implanted pH8N8 syngeneic mouse model was chosen. It is based on the syngeneic WAP-T breast cancer mouse model, which was established as a useful surrogate of human TNBC by Schulze-Garg et al[79,80]. pH8N8 breast cancer cells were isolated from an endogenously induced tumor of the bi-transgenic WAP-T-NP8xWAP-mutp53-H8 mouse line, then established[80]. After orthotopic transplantation of these cells in WAP-T-NP8 mice, breast carcinomas of an epithelial phenotype with mesenchymal components are formed. They have a morphology similar to the parental tumors and mostly depict a poorly differentiated phenotype[81,82]. After orthotopic transplantation, the pH8N8 tumor cells continue to grow independently of hormones because of accumulation of further genetic alterations in the pH8N8 genome due to T-Ag-mediated inactivation of Tp53 and Rb1[83]. The immunocompetent orthotopically implanted pH8N8 syngeneic mouse model is a valuable system for investigating the effectiveness of therapy because it is uncomplicated to: I) generate tumors, II) administer therapeutic agents, III) follow the development of growth kinetics by measuring the tumors using a caliper. In addition, immunocompetent mice are used, which allows to evaluate the role of the immune system in cancer progression and therapy.

1.9 X-ray based virtual histology as a tool for the 3D analysis of tumor samples

While classic section based histology has been used for pathological analysis of soft tissue specimens for decades, lately 3D techniques based on high resolution CT imaging (microCT) have emerged[84–87]. Classical histology has many advantages, the specimen preparation protocol is relatively straightforward and compatible with countless different staining regimens. To date, this makes histology the gold standard for the analysis of tissue samples. Especially, in combination with immunohistochemistry and the use of color or enzyme labeled antibodies,

histology allows staining of certain cell types and tissue structures specifically. The resolution of histology is thereby only limited by the used microscope.

However, there are disadvantages to classical histology: I) the specimen needs to be chemically dehydrated and embedded, both of which can significantly alter the morphology of the tissue, II) the sample needs to be cut, which can introduce additional deformations and destroy the specimen within the process and, III) since histological processing of tissue is time consuming, usually only a small fraction of the tissue is analyzed, which holds the risk of missing important features of the sample. In addition, the cutting process is done in a nearly blind manner and in a fixed direction depending on the position of the tissue in the embedding material. Reliable and reproducible sectioning can therefore be rarely obtained. Moreover, since histology is based on imaging of micrometer thin tissue slices, the obtained parameters are intrinsically two-dimensional (2D) and in terms of geometric measures are of questionable quality due to the mentioned deformation processes.

MicroCT has been previously tested for the 3D assessment of tissue specimens. microCT is intrinsically 3D, can provide resolution even below 1 µm and since it uses high energetic radiation can penetrate larger specimens. The disadvantage of microCT is that its contrast is based on the relative electron density and therefore it generates only poor image quality in soft-tissue specimens composed solely of low atomic number elements with only minor differences in their electron density. In contrast, for the 3D analysis of bones microCT can already be considered the method of choice. To circumvent the problem of low contrast in soft-tissue different heavy metal ion-based staining protocols have been reported similar to the ones used for electron microscopy[88–91]. Another option to drastically increase the contrast is the use of different microCT imaging techniques, which do not rely solely on x-ray attenuation as the method for contrast generation. Our group, among others, has already demonstrated that the use of synchrotron light sources to perform so-called “phase contrast imaging” or “propagation-based imaging” (PBI) enables the use of unstained soft tissue specimens for high resolution microCT analysis[92,93]. Our group has already demonstrated that by optimizing these protocols microCT imaging can be combined with subsequent histological analysis and even immunohistochemistry[92,94]. We called this approach x-ray based virtual histology (xVH) and the basic workflow is shown in Figure 8.

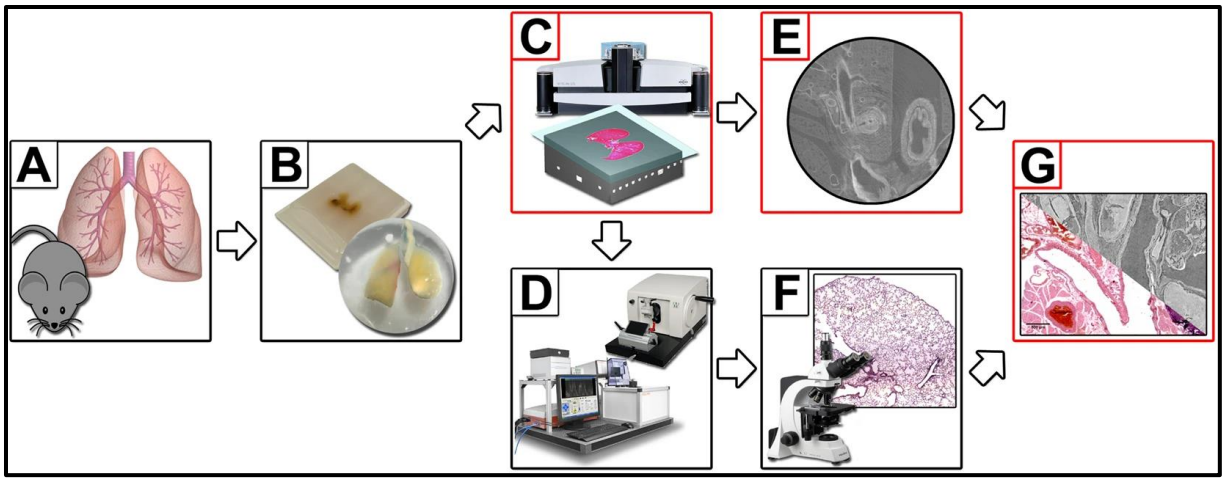

Figure 8: ***Workflow of microCT guided sectioning.***

A) Sample generation by organ explantation. B) Specimens are PTA dehydrated and embedded. (C) A microCT scan is performed and the position of interest defined within the 3D reconstructed phase retrieved data sets. D) The samples are cut at the predefined. E) A virtual slice is produced from the microCT data set. F) A microscopical image is generated from stained histological images. G) fusion of both imaging modalities. Figure was taken from Albers et al.[94]

The biggest downside of microCT imaging in comparison to histology is the lack of specificity for certain structures or tissue types. Thus, other imaging techniques have been developed such as k-edge subtraction imaging (KES). KES exploits the non-linearity in the x-ray absorption of elements with respect to the x-ray energy[95,96]. If an energy is reached which equals the binding energy of a specific electron, the electron is emitted and a strong increase in the absorption can be seen. The strongest absorption band can be found at the binding energy of the k-shell electron and is called k-edge. The k-edge is element specific and can therefore be exploited for imaging. In KES two acquisitions are performed with x-rays filtered specifically to two specific energies above and below the k-edge of the element of interest. In my case for barium the k-edge is at 37.4 keV which is ideally suited for medical CT imaging which is typically done in that energy range. Since for the two energies the absorption of all other elements will basically not change, a subtraction of those images will be highly specific for barium only. KES imaging can also be combined for two or more elements to perform multiplexing as shown by Bayat et al. on the example of xenon and iodine[97]. However, the approach of filtering the x-ray spectra to two sharp energies results in a dramatic loss of flux which virtually limits the approach to synchrotron light sources.

Analyzing the fate of the NPs inside the tumors after RT is an important step to understanding their functional mechanism. xVH is an especially useful tool for that because it is intrinsically 3D and the BaNPs can be easily discerned from their surrounding tissue. PBI allows the use of

unstained tumor samples, which is important due to the fact that an additional staining may mask the contrast of the BaNPs and therefore would complicate the analysis of the local environment and distribution of the BaNPs inside the tumor specimen.

1.10 Bioluminescence imaging for the evaluation of tumor progression

Bioluminescence itself describes the ability of living organisms to produce light[98]. In nature bioluminescence can be found in fireflies, the sea pansy and various bacteria[99]. Bioluminescence imaging (BLI) is a commonly applied method in preclinical imaging in which specific cells (like in my case the pH8N8 breast tumor cells) are transfected with DNA fragments which encode for an enzyme like luciferase, which catalyzes the light reaction. In addition, whole transgenic bioluminescent animals can be created[100]. As soon as a substrate molecule, like in my case luciferin, is injected, light with wavelengths in the visible spectrum is produced by luciferase containing cells. The big advantage of BLI is that only living transfected cells can produce a signal, which is therefore specific to the analyzed disease model. This specificity in combination with the fact that BLI allows non-invasive monitoring of tumor development makes it a great tool for longitudinal cancer therapy studies[101]. However, the signal is typically weak and is strongly absorbed when originating from locations in the body. To ensure measurements of weak signals a light proof cabinet and a cooled CCD camera to reduce the electronic noise are used.

1.11 Aims of the study

Radiation therapy is commonly employed for various tumor entities as a single treatment or in combination with surgery or chemotherapy. Due to its non-specificity, irradiation also effects healthy tissue and is therefore connected with unavoidable side effects. TNBC is an aggressive type of breast cancer, which lacks tumor specific therapy targets and is therefore only treated with systemic treatments like chemotherapy or surgery. Radiotherapy is given in TNBC as indicated in other breast cancer subtypes to improve locoregional control following mastectomy or breast conserving surgery. Thus, there is a clear need to explore new treatment options for TNBC. The aim of the here presented PhD project is to evaluate the feasibility of using the combination of an in vivo microCT imaging system with barium nanoparticles (BaNPs) to perform radiation therapy using a mouse model for TNBC. The use of BaNPs as radiotherapy enhancer would locally increase the administered x-ray dose in the tumors and therefore allow for a reduction of the total applied dose, limiting the side effects of radiation therapy.

For this purpose, the thesis presented here addresses the following questions:

- **Can low energy radio therapy in an in vivo microCT be effectively used for irradiation treatment of breast cancer?**

  This will be addressed by:

  - Establishing an irradiation setup for CT radiotherapy of breast tumors, including shielding of non-tumor regions to treat tumors that developed in mice after orthotopic breast cancer cell implantation
  - Performing dose measurements in order to implement irradiation protocols in tumor mouse models with doses comparable to those used in the clinic.
  - Designing an irradiation-based tumor treatment regimen based on low energy microCT aiming at efficient reduction of tumor growth, with minimum side effects.

- **Does the application of BaNPs enhance the effect of radio therapy on tumor growth?**

  This will be addressed by:

  - Evaluation of BaNP cytotoxicity by in vitro cell viability assays, to ensure the compatibility of the BaNPs with in vivo studies
  - Assessment of CT contrast enhancement of BaNPs
  - In vitro evaluation of a BaNP dependent enhancement of the irradiation effect on clonogeneic cell survival using colony forming assays.
  - In vivo assessment of an improved radio therapy outcome in the presence of BaNPs by monitoring tumor progression in relation to irradiation
  - Ex vivo analysis of the fate of BaNPs in explanted tumors using histology and x-ray based virtual histology

2 Material

2.1 Cell lines

Table 1: ***Cell Lines used in this work***

Cell line	Origin	Manufacturer
3T3	murine fibroblast	Leibniz Institute DSMZ-German Collection of Micro-organisms and Cell Cultures GmbH, Braunschweig
A549	human adenocarcinoma lung cancer	American Type Culture Collection, Manassas, USA
MH-S	murine immortalized macrophages	American Type Culture Collection, Manassas, USA
pH8N8	murine triple negative like breast cancer	Prof. Dr.W. Deppert (Universitätsklinikum, Hamburg-Eppendorf)
pH8N8-BLI	murine breast cancer cells transduced with lentiviral vector for luciferase and eGFP (Firefly luciferase-GFP lentivirus (CMV, Puro))	cells: Prof. Dr. W. Deppert (Universitätsklinikum, Hamburg-Eppendorf) lentiviral vector: Cellomics Technology, Halethorpe, USA

2.2 Mouse strains

Table 2: ***Mouse strains used in this work***

Mouse line	Manufacturer
NMRI-nu Immunodeficient Mouse	Janvier Labs, Le Genest-Saint-Isle, France
WAP-T NP8	breeding colony, MPI EM, Göttingen

2.3 Devices

Table 3: ***Devices used in this work***

Device	Manufacturer
Axiovert 200 inverted microscope	Carl Zeiss Microscopy GmbH, Jena
Bone density CT phantom	QRM Quality Assurance in Radiology and Medicine GmbH, Möhrendorf
Cell culture incubator (BB6220)	Heraeus Holding GmbH, Hanau
Cryo microtome (CM1950)	Leica Biosystems Nussloch GmbH, Nussloch
Dehydration automat	Süsse Labortechnik, Gudensberg
Dose measurement device + probe (Diados)	PTW, Freiburg
Epson PERFECTION V800 PRO flatbed scanner	Seiko Epson K.K , Suwa, Japan
Flattening Table for Histology	Medax GmbH & Co.KG, Neumünster
Glass syringe (10 µl)	Hamilton, Reno, USA
HM 340 E microtome	Thermo Fisher Scientific Corp., Waltham, USA
IP67 TESA digital caliper	Hexagon Metrology GmbH, Wetzlar
Isoflurane anesthesia system (for IVIS Spectrum, Matrix™ VIP 3000 Calibrated Vaporizer)	Midmark, Dayton, USA
Isoflurane anesthesia system (for QuantumFX)	VisualSonics, Toronto, Canada
IVIS Spectrum	Perkin Elmer, Waltham, US
Laminar Flow Hood (cell culture work bench, HBB2448)	Heraeus Holding GmbH, Hanau
LSM880 confocal laser scanning microscope	Carl Zeiss Microscopy GmbH, Jena
Multiplate spectrometer (Eon)	BioTek Instruments, Inc., Winooski, USA
Neubauer cell counting chamber	Schuett-Biotec GmbH, Göttingen
Paraffin embedding station (EG1160)	Leica Biosystems Nussloch GmbH, Nussloch
Quantum FX microCT system	Perkin Elmer, Waltham, US
Steam cooker for IHC (Braun)	De'Longhi Deutschland GmbH, Frankfurt
Stereo microscope (Stemi SV 6)	Carl Zeiss Microscopy GmbH, Jena
Tissue Float Bath	GFL Gesellschaft für Labortechnik mbH, Burgwedel

2.4 Chemicals

Table 4: ***Chemicals used in this work***

Chemicals	Manufacturer
2-Mercaptoethanol	Merck KGaA, Darmstadt
Acetone	Merck KGaA, Darmstadt
Acetic acid	Merck KGaA, Darmstadt
AEC substrate kit	Becton Dickinson GmbH, Heidelberg
Agarose (BioReagent)	Merck KGaA, Darmstadt
Aniline blue	Sigma-Aldrich, Darmstadt
Antibody Diluent (Dako)	Agilent Tech., Santa Clara, USA
Aquatex mounting medium	Merck KGaA, Darmstadt
Bieberich's scarlet red acid fuchsin solution red	Sigma-Aldrich, Darmstadt
Bouin's solution	Sigma-Aldrich, Darmstadt
Carprofen	Zoetis Schweiz GmbH, Delémont, Switzerland
DAPI	Thermo Fisher Scientific Corp., Waltham, USA
Dulbecco's Modified Eagle Medium (DMEM)	Thermo Fisher Scientific Corp., Waltham, USA
Entellan mounting medium	Merck KGaA, Darmstadt
Eosin	Merck KGaA, Darmstadt
Ethanol	Merck KGaA, Darmstadt
Ethylendiamintetraacetat (EDTA)	Merck KGaA, Darmstadt
Fetal calf serum (FCS)	Thermo Fisher Scientific Corp., Waltham, USA
Formaldehyde (4%)	Merck KGaA, Darmstadt
Glycine (0.3 M)	Merck KGaA, Darmstadt
Hoechst 33342	Thermo Fisher Scientific Corp., Waltham, USA
Hydrogen peroxide (3%)	Merck KGaA, Darmstadt
Isoflurane	Abbvie, Ludwigshafen, Gemany
Isopropanol	Merck KGaA, Darmstadt
Ketamine	Medistar Arzneimittelvertrieb GmbH, Ascheberg
Luciferine (Vivo Glo Luciferin)	Promega, Madison, USA

Mayers hematoxylin solution	Merck KGaA, Darmstadt
Paraffin	Süsse Labortechnik, Gudensberg
Paraformaldehyde (4%)	Merck KGaA, Darmstadt
PermaFlour mounting medium	Thermo Fisher Scientific Corp., Waltham, USA
Phosphate buffered saline (PBS)	Thermo Fisher Scientific Corp., Waltham, USA
RPMI-1640 cell culture medium	Thermo Fisher Scientific Corp., Waltham, USA
Saline solution (0.9 %)	B. Braun Melsungen AG, Melsungen
Sea Block Blocking Buffer	Thermo Fisher Scientific Corp., Waltham, USA
Sorbitol	Merck KGaA, Darmstadt
Target Retrieval Solution pH 6 (Dako)	Agilent Tech., Santa Clara, USA
TRIS buffer	Merck KGaA, Darmstadt
Triton-X 100	Merck KGaA, Darmstadt
Trypan blue	Thermo Fisher Scientific Corp., Waltham, USA
Trypsin-EDTA (0,05 %/0,02 %)	Merck KGaA, Darmstadt
Weigert's iron hematoxylin	Merck KGaA, Darmstadt
WST-1 cell titer solution	Sigma-Aldrich, Darmstadt
Xylazine	Riemser Pharma GmbH, Greifswald
Xylol	Merck KGaA, Darmstadt

2.5 Consumables

Table 5: ***Consumables used in this work***

Consumables	Manufacturer
6-well plate	Greiner Bio-One GmbH, Frickenhausen
24-well plate	Greiner Bio-One GmbH, Frickenhausen
96-well plate	Greiner Bio-One GmbH, Frickenhausen
Bepanthen Eye ointment	Roche, Basel, Switzerland
Cell culture flasks	Sarstedt AG & Co. KG, Nümbrecht
Combitips advanced (Biopur)	Eppendorf AG, Hamburg

Cover slips	Thermo Fisher Scientific Corp., Waltham, USA
Eppendorf Safe-Lock Tubes	Eppendorf AG, Hamburg
Falcon tubes	Corning, New York, USA
Glass slides (Menzel Superfrost plus)	Thermo Fisher Scientific Corp., Waltham, USA
Insuline syringes (Micro-Fine U100 0,3 ml)	Becton Dickinson GmbH, Heidelberg
Leukosilk tape	BSN medical GmbH, Hamburg
Paraffin embedding cassettes (Rotilabo)	Carl Roth GmbH + Co. KG, Karlsruhe
Pipette tips	Sarstedt AG & Co. KG, Nümbrecht
Serological pipettes	Greiner Bio-One GmbH, Frickenhausen
TLDs (GR-200 A)	Hangzhou Freq-control Electronics Technology Co., Ltd, Hangzhou, China
Vicryl surgical thread (Ethicon 4-0 Vicryl)	Johnson & Johnson Medical GmbH, Norderstedt

2.6 Antibodies

Table 6: ***Antibodies used in this work***

Antibody	Species	Manufacturer
anti-mouse CD326 (Ep-CAM) antibody (Biolegend 118222)	Rat	BioLegend, San Diego, USA
anti-mouse CD68 antibody (abcam 125212)	Rabbit	Abcam, Cambridge, Great Britain
anti-mouse SV40 T-Antigen antibody	Rabbit	Prof. Dr. W. Deppert (Universitätsklinikum, Hamburg-Eppendorf)
Histofine Simple Stain	Goat	Nichirei Biosciences Inc., Tokyo, Japan

2.7 Nanoparticles

Table 7: ***Nanoparticles used in this work***

Nanoparticles	Concentration	Manufacturer
BaNP-120	300 mg/ml	nanoPET Pharma, Berlin
BaNP-160	300 mg/ml	nanoPET Pharma, Berlin
BaNP-220	500 mg/ml	nanoPET Pharma, Berlin
BaNP-300	355 mg/ml	nanoPET Pharma, Berlin
Ba120-EpCam-A594	320 mg/ml	nanoPET Pharma, Berlin
IodineNPs	220 mg/ml	nanoPET Pharma, Berlin

2.8 Software

Table 8: ***Software used in this work***

Software	Manufacturer
Fiji / ImageJ	NIH, Bethesda, USA
GraphPad Prism 8	GraphPad Software, San Diego, USA
Imaris (v9.1.2)	Oxford Instruments, Abingdon, England
Living Image (v4.4)	Caliper Life Science Inc., Hopkinton, USA
MATLAB R2018b	MathWorks, Natick, USA
Office 365	Microsoft, Redmond, USA
Photoshop CS6	Adobe Inc., San Jose, USA
QT Creator (v15)	The Qt Company, Espoo, Finland
Scry (v6.0)	Kuchel & Sautter Gbr, Bad Teinach-Zavelstein
Syrmep Tomo Project (STP, v1.2.4)	ElettraSciComp/ Francesco Brun, Trieste, Italy
VG Studio MAX (v3.2)	Visual Graphics GmbH, Heidelberg

2.9 Synchrotron Facilities

Table 9: ***Synchrotron facilities used in this work***

Synchrotron facilities	Beamline	Location
ELETTRA Synchrotrone Trieste	SYRMEP	Trieste, Italy
European Synchrotron Research Foundation (ESRF)	ID 17	Grenoble, France

3 Methods

3.1 Maintenance of cell lines

All cell lines (Table 1) were cultivated under standardized conditions at 37 °C, 5% CO_2 and a relative humidity of 95% in an incubator. All cell culture work was carried out under a sterile workbench and with sterile materials. pH8N8, A549 and 3T3 cells were kept as a monolayer culture in uncoated cell culture flasks in high glucose Dulbecco's modified Eagle medium (DMEM) with the addition of 10% fetal calf serum (FCS). For MH-S cells, RPMI-1640 medium containing 0.05 mmol 2-mercaptoethanol and 10% FCS was used. Depending on the rate of growth, the cells were passaged at a confluence of 70-80% two to three times per week in a ratio of 1:10. For this purpose, they were washed with a phosphate buffered saline solution (PBS) and removed from the flask by adding a 0.05% trypsin / 0.02% EDTA solution for a short incubation time of approx. 3 min in the incubator. After centrifuging for 2 min at 1200 rpm and room temperature, the pellet was taken up in fresh cell culture medium and the number of cells was determined with a Neubauer cell counting chamber and seeded again in the appropriate concentrations.

3.2 Generation and validation of bioluminescent pH8N8 cells

The bioluminescent pH8N8 breast cancer cells were generated by Dr. Joanna Napp and Jakub Mitrega (Translational Molecular Imaging, MPI EM, Göttingen).

pH8N8 cells were transduced with a lentiviral vector encoding for firefly luciferase and eGFP under the CMV promotor. A puromycin resistance gene was used for cell selection. The cells were sorted for eGFP positive cells using fluorescence-activated cell sorting (FACS) and clonal selection was performed by seeding one cell per well on a 96-well plate. The cells were grown into small colonies and transferred into six well plates. Cells with good growth rates were transferred into cell culture flasks and their BLI signal was measured in vitro using the IVIS Spectrum device. These cells are referred to as pH8N8-BLI in the thesis.

3.3 Nanoparticle synthesis and characterization

All NPs for this work were specifically designed and manufactured by nanoPET pharma and due to company's intellectual property protection policies, no detailed information about the formulations can be provided. Briefly, barium sulphate ($BaSO_4$)-based nanoparticles (BaNPs) were produced by chemical precipitation at ambient conditions. After a purification step, the particles were sterically stabilized using a biocompatible polymer. The obtained highly stable colloidal suspension was sterilized and formulated for in vitro / in vivo use. Particles with different hydrodynamic diameters between 120-300 nm were produced. Before being used for this work, the NPs were tested in vitro by nanoPET pharma and were found to be non-toxic and to have no effect on the vitality of mammalian cells (data not shown).

BaNP-120 were also conjugated with Alexa Fluor® 594 anti-mouse CD326 (Ep-CAM) antibody for certain in vivo applications. These BaNPs are referred to as Ba120-EpCam-A594.

3.4 WST cell proliferation assay

Proliferation assays were used to analyze the number of viable cells by the cleavage of tetrazolium salts added to the culture medium. Tetrazolium salts like WST-1 ((4-[3-(4-Iodophenyl)-2-(4-nitro-phenyl)-2H-5-tetrazolio]-1,3-benzene sulfonate) are cleaved to formazan by cellular enzymes (Figure 9). An expansion in the number of viable cells results in an increase in the overall activity of mitochondrial dehydrogenases in the sample, which in turn increases the amount of formazan dye formed. Quantification of the formazan dye produced by metabolically active cells was done using a scanning multi-well spectrophotometer.

To perform the cell proliferation assay, $1x10^5$ cells per well of different cell lines were pipetted into 96-well plates with 200 µl of cell culture medium. The plates were incubated for 24 h at 37 °C. The different NP-solutions were diluted 1:10 in cell culture medium containing 20 mg/ml sorbitol. 200 µl of NP containing medium was added to the well. After 0, 4, 8, 24 or 48 h the medium was removed, the cells were washed twice with 200 µl PBS and 200 µl fresh medium with 20 µl WST-1 cell titer solution was added. The cell proliferation was measured after 2 h using a BioTek Eon photometric device at a wavelength of 490 nm.

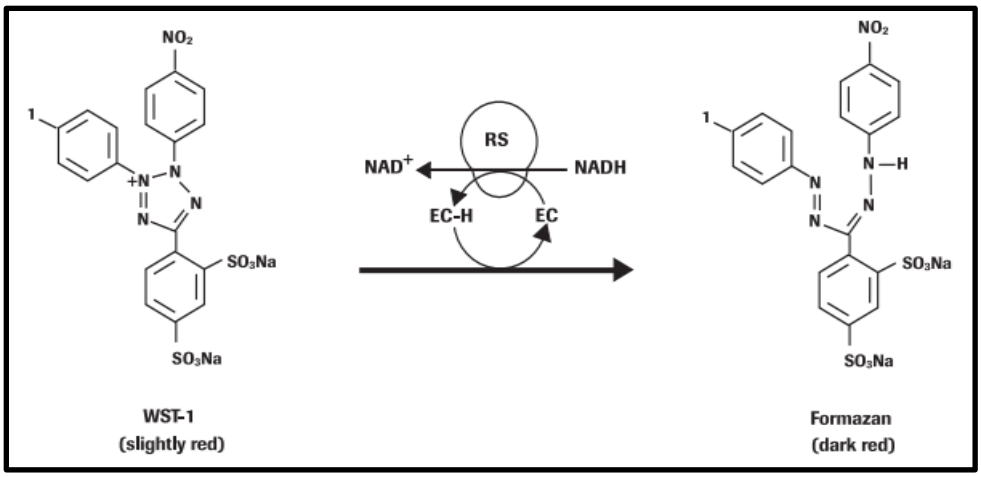

Figure 9: ***Chemical reaction for colorimetric detection in a WST assay.***

The substrate WST-1 is cleaved by cellular enzymes to the dark red product formazan. Image was taken from Sigma-Aldrich[102].

3.5 Quantification of CT contrast enhancement of NPs

To measure the x-ray contrast enhancement of different NPs, a dilution series was done, and CT datasets were acquired using the QuantumFX in vivo microCT. A 2 min scan was performed using a tube voltage of 90 kV, a tube current of 200 µA and a field of view (FOV) of 20 mm. The NPs were scanned either undiluted or diluted in PBS in a ratio of 1:1, 1:5 and 1:10 in 1.5 ml micro reaction tubes. The NP concentrations of the undiluted stock solutions can be found below in Table 10:

Table 10: ***Concentrations of NP stock solutions for quantification of CT contrast enhancement***

NP	Concentration [mg/ml]
BaNP-120	300
BaNP-160	300
BaNP-220	500
Iodine NPs	220

To correct for possible contrast differences caused by the CT system, a bone density phantom with known concentrations of calcium hydroxyapatite was included in each acquisition. A calibration curve of the calcium concentrations in the phantom (200, 400, 600, 800, 1000 mg/cm^3) was used to normalize the measured gray values of the NPs. For better comparison of the NPs, the normalized contrast was divided by the concentration of the NPs.

3.6 Quantification of X-ray irradiation effect on tumor cell survival

3.6.1 Principle

The colony forming assay (CFA) is an in vitro cell survival assay based on the ability of a single cell to grow into a colony[103]. After irradiation of the cells, they are counted, separated and a specific number of cells is seeded into cell culture plates. The mean number of colonies which grow following addition of fresh culture medium represents the absolute colony forming ability of cells. This number reflects the survival rate of the cells after passage and seeding in the culture plates. A cluster of at least 50 adjacent cells was defined as a colony. To avoid the labor-intensive manual counting of the cells under a (stereo-) microscope, I developed a semi-automated workflow using a standard flatbed scanner and a self-made software based on MATLAB to quantify the CFA colonies (Figure 10).

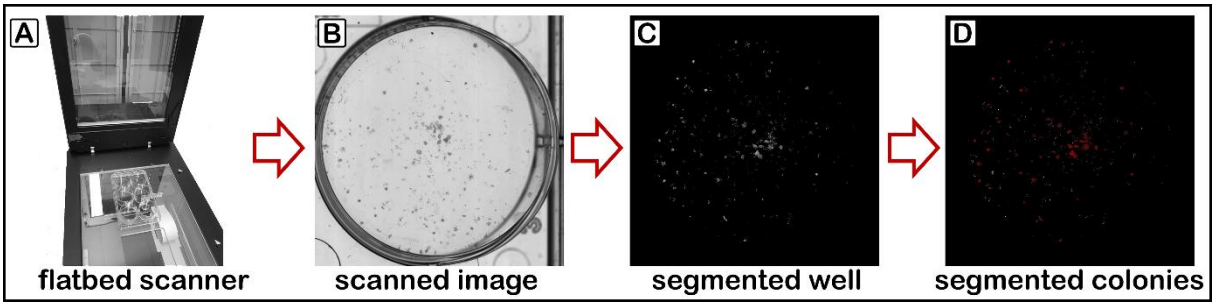

Figure 10: ***Workflow auf automatized CFA analysis.***

A) A standard flatbed scanner in transillumination mode is used to acquire images of well plates. B) Exemplary image of a well containing cell colonies. C) Segmented cells inside the same well. D) Cells that were identified as colonies are pseudo-colored in red.

3.6.2 Irradiation of tumor cells and NPs

Murine pH8N8 breast tumor cells or human A549 lung cancer cells were cultured in a T-75 cell culture flask. When confluency was reached, the cells were washed with 10 ml PBS. The adhesive cells were removed from the flask by adding 5 ml trypsin/EDTA and incubating for 5 min. Trypsination was stopped by adding 10 ml cell culture medium containing FCS. The cells were centrifuged for 2 min at 1200 rpm. The cell pellet was resuspended in 4 ml PBS and distributed into four 1.5 ml E-cups. Before irradiation the cells were gently centrifuged again, and the PBS was removed with a pipette. When required, 50 µl undiluted BaNP-120 solution (concentration 300 mg/ml) was added and gently mixed using a pipette. Subsequently the cells were irradiated in the QuantumFX in vivo microCT using the following parameters:

Table 11: ***In vitro CT irradiation parameters***

Parameter	Value
Tube voltage	90 kV
Tube current	200 µA
FOV	20 mm
Irradiation time	2 min
X-ray dose	~ 1 Gy

After irradiation, the cells were resuspended in cell culture medium and counted using a Neubauer chamber. 1000 cells per well for pH8N8 cells or 500 cells per well for A549 cells were plated into 6-well plates. One plate was used per treatment group per experiment.

3.6.3 Colony forming assay (CFA)

The plated colonies were incubated for 7-10 days at 37 °C and 5% CO_2 until the colonies were large enough for imaging but did not start to merge. The cell culture medium was removed, and each well was washed with 2 ml PBS. The cells were fixed by adding 1 ml/well of 70 % EtOH for 15 min. The plates were left open to dry in the workbench. To stain the cells, 1 ml/well of hematoxylin staining solution was added and incubated for 5 min. The staining solution was

removed with a pipette and kept for re-use. The wells were rinsed gently with demineralized water followed by a bluing step for 5 min under a light tab water flow. The cell culture plates were left open in the workbench until they were completely dry.

3.6.4 Imaging of CFA colonies using a flatbed scanner

To replace the labor-intensive manual counting of the cell colonies, all plates were imaged using a standard flatbed scanner (Epson Perfection V800). 16-bit gray value images were acquired using the transillumination mode of the scanner (Figure 10 A). The images were taken at a resolution of 1200 dpi, resulting in images of an approximate size of 4000 x 6000 px for each 6-well plate. Colonies on the images were automatically counted using a self-made software written in MATLAB.

3.7 Confocal microscopy of pH8N8 tumor cells with fluorescence labeled Abs

$5x10^4$ pH8N8 breast cancer cells were plated on coverslips and grown overnight (ON). The cells were then fixed for 15 min with 4% PFA, blocked for 30 min with 5% FCS-PBS and incubated with 1 µg/ml of either Alexa Fluor® 594 anti-mouse CD326 (Ep-CAM) antibody or with Ba120-EpCam-A594 BaNPs, ON at 4°C. Cell nuclei were stained with Hoechst 33342 for 10 min at room temperature, before the coverslips were mounted on glass slides.

A Zeiss LSM880 confocal laser scanning microscope equipped with Airyscan and hybrid detectors, a 40× oil objective lens (1.4 Plan-APOCHROMAT), a motorized stage and a tunable laser (470–670 nm) was used for acquisition. Image analysis was performed with Imaris 9.1.2 and Fiji software.

3.8 Housing and maintenance of mouse lines

The housing conditions consisted of a twelve-hour light-dark rhythm at 22 °C and 55% relative humidity. Animal food and water were given *ad libitum*. The mice were handled in accordance with the animal welfare experimental animal regulations.

Female nude NMRI-nu immunodeficient mice were ordered from Janvier Labs and used entered into the experiment after two weeks of acclimatization.

Maintenance of the WAP-T-NP8 mouse colony was ensured by mating heterozygous WAP-T-NP8 males with wild-type BALB/c females. Thus, the risk of accumulation of mutations by homozygous mating and inadvertent induction of the transgene in females is avoided. All animal in vivo procedures were performed in compliance with the guidelines of the European Directive (2010/63/EU) and the German ethical laws and were approved by the administration of Lower Saxony, Germany under the reference numbers 33.9-42502-04-17/2630 and 33.9-42502-04-18/3022.

3.9 Preparation of tumor cells for transplantation

A549 lung cancer cells as well as pH8N8 and pH8N8-BLI breast cancer cells were prepared according to the following protocol for in vivo application. Cells were passaged 24 h prior to transplantation, to reach about 80% of confluency. Cells were washed with 10 ml PBS once and removed from the cell culture flask by adding 3 ml trypsin/EDTA and incubating for 5 min at 37 °C. Cells were rinsed from the bottom of the flask by adding 7 ml of medium. 20 µl cell suspension was mixed with 20 µl trypan blue and counted using a Neubauer cell counting chamber. The cell suspension was centrifuged for 5 min at 1200 rpm. $1x10^6$ cells were resuspended in 1 ml cell culture medium and transferred to an e-cup. The e-cups were centrifuged again and carefully transported to the site of transplantation. Immediately before the injection of the cells the cell culture medium is removed with a pipette and the cell pellet resuspended in PBS.

3.10 Orthotopic transplantation of breast cancer cells

The orthotopic transplantation of $1x10^6$ pH8N8 or pH8N8-BLI tumor cells into the right abdominal mammary gland of syngeneic WAP-T-NP8 mice was performed after intraperitoneal (i.p.) administration of 2.5–3 µl/g body weight (BW) ketamine/xylazine

combination anesthesia. It consists of 75 mg/kg BW ketamine and 15 mg/kg BW xylazine in a 0.9% saline solution and was prepared 24 h before the orthotopic transplantation. After the anesthesia set in, 5 mg/kg BW of the analgesic carprofen was applied i.p. in a volume of 1.2 µl/g BW. The eyes were protected from drying by applying Bepanthen eye ointment. The anesthetized mouse was placed on a 37 °C heating plate to protect against hypothermia in supine position and fixed with Leukosilk tape. Next to the right nipple of the abdominal mammary gland a 3-4 mm incision was made. $1x10^6$ tumor cells were suspended in 20 µl PBS using a 0.3 ml U100 insulin syringe. After carefully separating the breast from the connective tissue, the prepared cell suspension was injected directly into the breast tissue. The syringe remained in the injection site for 5 s to prevent reflux of cell suspension. The skin of the wound was closed with 2-3 stitches with absorbable Vicryl surgical thread. The duration of the transplantation procedure was 5–10 min in total. Transplanted animals were checked and weighed three times a week for the entire duration of the experiments. Irradiation treatment was started when a tumor volume of 300 mm^2 was reached. Tumor volumes were measured using a caliper and determining the width, length and height of the tumors. Tumor volume was calculated using the simplified ellipsoid volume equation:

$$V \approx \frac{width \times length \times height}{2}$$

3.11 Subcutaneous implantation of lung cancer cells

Nude NMRI-nu immunodeficient mice were used for the implantation of the human A549 lung cancer cells. $4x10^6$ A549 cells were resuspended in 100 µl PBS and subcutaneously (s.c.) injected in the left flank of the mouse using a U100 insulin syringe. Tumor volumes were measured using a caliper and determining the width, length and height of the tumors. Tumor volume was calculated using the simplified ellipsoid volume equation:

$$V \approx \frac{width \times length \times height}{2}$$

3.12 In vivo administration of BaNPs

For irradiation experiments the undiluted NP solutions were directly injected into the tumor. This was performed as soon as the tumors reached a size of 300 mm^3 and 24 h before the first

irradiation. To achieve a homogeneous NP distribution in the tumor, 3x 10 µl of BaNP solution were injected with a 10 µl Hamilton glass syringe at three different sites of the tumor.

To evaluate the biodistribution of functionalized NPs, 100 µl anti-EpCAM-Ab labeled Ba120 NPs were administered i.v. into two WAP-T NP8 pH8N8 tumor bearing mice (tumor size approx. 300 mm^3).

3.13 Evaluation of biodistribution of i.v. administered anti-EpCAM-Ab labeled BaNPs

Two WAP-T NP8 pH8N8 tumor bearing mice were scanned in-vivo under isoflurane anesthesia (2-3 % isoflurane in 1:1 O_2/air with a flow of 1 L/min) in the QuantumFX in-vivo microCT directly after BaNP injection, as well as 1, 7 and 24 h later. The QuantumFX was operated at 90 kV tube voltage, 200 µA tube current using a FOV of 40x40 mm^2 and the cardiac gating acquisition protocol with a total scanning time of 4.5 min.

3.14 Measurement of x-ray doses generated by the in vivo microCT

The absorbed dose was measured for different settings of the QuantumFX in vivo microCT using a commercial dose rate measuring system (Diados, PTW), which is commonly used for consistency checks in clinical CT scanners. This system measures the dose length product (Unit: $Gy \cdot cm$) and is typically used in combination with an appropriate phantom. As no appropriate phantom is available for mouse irradiation and the clinical phantoms do not fit into the small animal CT, the measurements were performed without a phantom.

In order to test the performance of the purposely built mouse holder and shielding device and to obtain a more accurate reading of the dose at the tumor site, thermoluminescence detectors (TLDs) were implanted into dead mice in different locations. The TLDs were provided and analyzed by the Radiation Protection group of the Italian Synchrotron ELETTRA.

3.15 BLI measurements of breast cancer bearing mice

Bioluminescence imaging (BLI) was performed using the IVIS Spectrum system. The IVIS Spectrum is essentially a dark chamber equipped with a sensitive camera that is electronically cooled down to -90 °C to reduce noise. Each night, the system measures the dark current in the detector and the background radiation and calibrates for it. The IVIS is one of the few optical imaging systems that provides a completely referenced unit in terms of photons per second, area and solid angle with respect to the camera objective lens and additionally takes the quantum efficacy of the camera into account. The total flux of the BLI signal was measured as photons/s.

pH8N8-BLI tumor bearing mice were injected i.p. with 3 µl luciferin (concentration: 50 mg/ml) per 1 g BW prior to the administration of isoflurane anesthesia. The anesthetized mice were scanned 4, 7, 10 and 13 min after luciferin injection to ensure that the peak of the bioluminescence was captured. Since the luciferin needs to reach the site of the bioluminescent cells and is used up during the production of light, a correlation between signal intensity and amount of living tumor cells can only be made at the peak of the signal.

To take the irregular shape of the tumor into account, the analysis was performed using a threshold of 10%. This means that all signals/pixel with an intensity greater than 10% of the maximum signal were analyzed. For these signals, the total flux (integral) and the tumor area (amount of pixel times pixel size) were calculated.

3.16 Tumor sample processing and embedding

The mice were sacrificed using a CO_2 overdose in combination with a cervical dislocation. The tumors were explanted, the skin and fur removed and fixed in 4% PFA (paraformaldehyde) ON.

3.17 Histological staining procedures

3.17.1 Embedding in paraffin blocks

To produce paraffin blocks, formalin-fixed tissue samples were washed for 10 min with deionized water (D-water) in order to remove formalin residues. The samples were dehydrated by sequential incubation steps for 1.5 h each in 60%, 70%, 80%, 90%, 95%, 100% ethanol and xylol. This procedure was followed by infiltration with liquid paraffin for 1.5 h. Dehydration and infiltration took place in the automatic tissue infiltration machine with the program shown in Table 12. Finally, the tissue samples were embedded in paraffin blocks using a paraffin pouring station. Paraffin blocks were stored in the dark at room temperature.

Table 12: ***Dehydration and paraffinization protocol***

Step	Time (h)
60% EtOH	1.5
70 % EtOH	1.5
80 % EtOH	1.5
90 % EtOH	1.5
100 % EtOH	1.5
100 % EtOH	1.5
xylol	1.5
paraffin	1.5

3.17.2 Microtome sectioning of histological slices

The paraffin blocks were cooled on a -20 °C cooling plate for 30 min. The tissue sections were produced with a microtome at a section thickness of 2 µm. The sections were immediately smoothed in a water bath at approx. 45 °C, transferred to microscope slides and dried overnight at room temperature or for 20 min at a maximum of 65 °C on a hot plate. Sections treated according to this scheme were either stained histochemically, by IHC or stored in slide boxes at room temperature.

3.17.3 Deparaffinization and rehydration of tissue sections

For histochemical and IHC staining, tissue sections were first manually deparaffinized and rehydrated. For this, the paraffin was melted in a drying cabinet at 60 °C for 30 min, followed by sequential incubation steps in xylol and a descending alcohol series (Table 13).

Table 13: ***Deparaffinization and rehydration protocol***

	Time (min)	Reagent
Deparaffinization	7	xylol
	7	xylol
Dehydration	5	isopropanol
	5	98% EtOH
	5	75% EtOH
	5	60% EtOH
	5	H_2O (demineralized)

3.17.4 Hematoxylin-eosin staining (HE)

HE staining is a standard staining in histology, where hematoxylin stains cell nuclei in blue/violet, while eosin stains the cytoplasm, collagen, keratin, and erythrocytes in red. The sections were first deparaffinized and rehydrated. After rehydration, the sections were stained for 5 min in Mayer's hematoxylin solution. Subsequently, the sections were rinsed shortly in demineralized water followed by a bluing step for 5 min with tap water. The samples were stained for another 5 min in eosin staining solution. To prepare the eosin staining solution, 5 g eosin were solved in 500 ml demineralized water and 1-2 drops of acetic acid were added. To stop the staining process, the samples were rinsed in demineralized water. Subsequently the samples were dehydrated and mounted using Entellan mounting medium. The dehydration protocol is shown in Table 14.

Table 14: ***Dehydration protocol***

	Time (min)	Reagent
Dehydration	short	H_2O (demineralized)
	short	60% EtOH
	short	75% EtOH
	5	98% EtOH
	5	isopropanol
	5	xylol
	5	xylol

3.17.5 Masson's trichrome staining

For the assessment and analysis of the collagen content in the tumor, Masson's Trichrome staining (MTS) was performed. Cell nuclei were stained black with Weigert's iron hematoxylin, cytoplasm and muscle tissue with Bieberich's scarlet red acid fuchsin solution red and collagen with aniline blue. Slides were incubated at 60 °C for 30 min, followed by a deparaffinization and rehydration protocol as described in Table 13. Tissue sections were fixed in Bouin's solution at room temperature ON, then rinsed with tap water to remove excess reagent. Sections were stained with Weigert's hematoxylin solution, rinsed sequentially in tap and deionized water, and then stained with the trichrome kit whereby the slides were placed in phosphotungstic/phosphomolybdic acid solution and aniline blue solution for 5 min each. Slides were treated with 1% acetic acid, dehydrated through alcohol, cleared in xylene and mounted using Aquatex mounting medium.

3.17.6 Immunohistochemical staining

IHC staining is used to detect target proteins in formalin-fixed organs. The detection is based on the affinity of a primary antibody (pAb) for a specific epitope of a protein. Here we used unconjugated pAbs, which were made visible by secondary antibodies (sAb). The sAb is linked to a detection system, that is based on an enzymatically catalyzed conversion of the colorless aminoethylcarbazole (AEC) substrate into a colored end product by oxidation of the peroxidase coupled to the sAbs. In order to make target proteins more accessible for their Ab, tissue sections were boiled for 20 min in a steam cooker in 1x citrate buffer pH 6 (Target Retrieval Solution). After cooling for 5 min in double-distilled water on ice, the sections were washed

twice for 5 min in Tris-HCl buffer pH 7.6. The samples were then treated with 3% hydrogen peroxide for 10 min at room temperature in order to reduce the effect of endogenous oxidases and then washed again twice with Tris-HCl pH 7.6. The individual tissue sections were incubated for 20 min at room temperature with salmon serum (Sea Block Blocking Buffer) in order to minimize nonspecific binding and thus background staining. The pAb was diluted in Antibody Diluent and applied to the tissue sections. The incubation took place ON at 4 °C in a humid chamber, followed by two washing steps with Tris-HCl pH 7.6. To detect the pAb, the sections were then incubated with the sAb in Tris-HCl pH 7.6 at RT for 1 h and washed again twice with Tris-HCl pH 7.6. Tissue sections were incubated for 30 min at RT with the AEC substrate kit and the color reaction was stopped with distilled water. For counterstaining, the tissue sections were immersed in Mayers' hemalum solution for 20 s, washed briefly in distilled water and then blued in tap water for 5 min. Finally, the stained sections were sealed airtight with the mounting medium Aquatex and a cover slip. The pAbs and sAbs used as well as the dilutions and individual conjugations used are listed in Table 15 below.

Table 15: ***Antibodies for IHC***

Antibody	pAb/sAb	Species	Reactivity	Dilution
CD68	pAb	rabbit	mouse	1:500
T-Ag (R15)	pAb	rabbit	mouse	1:5000
Histofine Simple Stain	sAb	goat	rabbit	undiluted

Histological and IHC images were acquired using an Axiovert 200 inverted microscope. To depict the whole paraffin section, the built-in stitching algorithm of the microscope was used with a 10× magnification.

3.17.7 Antibody staining for confocal microscopy of pH8N8 tumor slices

For confocal microscopy, cryosections of pH8N8 breast tumors were cut with a microtome (Leica CM1950). The thawed sections were fixed with acetone for 10 min at room temperature. After the acetone was evaporated under the workbench, an incubation of 20 min at room temperature with 0.2% Triton-X was performed. The slices were washed two times for 5 min with Tris-HCl pH 7.6. Afterwards the slices were incubated for 30 min in 0.3 M glycine at room temperature and washed again twice with Tris-HCl pH 7.6 for 5 min each. The individual tissue sections were incubated for 20 min at room temperature with salmon serum (Sea Block

Blocking Buffer) to minimize nonspecific binding and thus background staining. The EpCAM-Alexa594 pAb was diluted in a ratio of 1:200 in Antibody Diluent and applied to the tissue sections. The incubation took place ON at 4 °C in a humid chamber, followed by two washing steps with Tris-HCl pH 7.6. Cell nuclei were stained with DAPI (dilution 1:4000) for 5 min and washed again with Tris-HCl pH 7.6 for 5 min. sections were sealed airtight with the mounting medium PermaFlour and a cover slip.

A Zeiss LSM880 confocal laser scanning microscope equipped with Airyscan and hybrid detectors, a 20× oil objective lens (1.4 Plan-APOCHROMAT), a motorized stage and a tuneable laser (470–670 nm) was used for acquisition. Image analysis was performed with Imaris 9.1.2 and Fiji software.

3.18 Synchrotron radiation microCT (SRµCT) of mouse breast tumor samples embedded in paraffin

To specifically detect the barium content in the tumor, I used k-edge subtraction imaging (KES) at the European Synchrotron Research Foundation (ESRF) in Grenoble. KES uses the fact that the x-ray absorption for a given material is non-linear with so-called edges at energies specific for the binding energy of a certain electron. To obtain barium specific contrast subtraction images the Pixie-III detector was set to energy thresholds of 36.5 and 38.5 keV. 2000 angular projections with a pixel size of 52 µm and an exposure time of 100 ms per projection were acquired resulting in a scanning time of 200 s. For the generation of barium maps the low energy reconstructions were subtracted from the high energy reconstructions.

All high-resolution SRµCT acquisitions for xVH were performed using the white/pink beam setup of the SYRMEP (SYnchrotron Radiation for MEdical Physics) beamline of the Italian synchrotron ELETTRA which is depicted in Figure 11.

Whole paraffin embedded samples were scanned with a sample to detector distance (SDD) of 500 mm. 3600 angular distributed projections with an exposure time of 50 ms were acquired over 360° resulting in a scan time of 180 s. A 0.5 mm Si filter was used, resulting in a mean beam energy of 19.6 keV. All high resolution SRµCT data sets were reconstructed using SYRMEP Tomo Project software (STP Version 1.3.2)[104]. A single distance phase retrieval algorithm developed by Paganin et al.[105] was used with a delta over beta ratio of 100. To image

the entire tumors, 3-4 single acquisitions were performed, and the resulting reconstructions were manually stitched together using Fiji (NIH).

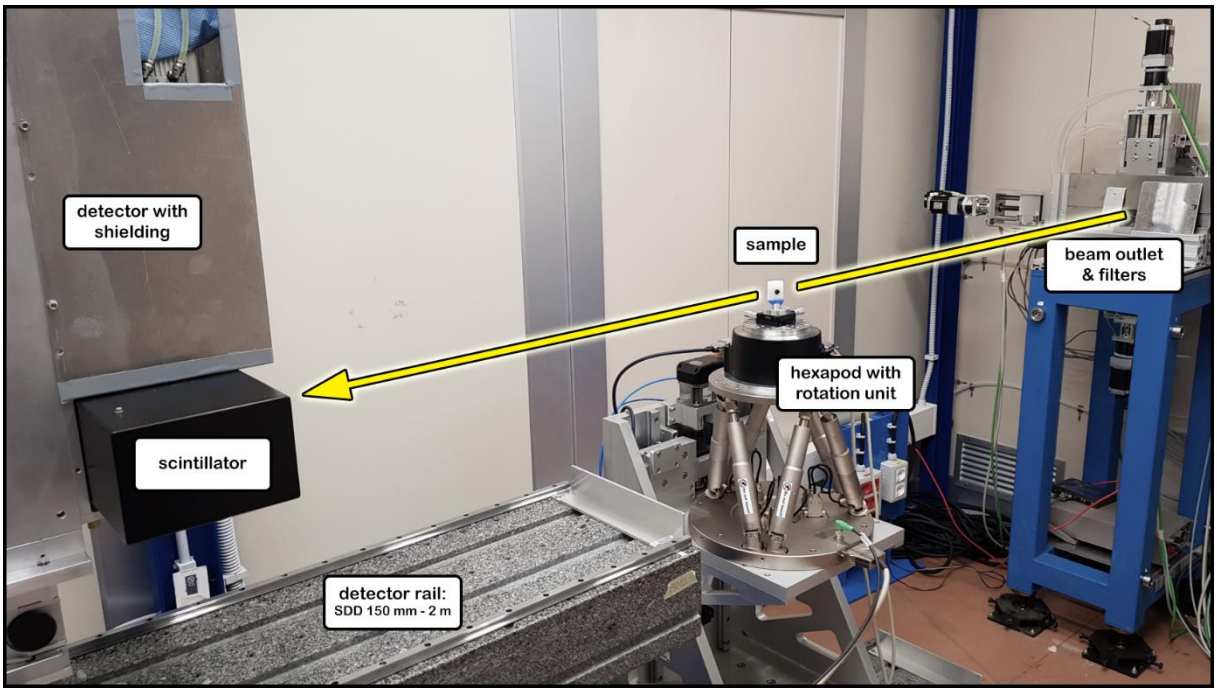

Figure 11: ***White beam setup of the SYRMEP beamline.***

The light path which originates from the bending magnet and passes through the beam outlet and the filters is indicated by the yellow arrow. The sample is positioned and rotated using a combined hexapod/rotation unit. The x-ray detector is mounted on a movable rail and contains a scintillator crystal for the conversion of the x-rays into the visible light spectrum, as well as microscope optics and a water-cooled CCD camera.

3.19 Elastic registration of microCT and histological images for xVH

To perform image registration between SRµCT data sets and histological slices the CT data was reoriented to match the cutting angle of the histology. This resampling and identification of the appropriate matching virtual slice was done using VG Studio MAX. Fiji was used to pre-process the histological images. Calculation of the deformation and transformation of the images was done via Elastix and Transformix[106,107] that were integrated into a tailored graphic user interface called Fuxlastix. The Fuxlastix frontend was developed in C++, using QT5.15 and is available on https://github.com/xPITcoding/Fuxlastix. For the presented data, the registration process took less than a minute using a standard computer with a quad-core CPU.

3.20 Statistical analysis

In order to check for statistically significant differences between the analyzed groups I applied variance analysis utilizing two types of ANOVA tests. For all in vitro analysis for which a sample size of larger than 6 could be achieved, I applied a “Brown-Forsythe” test that assumes Gaussian distribution of the measured values but does not imply equal variances in all groups[108]. Since “Brown-Forsythe” uses the median for comparison and not the mean it has been found to be more robust even if the assumption of Gaussian distribution is violated[109]. For all in vivo measurements, due to the comparably small sample sizes and the larger variations, a Gaussian distribution could not be assumed. Thus, I applied a “Kruskal Wallis” test that operates on ranks and not on medians but otherwise is equivalent to the “Brown-Forsythe” test[110]. For both tests I used the implementations in GraphPad Prism 8. From here on *, **, ***, **** indicate p-values of <0.05, <0.01, <0.001 and <0.0001, respectively.

4 Results

The concept of using BaNPs to enhance breast tumor contrast in CT and in parallel to enable radiation therapy in the same device has not previously been attempted. The BaNPs used in this study were designed especially for this purpose and therefore needed to be characterized before a possible in vivo application. Thus, all components to develop this novel treatment approach had to be established and optimized.

4.1 Evaluation of toxic effects of BaNPs on cell growth

In order to rule out any toxic effects of the newly designed BaNPs, I performed cell metabolic activity (WST) assays. Three different murine cell lines (pH8N8 breast cancer, 3T3 fibroblasts and MHS immortalized macrophages) were used. These cell lines were chosen, because pH8N8 was chosen to be used for further in vivo experiments. MHS macrophages were used, because these cells were expected to take up and incorporate the NPs[56]. 3T3 fibroblasts are commonly used as a non-tumor reference cell line. All three cell lines were exposed to three different particle types: BaNP-120, BaNP-160 and BaNP-220 which only differ in their hydrodynamic diameter as indicated by the number, which refers to the average diameter in nanometers.

To assess the viability of the cells the optical density (OD) was measured at 0, 4, 8, 24 and 48 h using a photometric device at a wavelength of 490 nm. To compensate the absorption of the NPs inside the corresponding cell culture medium itself, a blank sample, which did not contain any cells was measured additionally and subtracted from the measured values. Figure 12 shows the corrected OD over time. A Brown-Forsythe ANOVA test was performed at all measured datapoints at 24 h to evaluate if the NPs had a significant influence on cell viability. No significant reductions in the metabolic activity in comparison with the control group was found except for the BaNP-220s and pH8N8 cells (Figure 12 A) and the BaNP-120 and the 3T3 cells (Figure 12 B).

Since almost no negative effects of the NPs on the metabolic activity of the cells was found, I concluded that all three formulations are suited for in-vivo applications.

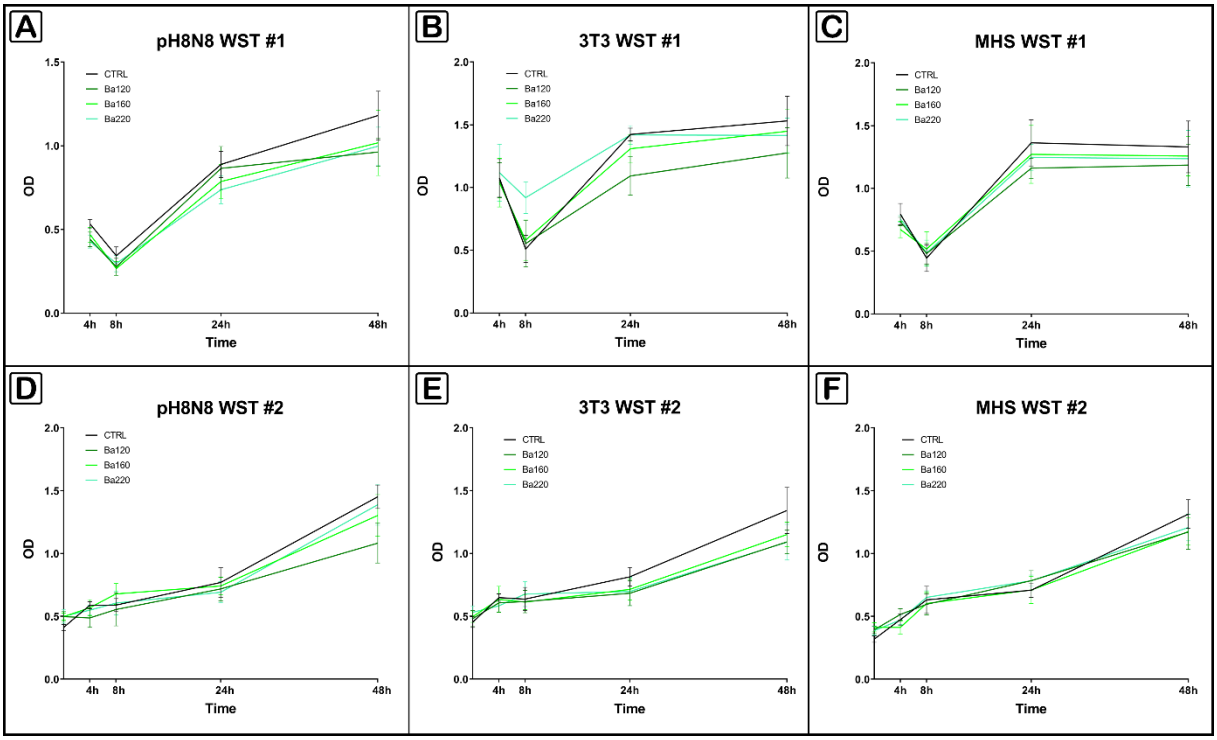

Figure 12: ***Cell viability of different cell lines in response to BaNPs.***

WST assay using BaNPs with different diameters. Graphs show the corrected ODs over time. A)+D) WST assays using pH8N8 mouse breast cancer cells. B)+E) WST assays using 3T3 mouse fibroblasts. C)+F) WST assays using MHS immortalized mouse macrophages.

4.2 Quantification of CT contrast enhancement of NPs

To satisfy the two purposes of radiation therapy and improvement of the tumor visualization in CT, the x-ray contrast of the NPs is of great importance. The contrast in CT is generated by the difference in x-ray attenuation between neighboring structures, which means by their difference in the absorption of x-rays. A strong absorption is not only important for the contrast but is also a key aspect to function as an efficient radiation therapy enhancer. Thus, I assessed the x-ray attenuation of four dilutions (1/10, 1/5, 1/1 and undiluted) of each of the three different BaNPs (BaNP-120, BaNP-160, BaNP-220) using the microCT. In addition, I used iodine containing NPs for comparison. I found that the highest x-ray contrast was achieved with BaNP-120, as can be seen in Figure 13 A, which shows the maximum intensity projections of the CT scans. A higher contrast is obtained at higher concentrations of the NPs. In Figure 13 B the results are displayed in terms of relative contrast agent concentrations. Despite being the smallest particle, BaNP-120 outperformed the other contrast agents in terms of relative contrast and was therefore selected for all following experiments.

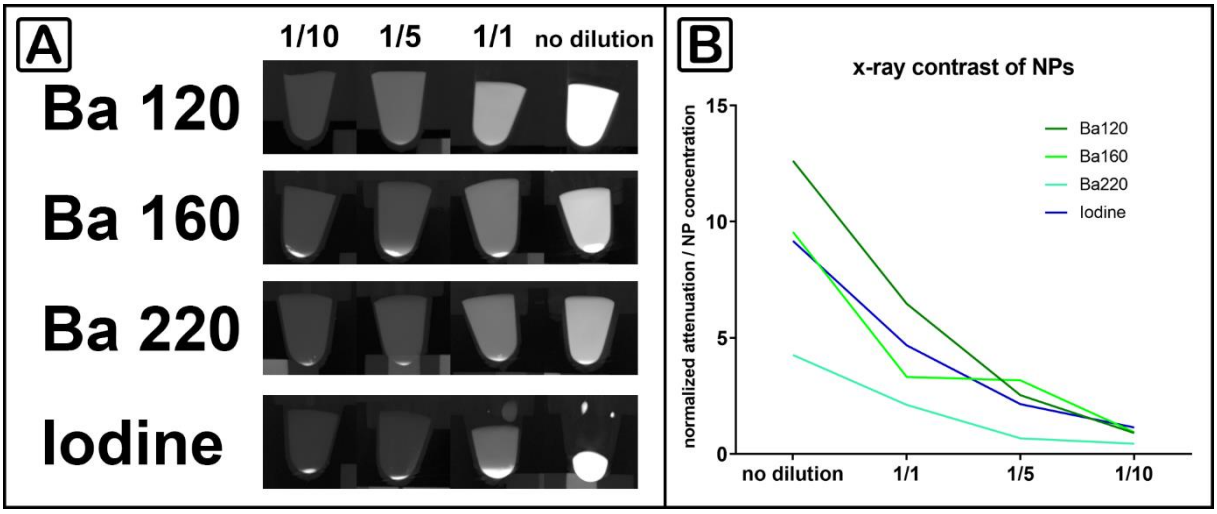

Figure 13: ***CT contrast enhancement of different NPs.***

A) Differently sized BaNPs as well as iodine NPs were imaged with the same imaging parameters later used for radiation therapy (QuantumFX, 90 kV, 200 µA, FOV 20mm, 2 min scan time). Stock particle solutions (BaNP-120 300 mg/ml, BaNP-160 300 mg/ml, BaNP-220 500 mg/ml, IodineNPs 220 mg/ml) and different dilutions in PBS were used. B) Plotted mean gray values of the data shown in A) reveals that BaNP-120 demonstrated the strongest x-ray contrast.

4.3 Dose calibration for in vitro irradiation with the microCT

Since there were no calibrated dose measurements available for our preclinical microCT system, it was necessary to evaluate the dose generated by the system at different parameters as a prerequisite for the following in vitro irradiation experiments. To achieve this, I used a dosimetric device which is usually used to perform consistency measurements for clinical CT scanners. The device measures the dose length product (dose integrated along one dimension of the irradiated area). The measurement probe was placed in the isocenter of the CT system and different acquisition protocols were performed. The results are shown in Table 16. For a standard CT acquisition protocol using 90 kV tube voltage, 200 µA tube current, 2 min scan time and a FOV of 20 mm dose values of 2.7 Gy were measured. The system can generate data sets at different resolutions, which is achieved by geometric magnification. Thus, to achieve a higher resolution, the x-ray tube is moved closer to the object/mouse while the distance between source and detector is kept constant. Since radiation intensity reduces with the distance to the power of 2, the scans performed at lower FOV generated a higher dose. Therefore, the values of measurements taken at larger FOVs (2 min, 90 kV, 200 µA, 73 mm FOV) of 0.95 Gy were in line with the expectations. The dose is linearly proportional to the tube current which can

also be seen in Table 16, since measurements at 100 µA tube current (2 min, 90 kV, 100 µA, 20 mm FOV) show values of 1.3 Gy, which is half the x-ray dose measured at 200 µA. In addition, we confirmed that the irradiated region is not much larger than the FOV by using an x-ray sensitive film. Thus, a 2 min scan at 90 kV and 200 µA at FOV 20 mm results in an absorbed dose of approximately 1.3 Gy.

Table 16: ***Dose length product measurements of the in vivo microCT with different acquisition parameters***

t [min]	kV	µA	FOV [mm]	Dose length product [Gy x cm]
2	90	200	20	2.692
2	90	200	20	2.685
2	90	200	73	0.9545
2	90	200	73	0.9506
2	90	100	20	1.322
2	90	100	20	1.316
2	90	200	40	1.386
2	90	100	40	0.6724

4.4 Quantification of the X-ray irradiation effect on tumor cell survival

Radiation damage of cells is commonly analyzed by performing colony forming assays as described in the method section 3.6. In short, the irradiated cells were plated and left to proliferate for 7-10 days. Then their ability to form colonies – clusters of 50 cells and over - were analyzed. To bypass the very time consuming and subjective manual counting of colonies using a microscope, I developed a new analysis pipeline using a flatbed scanner to image the cell culture plates in combination with a self-made quantification software.

4.4.1 Establishment of an automated quantification approach for colony forming assays

To quantify the number of colonies as well as their area I developed an image analysis software based on MATLAB. The code is publicly available and can be found under https://github.com/xPITcoding/CFA_analyze_plate. The workflow of the software is shown in Figure 14. The software allows to import a 16-bit *.tif image of a 6 well plate. To identify the wells, the image is downscaled by a factor of five and binarized using a gray value threshold of 35000. Subsequently an automated circle detection utilizing a circle Hough Transform was used to detect the coordinates and the radius of each well. A circular mask is generated with a radius which is 150 px smaller than the detected circle. Following this step, each single well is cut out from the original 16-bit data and the wall of the well is removed by applying the circular mask. A background correction is performed using a filtered version of each well (Gaussian filter, σ=100) and subtracting it from the image to remove shading and incorrect lighting. To segment the cells as colonies and not as single cells, the images are binarized, using a set threshold. Then a closing filter is applied to merge all pixels that belong to a single colony. To count the colonies subsequently an algorithm based on region growing is used. In short, a region growing algorithm can segment structures by checking a similarity criterion to neighboring pixels, in this case a low variation in their gray values. In addition, the function allows to exclude clusters which have insufficient size. The number of colonies, as well as their area and average brightness in the original data is exported as a *.csv file.

This approach allows the analysis of a six-well plate in a matter of seconds. In addition, images of all wells and their processing steps are saved, to check the reproducibility of the results.

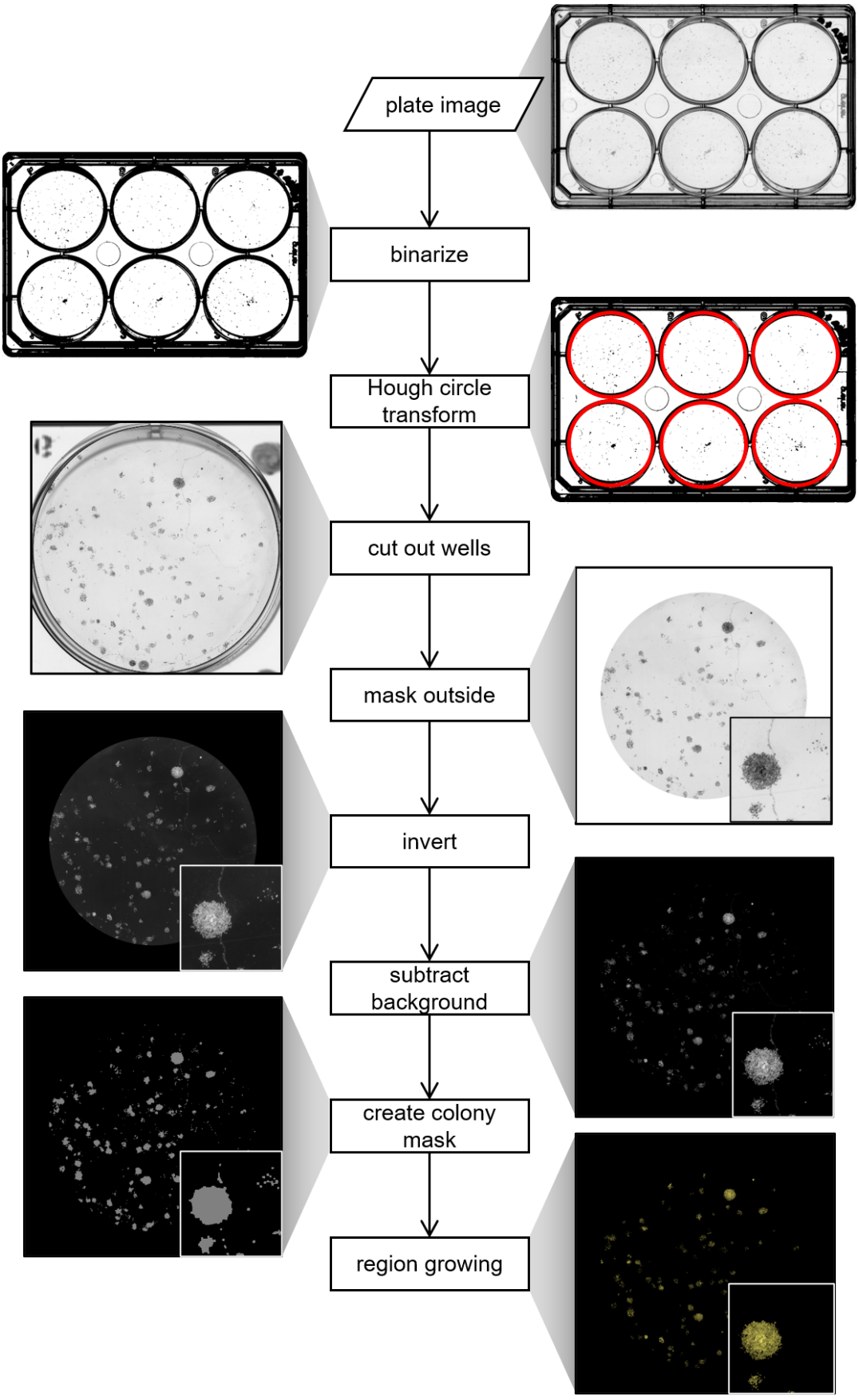

Figure 14: ***Flowchart of the automated colony forming assay analysis software written with MATLAB.***

4.4.2 Quantification of the in vitro irradiation effects of BaNPs

To test the influence of low energy x-ray irradiation on the survival of cancer cells and the ability of the BaNPs to enhance this effect, an in vitro irradiation study was performed. BaNP-120 solution was added to a cell pellet of murine pH8N8 breast cancer cells or human A549 lung cancer cells inside a micro reaction tube and irradiated in the microCT two times for 2 min, resulting in a dose of approx. 2.6 Gy Following this step, the cells were counted and seeded into 6-well plates and left to form colonies. The novel pipeline described above was utilized for the analysis of the colonies. The experiment was performed two times with the murine pH8N8 cells and two times with the human A549 cells. In each experiment, the cells were divided into four groups: the control group, CTRL represents cells that did not receive NPs and were not exposed to radiation, NP CTRL received NPs but no radiation, RAD were irradiated but did not receive NPs and NP RAD received both NPs and irradiation. One 6-well plate was used for each group and experiment. Figure 15 illustrates the outcome of the experiments. The bars show the relative difference to the mean of the respective CTRL group in each individual experiment.

Figure 15 A shows a significant reduction in the number of formed pH8N8 colonies for the NP RAD group in comparison to all other groups. The RAD group without BaNPs also shows a significant reduction in the colony number. But this reduction is only around 20 %, while the reduction in the NP RAD group is greater than 90 %. The NP CTRL group also shows a rather small but significant reduction in the colony number. Since the WST assay did not show any toxic effect of the BaNPs on pH8N8 cell proliferation, this result is most likely not due to toxic effect of the BaNPs, but rather due to the fact that the presence of BaNPs hampered the dissociation to single cells during the seeding process. As indicated in Figure 15 E, the colonies in the NP CTRL group were not as homogeneously distributed over the area of the well than in the other groups. This trend was similar for the analysis of the colony area, revealing an even larger area of colonies for the NP CTRL group than the one of the CTRL group (Figure 15 C). The colony area of the pH8N8 cells in the NP RAD group is also drastically reduced when compared to the other groups. Irradiation of A549 lung cancer cells revealed comparable results to those with pH8N8 cells, as evidenced in Figure 15 B and D. There is a highly significant reduction in both colony number and area even of the NP RAD group, although the enhancement effect of the BaNPs is not as dramatic as for the pH8N8 cells. Figure 15 E shows four exemplary wells of treated pH8N8 cells. The cells that are marked in red represent the automatically detected colonies. Bright gray cells/structures were not counted because they did not fulfill the size and roundness criteria of the analysis.

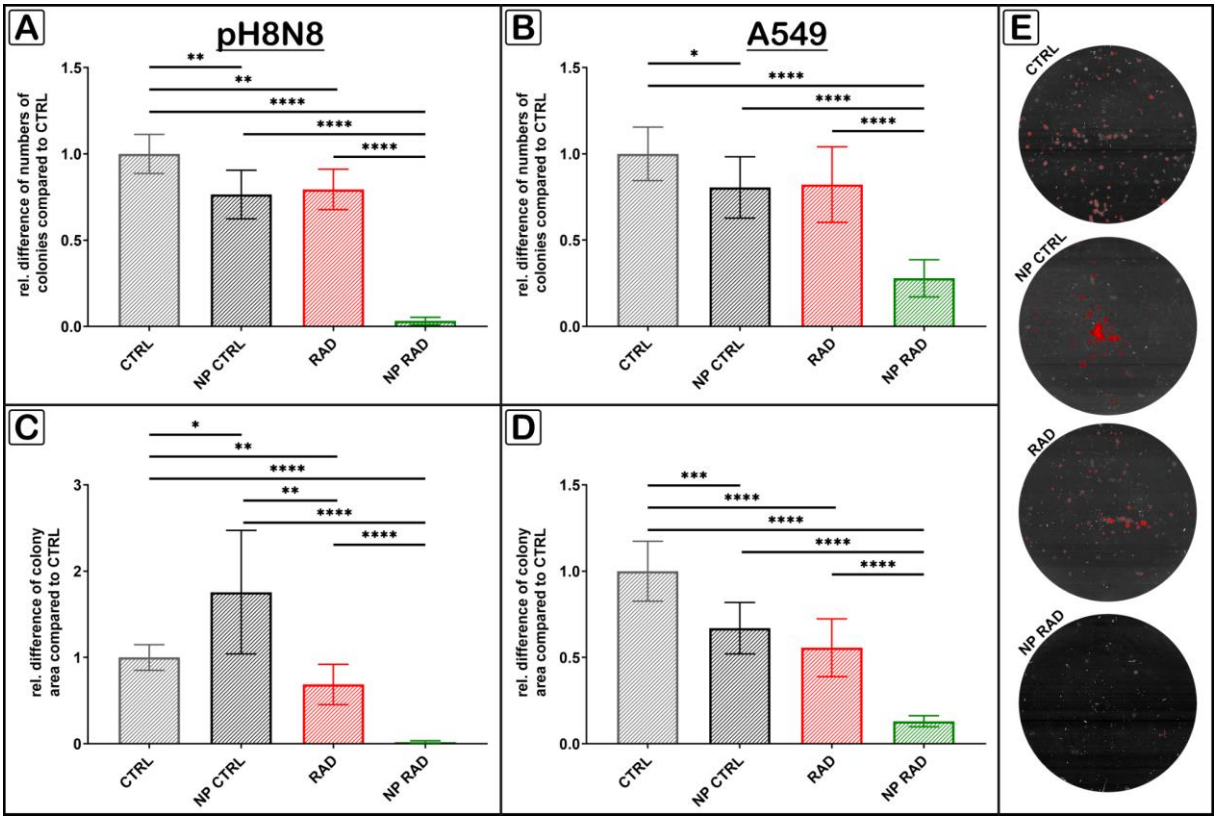

Figure 15: ***Irradiation enhancement effect of BaNPs in vitro.***

In vitro irradiation was performed for murine pH8N8 cells and human A549 cells and the following groups were compared. CTRL (no irradiation, no NPs), NP CTRL (no irradiation, NPs), RAD (irradiation, no NPs) and NP RAD (irradiation, NPs). A) Relative difference of colony number compared to CTRL group for pH8N8 breast cancer cells (n=12). B) Relative difference of colony number compared to CTRL group forA549 lung cancer cells (n=12). C) Relative difference of colony area compared to CTRL group for pH8N8 breast cancer cells (n=12). D) Relative difference of colony area compared to CTRL group for pH8N8 breast cancer cells (n=12). E) Exemplary images of segmented colonies of pH8N8 cells for each treatment group. Segmented colonies are pseudo-colored in red.

4.5 In vitro evaluation of tumor cell specificity of Ba120-EpCam-A594 NPs

To improve the BaNP enrichment in the tumor after systemic administration, BaNPs were functionalized with an antibody targeting a tumor associated protein. To this end, anti-EpCAM antibody (Ab) was chosen for functionalization of BaNPs, as previous studies showed a high expression of EpCAM in pH8N8 tumors[111]. Additionally, the BaNPs- EpCAM antibody construct was labeled with the fluorescent dye Alexa594 to enable microscopic analysis. To

validate that the Ab binds to the tumor cells, we performed in vitro cell culture assays with the free anti-EpCAM-A594 Ab as well as the Ba120-EpCam-A594 conjugate. These demonstrated a clear signal located at the cell membrane of the tumor cells for both assays, as representatively shown in confocal microscopy images of pH8N8 tumor cells of Figure 16. The Ab signal is depicted in yellow/orange, while the cell nuclei are stained with Hoechst dye and shown in blue. For the Ba120-EpCam-A594 conjugate some signal can also be found inside the cells, hinting at an internalization of the labeled BaNPs.

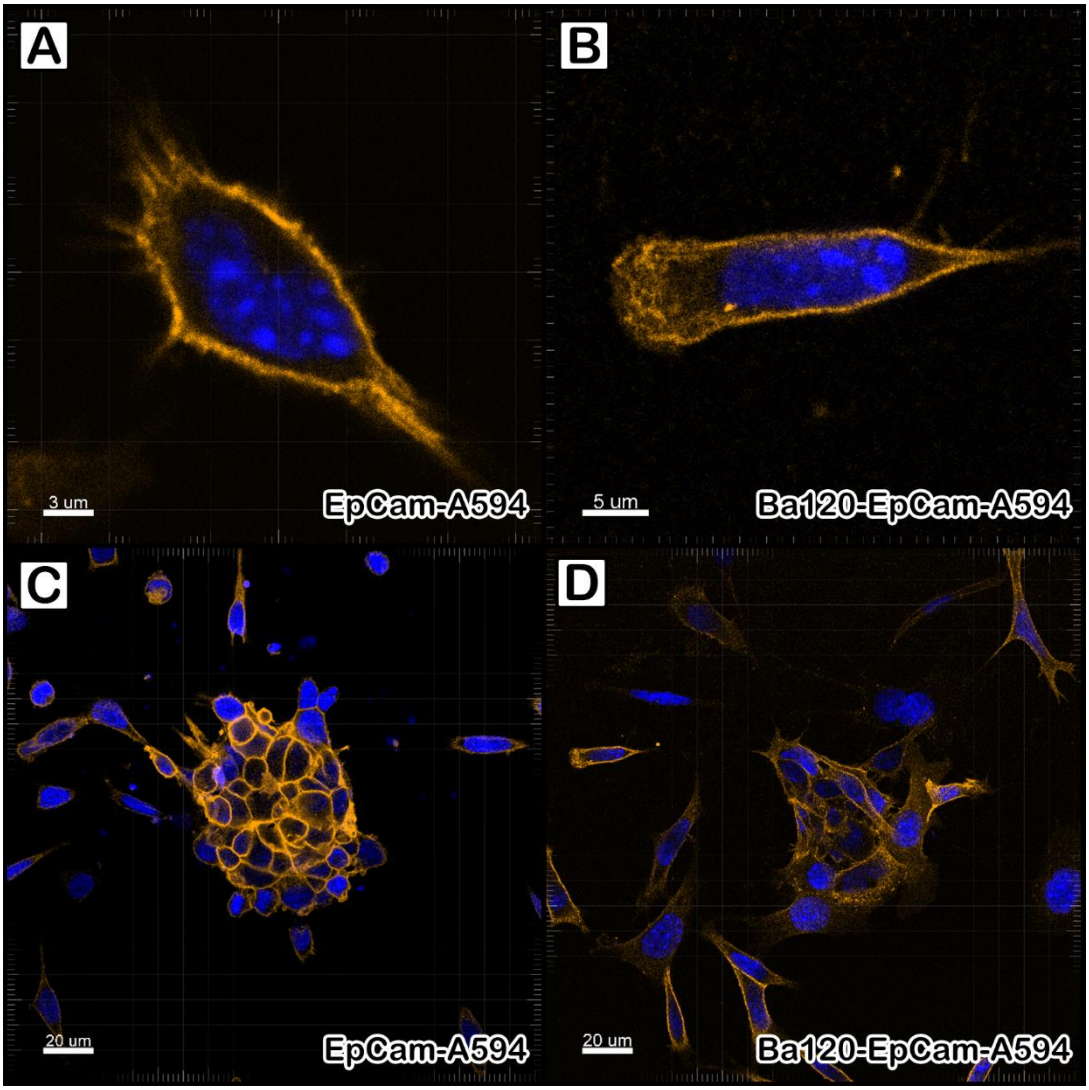

Figure 16: ***Confocal microscopy of pH8N8 breast cancer cells using fluorescence labeled anti-EpCam antibodies.***

A)+C) Representative images of H8N8 breast cancer cells incubated overnight with free EpCam-A594 antibody (yellow/ orange signal) show a specific binding of the antibody to the tumor cell membranes. B)+D) pH8N8 breast cancer cells incubated overnight with Ba120-EpCam-A594 BaNPs (yellow/ orange signal) show an enhanced fluorescence signal at the cell membranes as well as fluorescence signal inside the tumor cells hinting at internalization of the Ba120-EpCam-A594 particles. Cell nuclei are stained with Hoechst dye and depicted in blue.

Specific binding of EpCAM-A594 antibody to tumor cells was also confirmed in pH8N8 tumor cryosections. Representative confocal microscopy images in Figure 17 clearly show a strong signal at the cell membranes of the pH8N8 tumor cells. These results demonstrate that the generated Ab-labeled BaNPs specifically bind to the tumor cells.

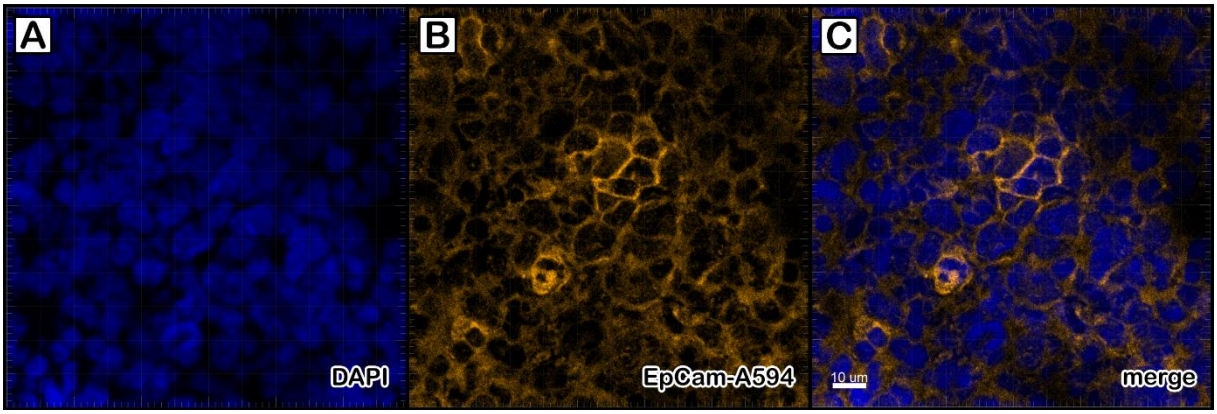

Figure 17: ***Confocal microscopy of pH8N8 tumor slices using Alexa594 labeled anti-EpCAM antibodies.***

Confocal microscopy of a tumor cryosection. A) DAPI stained cell nuclei depicted in blue. B) EpCAM-A594 signal depicted in yellow/orange. C) merge of A) and B) showing the antibody binding to the tumor cell membranes.

In summary the in-vitro analysis identified the BaNP-120 as the particles with the highest relative contrast, together with no signs of toxicity. BaNP-120 showed very promising results in RT in vitro and was therefore selected for in vivo testing.

4.6 Setup of an in vivo microCT radiotherapy approach

In order to perform RT with the in-vivo microCT system, I developed a dedicated mouse holder as shown in Figure 18 A. The system is based on a plastic pipe and equipped with a mask for isoflurane anesthesia. Two cylindrical covers made from 3 mm thick lead can be adjusted to protect the organs from radiation and only expose the tumor. A third piece of lead is used to counterbalance the setup. 3 mm of lead causes 100% attenuation of x-rays in the energy range produced by the QuantumFX x-ray tube. As the irradiation of the tumor is done by CT, meaning the x-ray tube is rotating around the mouse, the contralateral side will also receive the same radiation dose. Shielding the contralateral side - while feasible - would obviate a 3D image from the data and therefore prevent the use of the approach for a combined diagnosis and treatment. Intensive dose measurements were then performed to further characterize the setup.

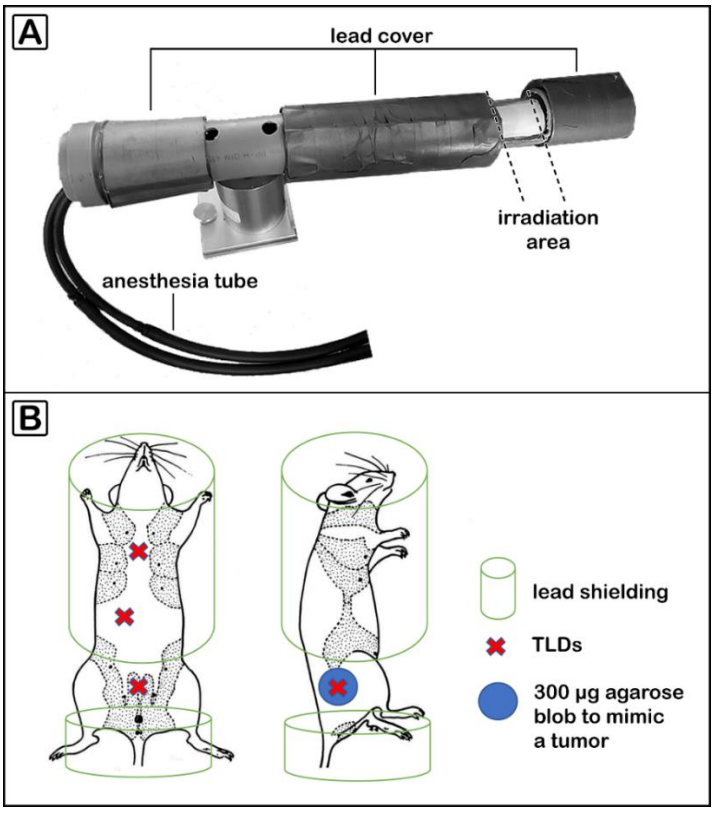

Figure 18: ***Preparatory work for radio therapy experiments.***

A) Custom made mouse holder for irradiation. Lead is used to shield all areas of the mouse outside of the tumor region. An anesthesia mask is integrated for isoflurane anesthesia. B) Dose measurement setup. TLDs were implanted into dead mice as shown and the position of the mouse holder is indicated. Agarose blobs were injected subcutaneously in the flank of the dead animal to mimic a tumor. The TLDs were implanted under the agarose blob.

In order to test the functionality of the mouse holder / shielding device and to obtain an estimate of the dose inside the tumor, thermoluminescence dosimeters (TLDs) were implanted at different positions into five dead mice as indicated in Figure 18 B. TLDs implanted in either the chest or the liver region were behind the led shielding and therefore expected to not receive any irradiation dose. The bladder region was used as a control region for healthy tissue that is within the unprotected FOV. The hind limb region was used to mimic the tumor location. For this purpose, 300 µL of agarose gel was injected subcutaneously in the flank of the mice to act as an artificial tumor. Two of the mice received the agarose gel mixed with 15 µL of BaNP-120. The results of the TLD measurements are summarized in Table 17. On average the hind limb region received a dose of approximately 1.4 Gy within 125 s. Given the fact, that the FOV or more precisely the irradiated FOV, is slightly larger than 20 mm, the result matches exactly the preceding measurements of the dose length product. In the two cases (mouse 1 and 2) in which the agarose gel was mixed with BaNP-120, the TLD measurements show slightly lower dose values. This suggests that compared to the artificial tumors without BaNPs, a higher percentage of radiation is absorbed in the presence of the particles and therefore does not reach the TLD. Contrary to the expectation, the TLDs labelled “Chest” and “Liver” demonstrated values of approximately 1% of the readings at the artificial tumor site. There are three effects that can account for this observation: I) scattering of the x-ray occurs within the mouse which can even reach locations protected by the lead cover, II) the TLDs may also see all other sources of radiation especially during their shipment from the Synchrotron (Trieste, Italy) to Göttingen and back and III) there may be a sensitivity threshold in the readout of the TLDs. However, a reduction of the radiation by 99% should keep harmful effects in the protected regions in the mouse to a minimum.

In summary, the TLD measurement confirmed the in vitro measurement of the dose length product. The small diameter of the mouse did not influence the dose distribution, because no scattering occurred. The CT system can be used to deliver a dose of approximately 1.4 Gy for a 2 min scan. Thus, by combining multiple scans, a sufficient dose for RT can be generated.

Table 17: ***Dose measurements of TLDs implanted into dead mice***

	Weight [g]	Time [s]	TLD Chest	Dose [Gy]	TLD Liver	Dose [Gy]	TLD Bladder region (Subq)	Dose [Gy]	TLD hind limb (Subq)	Dose [Gy]	300 µg Agarose Tumor
Mouse 1	38.5	125	A5	0.0098	A8	0.0263	A6	1.4733	A0	1.3587	+15µL BaNPs
Mouse 2	45	30	B5	0.0017	A3	0.0034	B8	0.2980	A7	0.2360	+15µL BaNPS
Mouse 3	40.7	30	A1	0.0032	B7	0.0058	B3	0.4127	B9	0.2969	
Mouse 4	40	125	B4	0.0090	A4	0.0332	A2	1.2651	B1	1.3824	
Mouse 5	38.3	125	B2	0.0143	B0	0.0669	A9	1.3512	B6	1.3802	

4.7 Analysis of BaNP distribution and fate after intratumoral application

In order to generate an effective RT strategy, a specific homogenous enrichment of BaNPs in the tumor must be achieved. In addition, it is important to know if the BaNPs are excreted or where they remain in the body. The data sets shown here were generated in the first irradiation experiment which is shown in section 4.8.1 below. Human A549 tumor cells were subcutaneously injected in the flank of the mice. 30 µL BaNP-120 was injected intratumorally once 24 h before the first treatment when the tumors reached a size of 300 mm^3. Since the mice were irradiated using a standard acquisition protocol of the in vivo microCT (90 kV tube voltage, 200 µA tube current, FOV 20 mm, 2 min scan time), 3D volume data sets were generated during the therapy. Six therapy sessions were performed every second day. Figure 19 A shows 3D renderings of the tumors and the BaNP distribution at each therapy session. Two general distribution patterns were found: intra-tumoral distribution of the particles and cases in which the NPs were mostly enriched in the capsule. However, in both cases there was virtually no change in the local distribution over the entire duration of the experiment. This is further illustrated by two exemplary tumors in Figure 19 B showing that the volume of particle enriched regions of the tumor remains constant over time. Therefore, it can be concluded that the BaNPs remain at their injection site over two weeks until the end of the experiment.

In addition, I did not find any BaNPs in other organs, which were scanned in the CT and analyzed by histology after explantation. In summary, the distribution of the particles in the tumor was inhomogeneous but static over time.

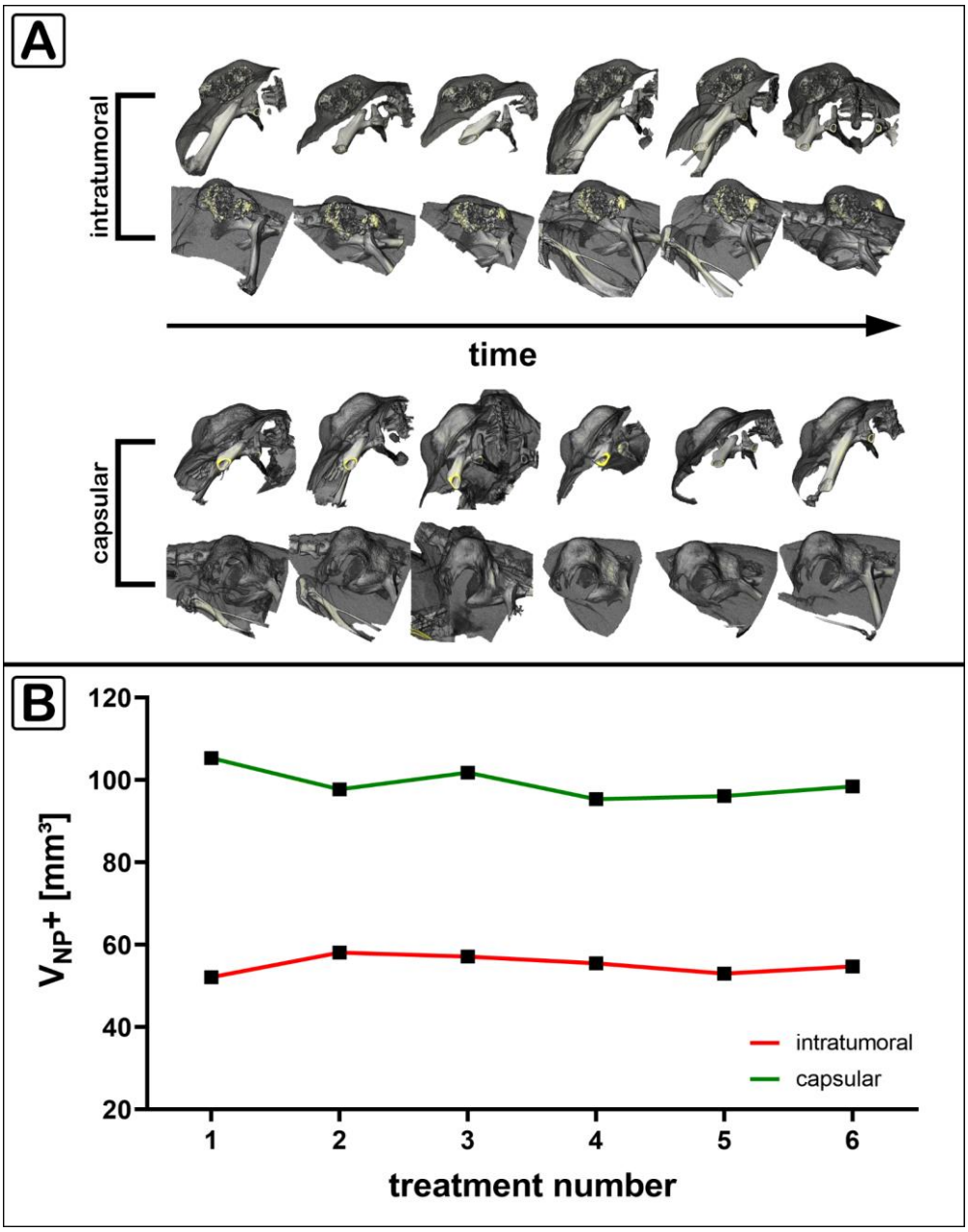

*Figure 19**: Fate of BaNPs after intratumoral application in subcutaneous A549 lung tumors.***

Subcutaneous A549 lung tumors after i.t. application of 30 µl BaNPs. A) 3D renderings of microCT data sets acquired during RT. Two tumors are visualized from two different angles at six different time points. Upper panel exemplifies a tumor with intratumoral accumulation of NPs; lower panel exemplifies a tumor with accumulation of NPs in the tumor capsule. No visual difference in the NP amount or distribution was observed over time. B) Segmented NP-positive volume (V_{NP+}) over time. No changes can be found.

4.8 NP enhanced low energy RT performed in an in vivo microCT

In vivo experiments were conducted that followed the workflow presented in Figure 20, except for panel D - the bioluminescence measurement - which was only performed in the last experiment. The first experiment was conducted on subcutaneously implanted lung cancer cells (A549), the latter three on orthotopically implanted breast cancer cells (pH8N8). For all experiments, following the implantation (Figure 20 A), the size of the tumors was continuously evaluated using a caliper (Figure 20 C). When tumors reached a size of 300 mm^3, the mice were randomly assigned to one of the therapy groups and BaNPs were injected intratumorally (Figure 20 B). Irradiation was performed with the QuantumFX in-vivo microCT system at an energy of 90 kV. The details and the results for the specific experiments are given in the following chapters.

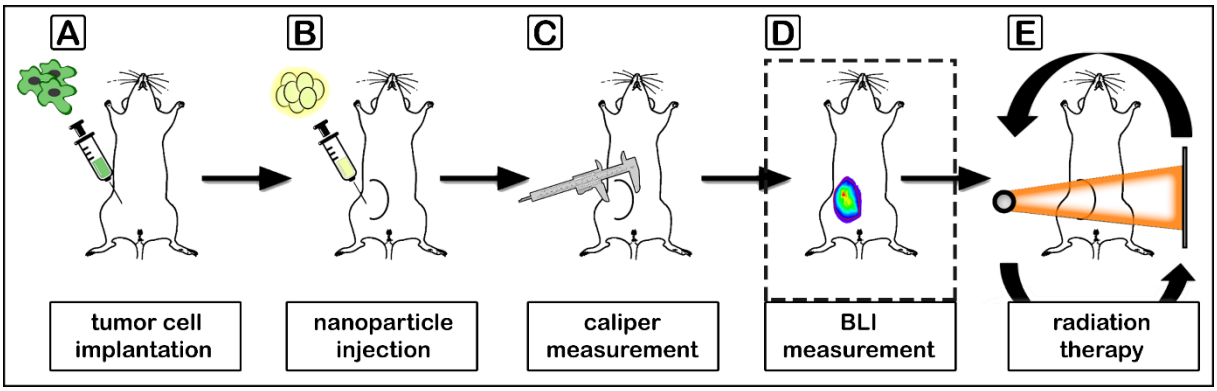

Figure 20: ***Workflow of the irradiation experiments****.*

A) Implantation of tumor cells. B) Intra tumoral injection of 30 µl BaNP solution. C) Manual caliper measurements for tumor volume assessment, performed by 2-3 readers. D) Measurement of BLI intensity. BLI measurements were only performed in the fourth experiments. E) RT performed in the in vivo microCT.

4.8.1 Preliminary evaluation of the therapy approach using a subcutaneous lung cancer model

To evaluate a NP-enhanced RT approach we initially thought of using a subcutaneous tumor model that provides the advantage of directly injecting the BaNPs into the tumor and easy tumor measurements by caliper. For this purpose, A549-cell induced subcutaneous tumors were irradiated six times every second day using four consecutive CT scans of 2 mins at 90 kV and 200 µA resulting in a dose of about 5.5 Gy per session and a total dose of ~33 Gy. Mice were randomly assigned to four groups CTRL (no NPs, no irradiation, N=4), NP CTRL (NPs, no irradiation, N=5), RAD (no NPs, irradiation, N=5) and NP RAD (NPs and irradiation, N=5). Tumor size was monitored by caliper measurements by two readers every second day. Body weight was also measured every second day.

The selected irradiation schedule revealed no significant adverse effect on the body weight, es demonstrated in Figure 21 A, which shows changes in body weight at the end of the experiment in comparison to the date of tumor cell implantation. Both non-irradiated groups (CTRL & NP CTRL) gained weight of approx. 5-7 %, suggesting no harmful side effects of the BaNPs on the wellbeing of the mice. Mice of both irradiated groups did not show any weight loss, indicating no severe side effects. The starting point of the experiment was defined as the day when the tumors reached a size of 300 mm^3. Since the individual tumors showed very different growth kinetics, the animals were divided into 5 different cohorts. The treatment group of each mouse was randomly assigned independently of the cohort. Figure 21 B shows the measured tumor volumes for each mouse over time. Figure 21 C shows the relative change in tumor volume in comparison to the day of BaNP injection.

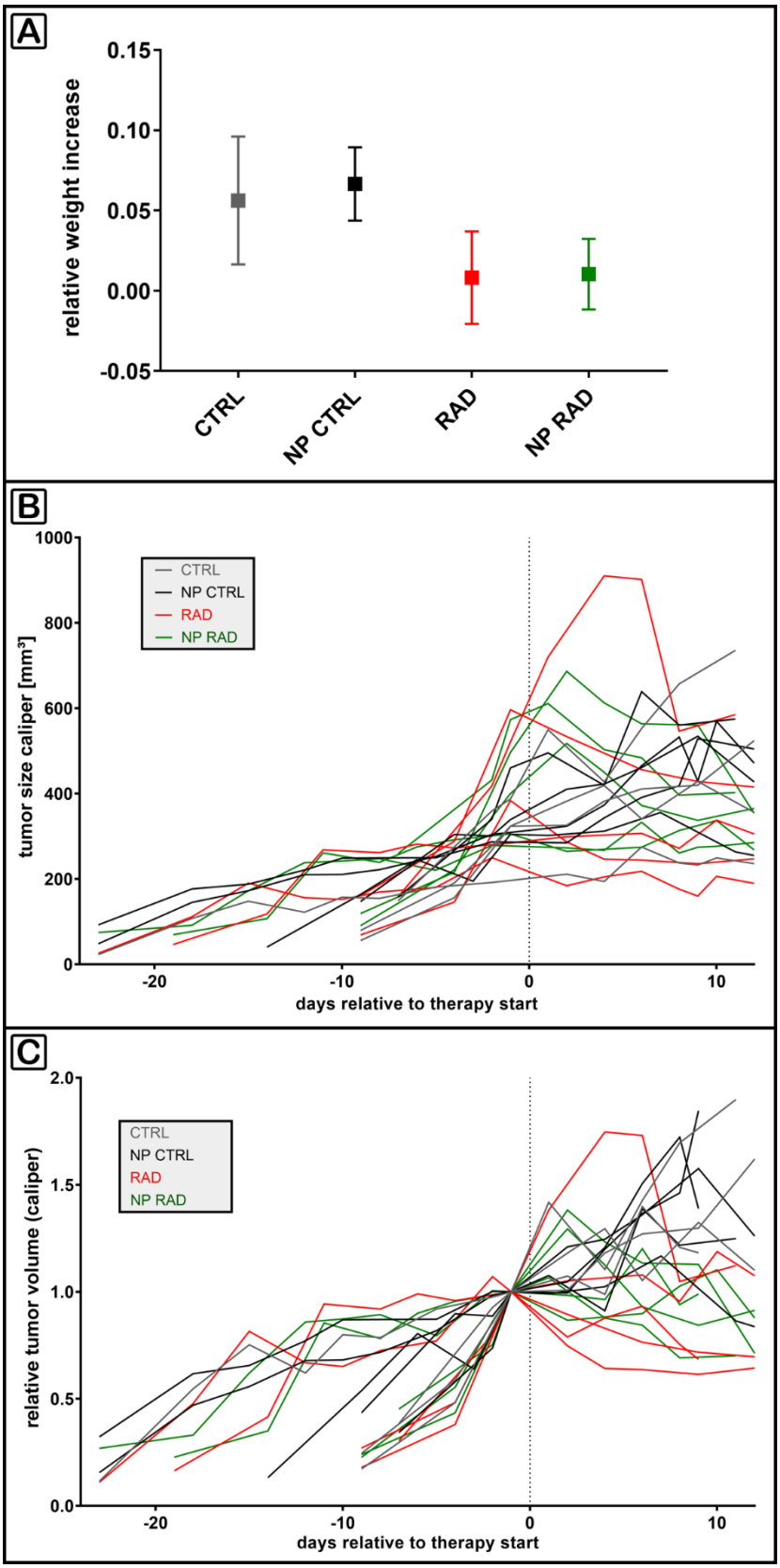

Figure 21: ***Results of the first irradiation experiment.***

A) Mean weights over time for each treatment group. No significant weight loss was observed in any of the groups. B) Tumor volumes over time relative to the therapy start. C) Relative tumor volumes in comparison to the day of NP injection (day -1) over time.

Interpretation of the graphs shown in Figure 21 B and C is rather difficult, because of the different growth kinetics, treatment dates and the large standard deviations of the caliper measurements. Therefore, Figure 22 shows the tumor volumes over time in the different treatment groups.

As shown in Figure 22 A and B the tumor volumes in both control groups (CTRL & NP CTRL) increased steadily over time. In contrast, we found that in both irradiated groups (RAD & NP RAD) the tumors shrunk, or the tumor growth was minimized (Figure 22 C and D). The effect can be observed 3-4 days after therapy start and is stronger in larger or faster growing tumors. No apparent difference was detected in the tumor volume kinetics after treatment between the RAD and the NP RAD group.

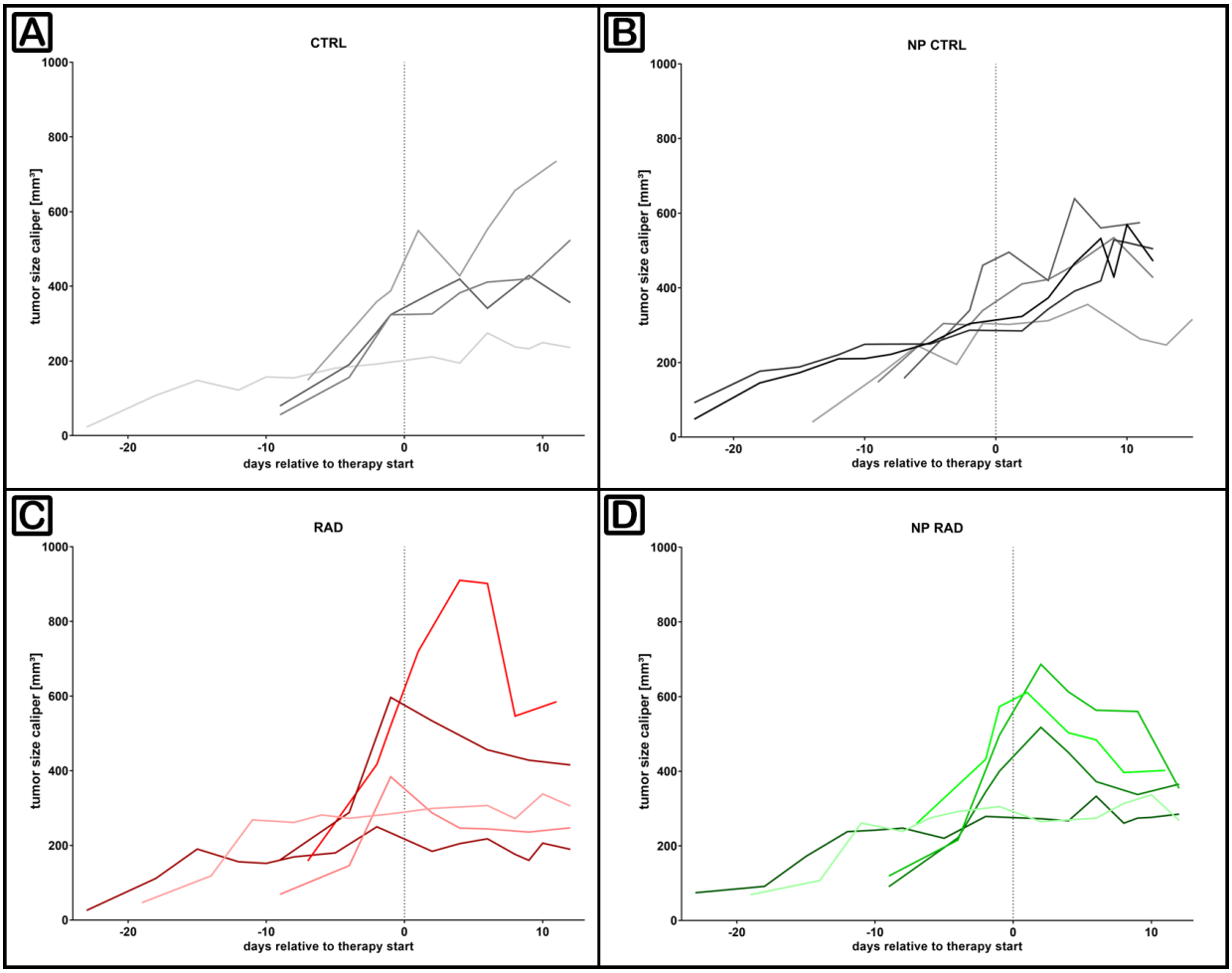

Figure 22: ***Growth kinetics over time as a result of radiotherapy divided into the treatment groups.***

Tumor volumes for individual animals over time measured by manual caliper measurements. A) CTRL group (no radiation, no BaNPs; N=4). B) NP CTRL group (no radiation, BaNPs; N=5). C) RAD group (radiation, no BaNPs; N=5). D) NP RAD group (radiation & BaNPs; N=5). Both non-irradiated groups show a steady tumor growth, while the irradiated tumors show a decrease in tumor volume due to the therapy.

In summary, this pilot experiment provided evidence that RT can be indeed performed successfully in a CT. However, it also showed experimental flaws, which most probably contributed to non-statistically significant results as tested by ANOVA. In particular, the measurement of the tumor by caliper is difficult to reproduce and especially challenging for small tumor volumes despite the superficial nature of the subcutaneous lung tumors. The current experimental numbers and set-up did not show a strong increase in the efficacy of RT based on the presence of NPs. We cannot exclude smaller differences in the tumor growth between RAD and NP RAD that were not measurable in these data sets.

In the following experiment, I optimized the treatment scheme and utilized the pH8N8 breast cancer model for TNBC.

4.8.2 Radiation therapy effect in the orthotopically implanted breast cancer model

Since the main aim of my thesis was to evaluate if NP-enhanced RT can be used as a therapy for TNBC, I used an orthotopic breast cancer model for further experiments, which provides a more disease-relevant environment for the assessment of tumor growth. In addition, the pH8N8 breast cancer cells are of murine origin and allow the use of immunocompetent mice, which is important because of the role of the immune system in response to cancer treatment. Moreover, as the current route for administering the NPs was intratumoral injection an application in breast cancer therapy seemed more likely than in lung cancer. Since neither the cell viability assays nor the mice in the control group (no BaNPs, no irradiation) in the previous experiment showed any signs of toxicity or altered tumor growth compared to the NP CTRL group which received BaNPs, I only evaluated the concept in three groups: NP CTRL (NPs, no irradiation, N=2), RAD (no NPs, irradiation, N=4) and NP RAD (NPs and irradiation, N=5).

The preliminary irradiation experiment did not show a strong difference in the tumor volumes when BaNPs where used in combination with irradiation. I therefore adjusted the irradiation schedule to achieve an increase in the NP-based RT effect. For this purpose, the same radiation dose of 5.5 Gy was delivered per treatment, but the schedule was changed to daily irradiation instead of every second day to give the tumor cells less time to repair the damage. Thus, seven therapy sessions were performed with four 2 min CT scans at 90 kV and 200 µA per session.

This treatment schedule resulted in a strong weight loss of up to 20% within 10 days of treatment in both irradiated groups (Figure 23 A) and led to a premature termination of the experiment. Figure 23 B shows the relative volumes over time in comparison to the treatment start. While the mice in the non-irradiated NP CTRL group exhibited a tumor volume increase up to a factor of five, the irradiated groups (RAD & NP RAD) displayed a therapy effect. In the RAD group the tumors grew similarly to the NP CTRL group until day five and then the tumors receded in size. When the experiment was terminated the tumor volumes were approximately the same as at the beginning of the experiment. The NP RAD group showed a slower tumor growth from the start of the experiment. The tumors also began to shrink after day 5. However, these differences between the RAD and NP RAD group were not significant

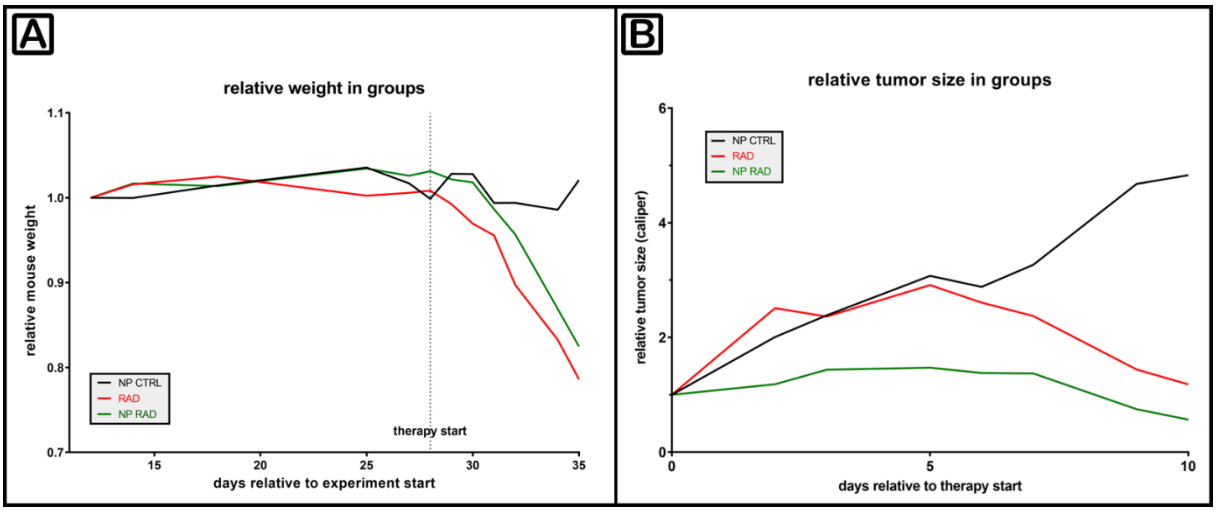

Figure 23: ***Outcome of radiotherapy using the orthotopic breast cancer model.***

Mean values for the following groups are depicted: NP CTRL (BaNPs, no irradiation; N=2), RAD (no BaNPs, irradiation; N=4) and NP RAD (BaNPs and irradiation; N=5). A) Mean relative weights over time for each treatment group. Significant weight loss in the treated groups. B) Tumor volume over time relative to the therapy start. Both treated groups show a reduction in tumor growth.

In summary, this experiment revealed a clear reduction in the pH8N8 tumor volumes in treated mice in comparison to the NP CTRL group, similar to the results we observed in the A594 subcutaneous tumors. However, a significant benefit of the BaNPs for reducing the tumor volumes was not detected. Due to the strong side effects of the irradiation dose, I decided to further optimize the treatment schedule by adding rest days with the aim to reduce side effects, while maintaining the effect of the RT.

4.8.3 Improving the treatment schedule to reduce side effects for radiotherapy of pH8N8 breast cancer bearing mice

The daily irradiation schedule as described in the previous chapter led to a significant weight loss of the mice due to applied irradiation dose of 5.5 Gy per day. To reduce these side effects, I adapted the treatment scheme to a protocol which is similar to irradiation of breast cancer residues in patients[30]. The mice were now irradiated for 5 consecutive days, followed by 2 days of rest. Furthermore, the dose per therapy session was reduced by 50% using only two 2 min CT scans at 90 kV and 200 µA which resulted in an applied dose of 2.7 Gy. In total 16 sessions were performed to reach a total dose of approx. 40 Gy. The same group design was kept as before, with an additional group using NPs with a larger diameter of 300 nm (NP_{300} RAD). I speculated that due to the rather small diameter of the BaNP-120 the effective cross section was too small, leading to the low efficacy.

As in previous experiments, the NP CTRL mice showed no weight loss (Figure 24 A). The mice in all three irradiated groups demonstrated a weight loss of up to 10% during the therapy days (marked by dotted lines), but a weight gain was observed during the days without treatment. The overall weight loss of the animals was smaller than in the previous experiment, even though the time period of therapy was much longer (Figure 24 A). The exclusion criterion of the ethics approval for the study of 20% weight loss was never reached. In addition, the mice showed significantly reduced signs of stress, such as minimally reduced activity, no diarrhea or dull fur. These results were also reflected in the absolute mean tumor volumes (Figure 24 B). The animals in the NP CTRL group showed continuous tumor growth. Since the therapy schedule was changed and the treatment period was longer, two NP CTRL animals reached the exclusion criterion for the tumor size (1500 mm^3) at day 18 and day 13 (indicated by the cross) and had to be sacrificed before the end of the experiment. The tumor volumes of the three irradiated groups started to decrease from day 7 onwards. When comparing the start tumor volumes (day 0, therapy start) and the end volumes (day 25), the volume decreased by 41% for the RAD group, 50% for the NP_{120} RAD group and 60% for the NP_{300} RAD group. However, there were no significant differences in the tumor volumes between the three groups as tested by ANOVA.

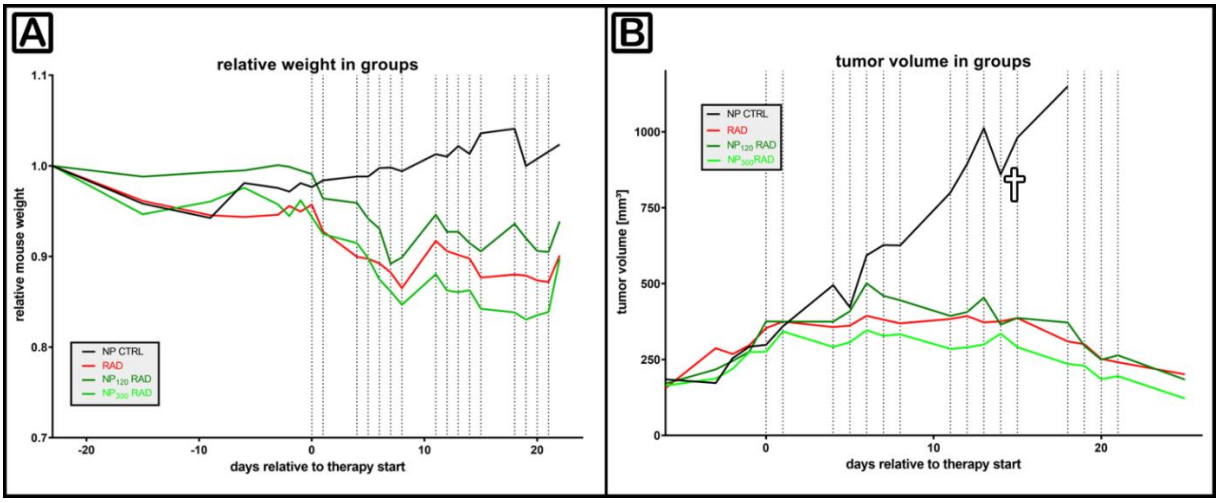

Figure 24: ***Outcome of radiation therapy in the pH8N8 breast cancer model using an improved treatment schedule***

Mean values are depicted for the following groups: NP CTRL (BaNP-120, no irradiation; N=4), RAD (no BaNPs, irradiation; N=4), NP_{120} RAD (BaNP-120 and irradiation; N=4) and NP_{300} RAD (BaNP-300 and irradiation; N=3). A) mean relative weights over time for each treatment group. B) tumor volume over time relative to the therapy start for each treatment group. All therapy days are marked by dotted lines. Irradiated mice show decreased tumor volumes after the onset of the therapy, while control tumors show continuous growth.

In summary, the results so far prove that low energy irradiation in an in vivo microCT can significantly reduce tumor growth and is well tolerated if an adapted treatment protocol is used. These optimizations include lowering the x-ray dose per session from 5.5 Gy to 2.7 Gy and irradiating the mice for five consecutive days followed by two rest days. Since the tumor volume measured by caliper was the only readout for therapy success, and this method does not take into account the viability of the tumor cells, I opted for a further improvement of read-outs by utilizing bioluminescent tumor cells to gain more information.

4.8.4 Utilization of bioluminescent pH8N8 breast cancer cells to gain more insights on radiation therapy effects

In previous experiments the only parameter for RT outcome was the manual measurements of tumor size with a caliper. Even when using multiple readers, this type of measurement has proven to be prone to large variations. To have another readout for the therapy success I therefore decided to use bioluminescent tumor cells, which provide the possibility to assess tumor progression based on their bioluminescence intensity. For this purpose, pH8N8 breast cancer cells were transduced with a lentiviral vector encoding for both luciferase and eGFP. Multiple clones were created and their bioluminescence intensity was measured ex vivo.

The cells were seeded into the wells at each corner of the plate and the total photon flux was measured 20-times with a one-minute interval after adding the luciferin substrate (Figure 25 A). The image shows the BLI signal of the first measurement in pseudo-colors, according to the color map on the right side (blue = low, red = high). Figure 25 B shows the total photon flux of the clones over a time span of 20 mins after the addition of luciferin. The clone 1G8 did not show any bioluminescence signal, while the three other clones showed a strong BLI signal. Clone 3D3 clearly demonstrated the strongest BLI signal.

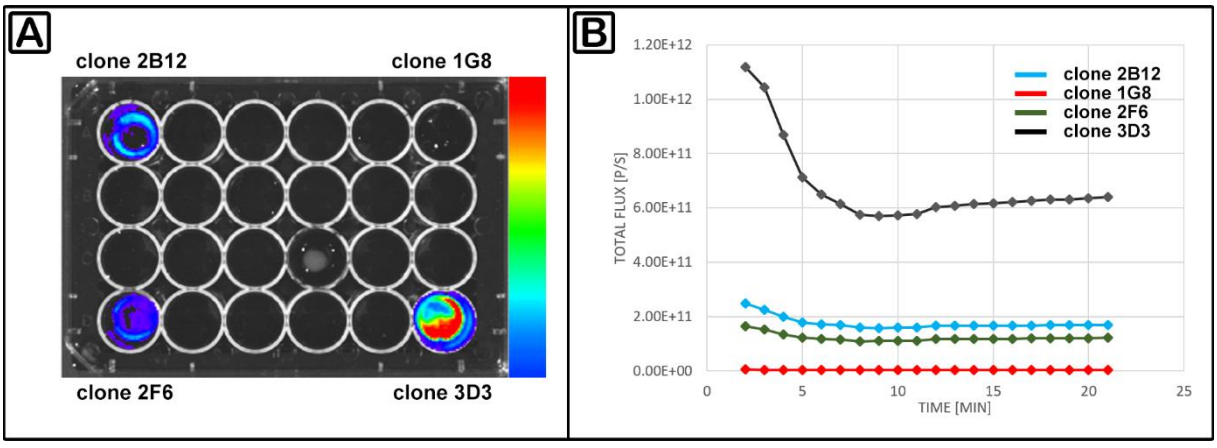

*Figure 25**: In vitro validation of bioluminescence of modified pH8N8 tumor cells.***

A) In vitro BLI measurements in a 24-well cell culture plate measured with the IVIS Spectrum device. B) Total flux values measured every min for 20 min after the addition of luciferin. The clone 3D3 shows the strongest signal. Clones 2F6 and 3D3 demonstrate a clear BLI signal while clone 1G8 shows no bioluminescence.

Clones 2F6, 2B12 and 3D3 were then orthotopically implanted into three WAP-T-NP8 mice each. The mice implanted with the clone 3D3, which showed the strongest in vitro BLI signal, did not develop any tumors. The remaining mice successfully developed breast tumors, which were large enough to be measured by caliper after three weeks. The tumor growth was monitored manually by caliper measurements (average of two readers) on the same days the BLI signals were measured.

As shown in Figure 26 A and B the BLI signal was measured seven times after the luciferin application to determine the time point of the maximum signal, which was detected at approximately 10 min after luciferin administration. Comparison of the caliper volume measurements (black) with the BLI total flux measurements (red) of both clones (Figure 26 C and D) demonstrated that the manual volume measurements and the BLI total photon flux showed similar trends. For further irradiation experiments I decided to use the clone 2F6, because the tumor growth was similar to the non-bioluminescent pH8N8 cell used before. In addition, the BLI signal of clone 2F6 was slightly stronger than for clone 2B12.

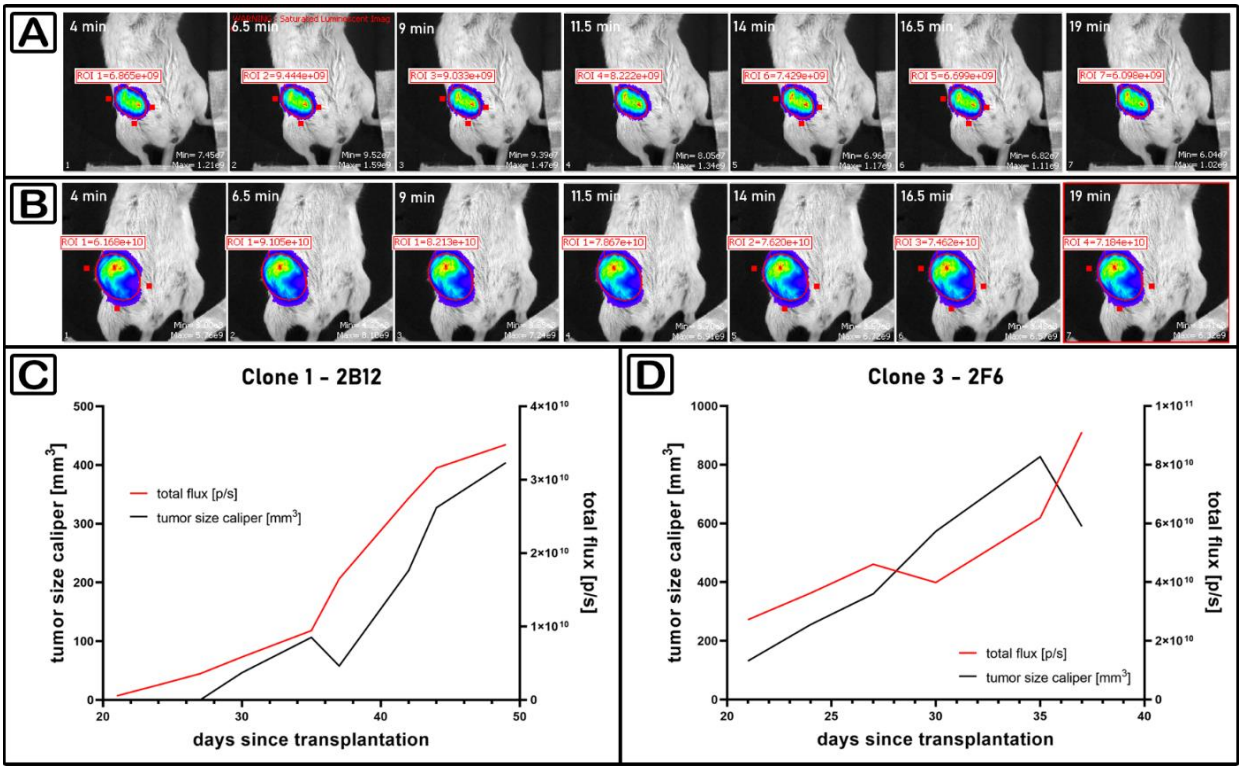

Figure 26: ***In vivo validation of bioluminescent pH8N8 breast tumor cells.***

Representative images of BLI measurements of breast tumors induced with pH8N8 clone 2B12 (A) and 2F6 (B) at 7 different time points after luciferin injection. Graphs comparing BLI total flux measurements and manual caliper measurements over time for the clone 2B12 (C) and 2F6 (D) demonstrating similar trends for both methods.

All irradiation experiments so far revealed that the data evaluation is impeded by multiple factors. Since the tumors show different growth kinetics the therapy start had to correspond to either a specific date or a specific tumor size. I chose the latter option since this should make the biological properties of the tumors more comparable. A consequence of this choice was that the mice entered the treatment at different time points. Furthermore, the additional BLI measurements increased the treatment time per animal and thus the total workload, which necessitated splitting the mice into treatment cohorts. In addition, the manual caliper measurements are prone to inter-observer variability. Collectively, these aspects make the manual comparison of the different data sets very complicated and labor intensive. Therefore, I decided to develop a software that can assist with sorting and filtering of the data. The principle workflow of the software is described in the following section.

All data points, such as the caliper measurements, the BLI data sets, as well as tumor size measurements based on the acquired CT data sets are imported as *.csv sheets. The mouse number and the date of the data acquisition is used to identify the data sets. Internally a database is created that holds all the information for each animal as demonstrated in Figure 27.

```
class Mouse
{
public:
    QDate _birth,_implantation,_NPInjection,_startDate;
    QMap <QDate,SizeMeasurement> _measurements;
    QMap <QDate,float> _weights;
    QList<IVISMeasurement> _IVISMeasurements;
    QMap <QDate,QList<IVISMeasurement>>_IVISdata;
    QMap <QDate,float> _CTmeasurements;
    M_COHORT _cohort;
    M_GROUP _group;
    QString _comment;
    int sectionNumber;
```

Figure 27: ***"mouse class" construct implemented in the analysis software.***

The class holds the date of each mouse specific parameter as well as each measurement (data type = QDate). In addition, the treatment group, cohort and section number are saved.

Figure 28 illustrates a simplified flowchart of the developed software. The created database can be saved to avoid importing all data sheets every time the software is used. To enable a better comparison of the animal in the different treatment groups the software supports normalization of the data sets to either the day of tumor cell implantation ("start day") or the day of the first therapy session ("therapy start"). In the next step the user manually filters which data is of

interest. If some data points are missing for the selected animals/ treatment groups/ cohorts, missing data points are interpolated using a simple linear interpolation algorithm. A moving average filter with a variable filter width can be applied to smooth the data if necessary. This is important for monitoring the trends of the data, due to the large standard deviations that can occur in both the manual caliper measurements as well as the BLI measurements. The selected data can be plotted, either over time or as a correlation plot. In addition, all values can be displayed as the absolute values or as a relative change in comparison to the "start day" or the "therapy start". The data points can be exported as a *.csv file for further analysis.

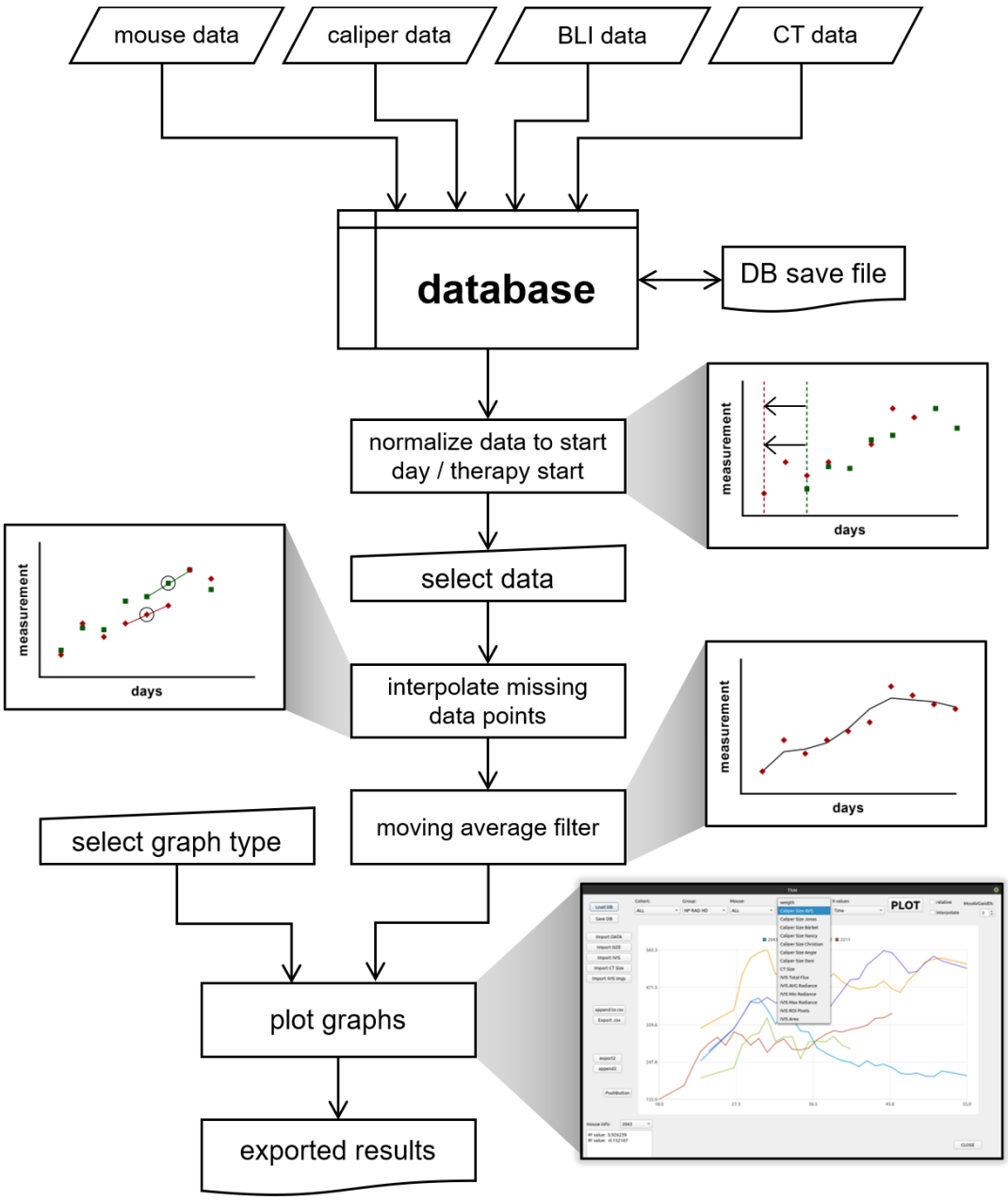

Figure 28: ***Flowchart of the software to analyze the effect of irradiation on tumor growth kinetics.***

The bioluminescent pH8N8 clone 2F6 and the aforementioned newly developed software were then used to evaluate a further optimization step in the RT regimen. So far, the RT experiments showed that the irradiation itself leads to effective RT using a microCT but did not reveal any difference between the irradiated groups, either treated with or without BaNPs. Because RT without BaNPs already significantly decreased the tumor volumes, I speculated that, at lower dose rates, a larger difference may be found between the RAD and NP RAD groups. Therefore, an additional group NP RAD LD was added, which only received 50% of the irradiation dose (LD = low dose, one 2 min CT scan at 90 kV and 200 µA; ~1.35 Gy/treatment) in comparison with the previously applied dose of 2.7 Gy/treatment, which is here referred to as high dose (HD). In order to provide a better readout of the radiation damage the pH8N8-BLI cells were used for the orthotopic tumor mouse model, since the BLI signal correlates well with the amount of living tumor cells. In addition, to improve the volume measurement on its own, I used the acquired CT data sets to also calculate the tumor volumes. However, this was not possible for the NP CTRL group which did not receive any CT scans.

The treatment schedule consisted of eight therapy sessions of two 2 min CT scans at 90 kV and 200 µA (except for the NP RAD LD group) (Figure 29). Due to the addition of BLI measurements the mice were analyzed in a multiplexed fashion (50% on one day, 50% on the second day and then starting with the first 50% again). Thus, a daily irradiation was not feasible, due to time constraints. The BLI measurements were performed immediately before the RT to avoid multiple anesthesia of the animals. Mice were again randomly assigned to four groups NP CTRL (NPs, no irradiation, N=4), RAD (no NPs, high dose irradiation, N=5), NP RAD HD (NPs, high dose irradiation, N=5) and NP RAD LD (NPs, low dose irradiation, N=4). The regular caliper tumor volume measurements were performed daily for each mouse by 2-3 different readers to minimize the measurement error.

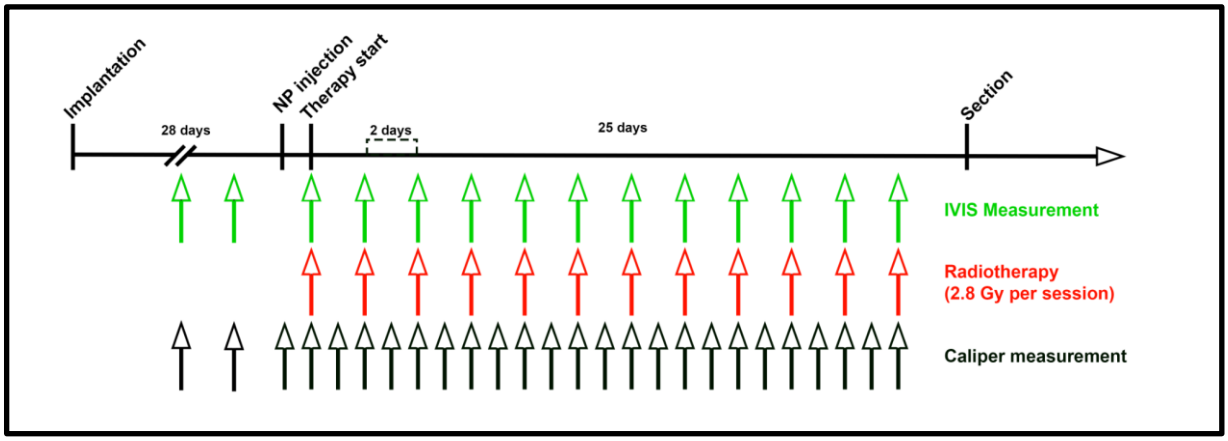

Figure 29: ***Optimized treatment schedule using bioluminescent pH8N8 tumor cells.***

The IVIS (BLI) measurements of the mice were performed immediately before radiation therapy every second day. Manual caliper measurements were performed every day by two to three different readers to reduce the measurement error.

Figure 30 A shows the body weights of the mice on the day of tumor cell implantation. While the variation in weight was relatively large (22-32 g) there was no significant difference in weight between the groups. Tumor volumes on the day of the first RT demonstrated no significant differences between the groups, as seen in Figure 30 B. This result was confirmed by the total flux values of the BLI measurements on the day of the first RT, with no significant differences found between the groups (Figure 30 C). Therefore, I can exclude any bias in the outcome of the experiment based on the assignment of the mice to the different groups. In addition, any differences in the outcome of the RT were not related to differences at the starting point.

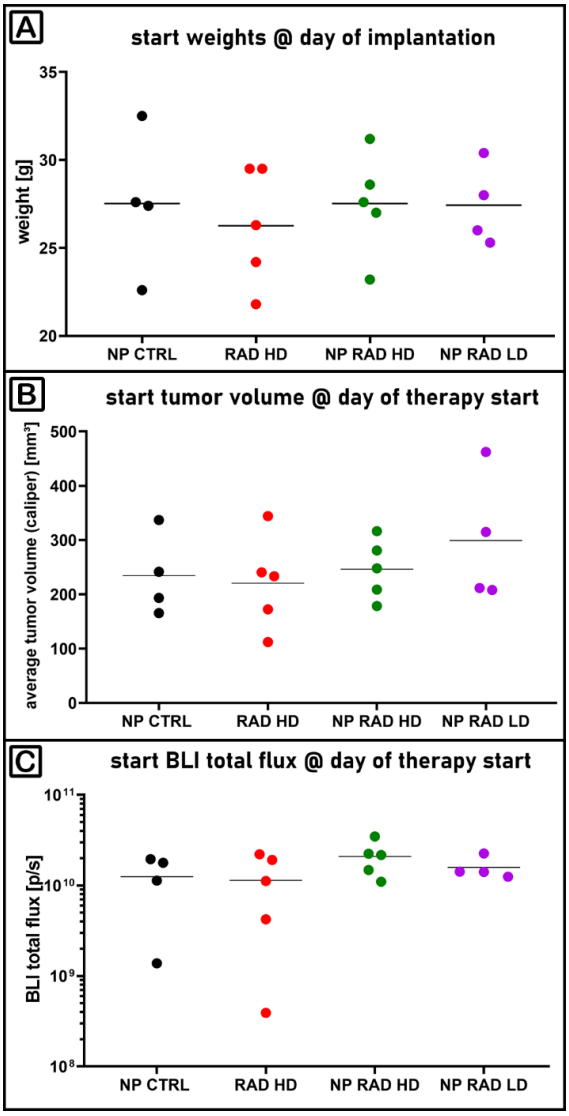

Figure 30: ***Statistical analysis of the starting condition of the radiation therapy experiment using pH8N8-BLI cells***

Comparison of A) mouse weights at the day of tumor cell implantation, B) tumor volumes at the day of therapy start and C) BLI total flux at the day of therapy start demonstrated no statistical differences between the groups ensuring unbiased starting conditions.

Comparison of the body weights in the treatment groups over time demonstrated that the weights of the NP CTRL group remained constant over the course of the experiment (until they were excluded from the experiment), while the mice in the irradiated groups showed a minor weight loss after the start of the irradiation treatments (Figure 31 A). The weight loss was about 10% and therefore not as evident as in previous experiments. It must be noted, that mice in the NP RAD LD group, which received only half of the x-ray dose suffered from a similar weight loss at the start of the RT treatment but regained some of the weight while both HD groups did not regain weight. The NP CTRL mice had to be excluded from the experiment at day 40 (after

tumor cell implantation) because the tumors reached the maximum tumor volume of 1500 mm^3. When tumor volumes measured by caliper over time relative to the therapy start were evaluated (Figure 31 B), the NP CTRL group showed a continuous tumor growth and doubled their volumes every eight days. Similar to the previous experiments, the HD irradiation protocol reduced the tumor growth significantly, as shown in Figure 31 F. The mice in the NP RAD LD group had a reduced but steady tumor growth, indicating that the lower x-ray dose was not able to stop the tumor growth. Figure 31 C shows the relative tumor volumes over time which were calculated from 3D CT data sets that were generated during RT. Therefore, no data sets were available for the NP CTRL group or for time points before the therapy start. The volume measurement was performed in a similar way to the caliper measurements by determining the length, height and width of the tumor. A segmentation-based approach was not feasible due to the poor x-ray contrast of the tumors. The CT-based tumor volumes demonstrated similar trends to the manual caliper measurements. Mice in both HD groups had unchanged tumor volumes over time, indicating that the RT can stop the tumor growth. The NP RAD LD group showed a constant but slow tumor growth. In comparison to the caliper measurements, the relative volumes of the CT measurement showed a slightly stronger tumor growth. The analysis of the mean relative BLI total flux measurements (Figure 31 D) was more difficult when compared to caliper and CT measurements. The NP CTRL group displayed an increase in the BLI total flux similar to the increase in tumor volume. Since the mice of the NP CTRL group had to be removed from the experiment before the mice of the treatment groups due to their large tumor volumes, I extrapolated the values (dotted line) using linear extrapolation. Interestingly, all three treatment groups showed an initial increase in total flux until day 5 after therapy start. Then the values decreased to levels similar to those at the therapy start. The BLI total flux measurements showed no significant differences between the three treatment groups. I observed that the tumor position with respect to the camera angle of the device significantly impacted the intensity measurements. Thus, I decided to additionally use the area of the BLI signal above 10% of the maximum value as 2D equivalent to the tumor size (Figure 31 E). While the graphs for the tumor area show the same trends as for the tumor volumes, the differences between the groups are much smaller. This can be explained by the fact that the area measurement is only two-dimensional, while the volume is three-dimensional. In comparison to the total flux measurements, the BLI tumor area values for the treated groups do not show a peak at day 5. No significant differences between the irradiated groups was observed. Finally, I evaluated the mean tumor volumes of each group at the last measurement before autopsy, as illustrated in Figure 31 F. Since the manual volume measurements are error prone, especially for small

tumors, and there were no significant differences in the tumor volumes at the therapy start, I decided to compare the absolute tumor volumes at the end of the therapy. This includes the measurement error only once, while a relative comparison would consider the error twice. The irradiated groups showed a highly significant reduction in tumor volumes in comparison to the NP CTRL group. The HD groups demonstrated a significant tumor volume reduction in comparison to the NP RAD LD group. However, no significant difference between the RAD HD and the NP RAD HD group was detected.

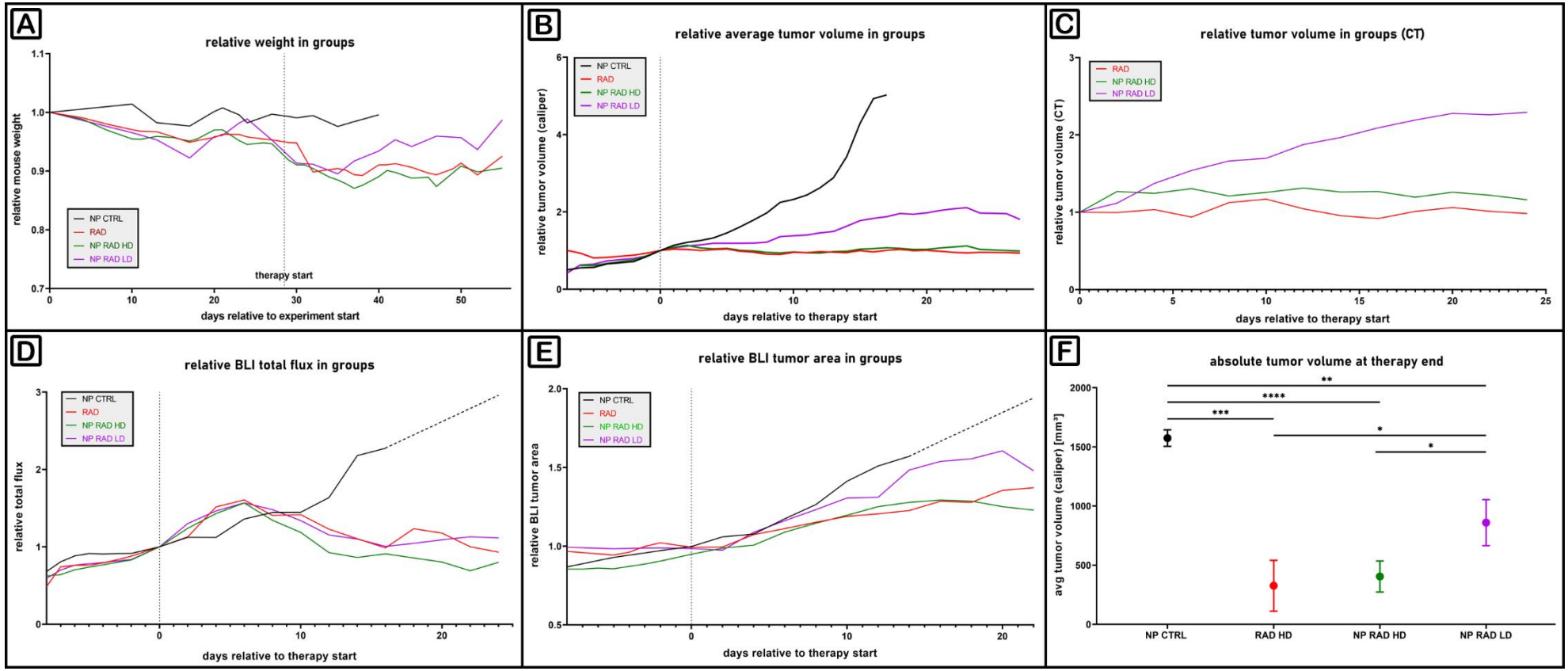

Figure 31: ***Outcome of the optimized radiation therapy using pH8N8-BLI tumors after data treatment with the proposed analysis software.***

Mean values are depicted for the following groups: NP CTRL (BaNPs, no irradiation; N=4), RAD (no BaNPs, high dose irradiation; N=5), NP RAD HD (BaNPs, high dose irradiation; N=5) and NP RAD LD (BaNPs, low dose irradiation; N=4). A) Mean weights relative to the weight at the therapy start over time for each treatment group. No significant weight loss was detected in any of the groups. B) Mean tumor volume caliper measurements over time relative to the therapy start. C) Tumor volume CT measurement over time relative to the therapy start. D) Mean BLI total flux over time relative to the therapy start. E) Mean BLI tumor area over time relative to the therapy start. F) Comparison of tumor volumes (caliper measurements) at the end of the therapy showing a significant decrease in tumor volumes in response to irradiation.

Comparisons of the manual caliper measurement with CT and BLI parameters are demonstrated in scatter plots as shown in Figure 32. A linear correlation was found between the tumor volumes measured by caliper and measured from the CT data sets ($R^2 = 0.7821$) (Figure 32 A). Figure 32 B illustrates that there is no linear correlation between the BLI total flux and the manual tumor volume measurements ($R^2 = 0.1069$). Since the trends shown in Figure 31 B and D were similar for the irradiated groups, a linear correlation was not expected. However, even for the NP CTRL group (red), which showed a similar behaviour in both graphs, no linear correlation was found. Figure 32 C demonstrates a weak linear correlation between the manual caliper measurements and the tumor areas measured by BLI ($R^2 = 0.4402$). Note that the square root of the BLI areas was compared to the cube root of the tumor volumes to account for the fact that a two-dimensional measurement was compared with a three-dimensional measurement.

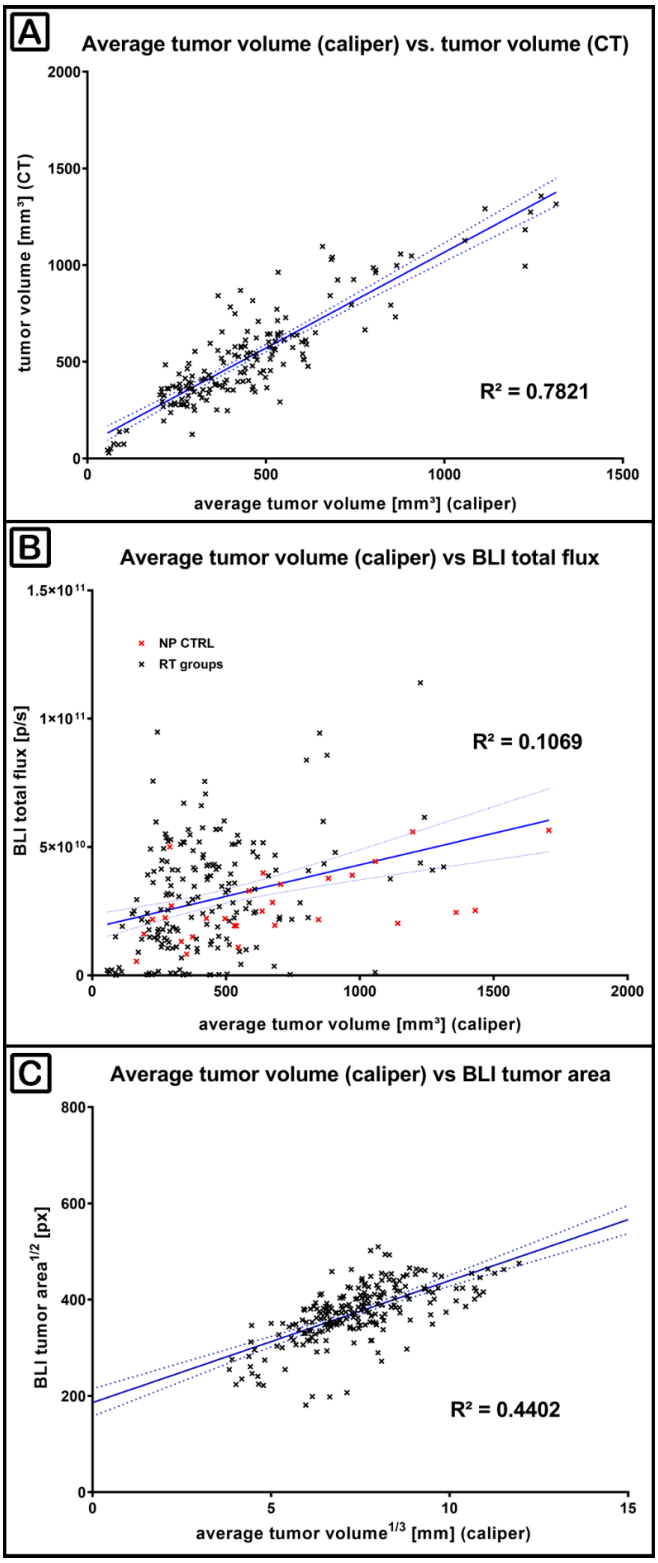

Figure 32: ***Statistical comparison of caliper tumor volume measurements with CT-based tumor volume assessment and bioluminescence readouts.***

A) Scatter plot of manual caliper tumor volume measurements with tumor volumes assessed from CT data sets, demonstrated a good correlation of both modalities (R^2=0.7821). B) Scatter plot of manual caliper tumor volume measurements with BLI total flux measurements showed no correlation of both measurement types (R^2=0.1069). C) Scatter plot of manual caliper tumor volume measurements with BLI tumor area measurements showed a weak correlation (R^2=0.4402).

In summary, RT performed by microCT can significantly impede the growth of pH8N8-BLI breast tumors. However, no significant increase in therapy efficacy was achieved with the application of BaNPs. A reduction of the x-ray dose in the NP RAD LD group resulted in a weaker therapy effect in comparison to a higher dose in the HD therapy groups. The CT based tumor volume measurements confirmed the findings of the manual caliper measurements. The implementation of an analysis software eased the identification of trends as well as the normalization of the different data sets. The additional implementation of bioluminescence measurements also revealed significant differences between the NP CTRL group and the irradiated groups, but no direct correlation between tumor volume and BLI signal was found.

4.9 Biodistribution of functionalized BaNPs after i.v. application

In the presented irradiation experiments the BaNPs were injected directly into the tumor to ensure a sufficient enrichment of BaNPs inside the tumor. Since an intratumoral injection would probably not be translatable into a patient application, another goal of this work was to analyze the accumulation of i.v. injected functionalized BaNPs in the tumor and other organs. For this purpose, the BaNPs were functionalized with an antibody against the membrane protein EpCAM and the specific binding of this construct to the pH8N8 cells was validated in vitro. To evaluate the biodistribution of systemically administered functionalized BaNPs, two tumor bearing mice were i.v. injected with 100 uL Ba120-EpCam-A594 NPs. The mice were scanned with the QuantumFX in vivo microCT directly after injection, as well as 1, 4, 7 and 24 h later. A scan protocol using 90 kV tube voltage, 200 µA tube current, a FOV of 40x40 mm^2 and a scan time of 4.5 min was utilized. No visual contrast enhancement was found in the tumor (T) at any of the scan points, as demonstrated in virtual cross sections of a mouse over time (Figure 33 A). However, the spleen (S) and liver (L) showed a strong uptake of the NPs within the first 4 h and then a stable high CT contrast until the end of the experiment. Figure 33 B shows a maximum intensity projection of the data set taken 24 h after BaNP administration, confirming the absence of x-ray contrast in the tumor region. The average gray values of each organ (measured at three different slices) are displayed in Figure 33 C as a stacked bar graph. It is evident that the contrast within the tumor remains constant over time whereas the contrast in spleen and liver increases from 0-4 h and then remains unchanged until the end of the experiment.

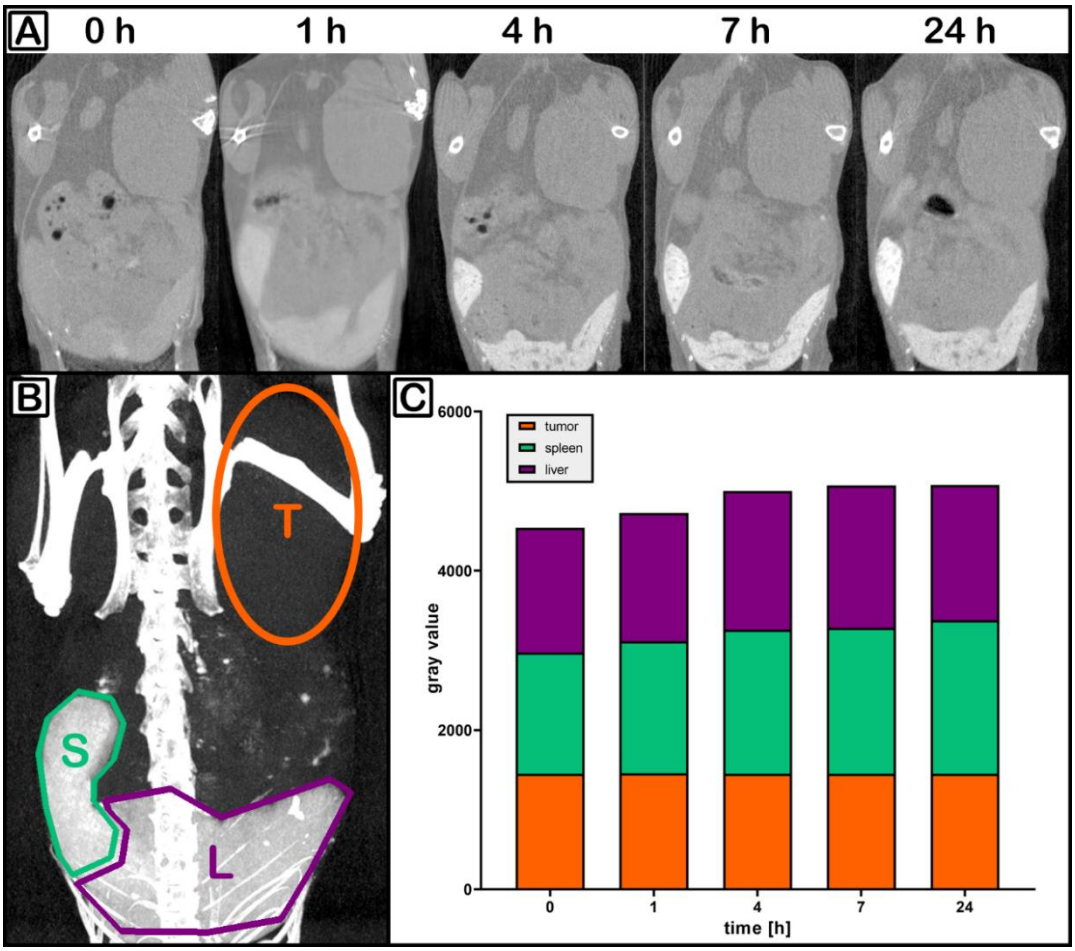

Figure 33: ***Biodistribution of functionalized BaNPs after i.v. application.***

A) CT slices of the mouse abdomen 0, 1, 4, 7 and 24 h after i.v. administration of 100 µl Ba120-EpCam-A594 show virtually no contrast enhancement in the tumor region, while the x-ray contrast in the liver and spleen is enhanced. B) Maximum intensity projection of the CT data set acquired 24 h after Ba120-EpCam-A594 administration confirms no contrast enhancement in the entire tumor (T), while Spleen (S) and liver (L) regions show drastic contrast enhancement. C) Cumulative bar chart of the measured CT gray values in the indicated regions over time. No contrast enhancement was found in the tumor.

In summary, the developed RT setup enabled to successfully shield non-targeted regions of the animals, as proven by TLD dose measurements. Intratumoral administration of BaNPs resulted in an inhomogeneous but stable enrichment of BaNPs in the tumors. All in vivo irradiation experiments showed that RT in tumor bearing mice is possible using a conventional in vivo microCT. When an optimized treatment plan was used side effects of the therapy were minimized. Despite all efforts, no evidence of an increased effect of RT in the presence of BaNPs was found. Bioluminescent tumor cells provide additional readouts for the therapy success, but the direct effect of irradiation on the bioluminescence properties of the tumor cells need to be further evaluated. The biodistribution analysis of i.v. administered functionalized BaNPs showed no accumulation of NPs in the tumor.

4.10 Validation that tumor contrast enhancement is only caused by the BaNPs

Since breast tumors are known to develop calcifications, which would cause a contrast enhancement in x-ray imaging, I needed to validate, that the contrast enhancement observed during the RT experiments was solely caused by the BaNPs. X-ray fluorescence imaging (XRF) is a method which can specifically detect and quantify the concentration and distribution of certain elements. Since barium is not present in soft tissues under natural conditions, the BaNPs were the only possible source of barium detectable in the tumors. XRF is a method in which typically a tissue section is raster scanned by a focused x-ray beam. Material is excited and responds with emitting fluorescence photons at specific wavelengths, which are detected. In combination with the known spectrum of the x-ray source, this information is element specific and can be used to produce concentration maps especially for lighter elements that are difficult to quantify by other techniques. Thus, XRF was performed in collaboration with Marius Reichardt, X-ray Physics Department, University of Goettingen, using A594 cell induced subcutaneous tumor samples intratumorally injected with BaNPs, as illustrated in Figure 34. Figure 34 A shows a 3D rendering of the in vivo CT data set of the particular tumor, demonstrating high contrast areas in the tumor. Low contrast areas are shown in gray, while high contrast areas are pseudo-colored in yellow-red. Following autopsy of the mouse, the tumor was embedded in paraffin, the surface of the paraffin block was cut until the tumor was clearly visible and scanned again by CT to provide a 3D reference for subsequent analysis. Figure 34 B shows the reconstructed CT slice which represents the surface of the cut paraffin block. The tumor margins were barely visible, due to the embedding and are outlined by the dashed line. The center of the tumor shows structures with very high contrast. Figure 34 C shows the complementary XRF scan of the surface of the paraffin block. The barium concentration in arbitrary units is shown color coded. We found high barium concentrations in XRF at the same position as the high contrast areas in the CT image, proving that the BaNPs are causing the contrast enhancement inside the tumors.

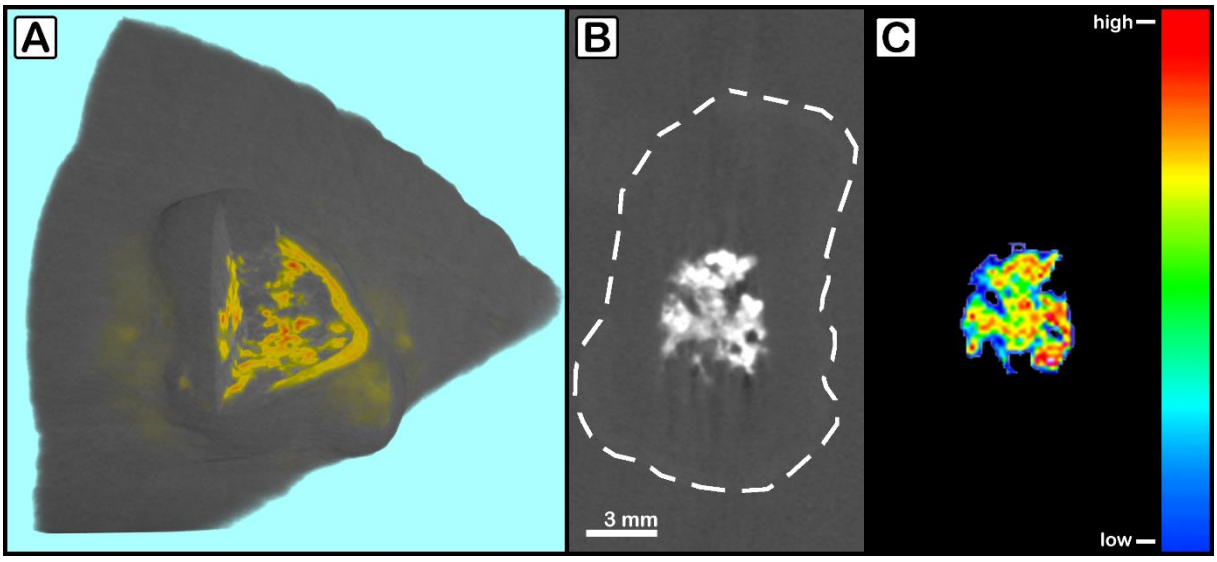

Figure 34: ***XRF measurement to validate Ba dependent x-ray contrast.***

A) 3D rendering of a subcutaneous A549 lung tumor in vivo. High contrast areas are pseudo-colored in yellow/red. B) microCT dataset of the same tumor after fixation and paraffin embedding. C) XRF map for barium of the surface of the paraffin block shown in B). XRF is pseudo-colored using a color gradient from blue (low barium concentration) to red (high barium concentration).

4.11 K-edge subtraction imaging to further improve contrast enhanced tumor imaging

The BaNPs design aimed to achieve two goals: I) Enhancement of RT and II) Improvement of tumor contrast for CT imaging. However, the systemic application of BaNPs did not show a contrast enhancement in the tumors in classical in vivo microCT. Therefore, methods that can improve the sensitivity and specificity for barium imaging are of great interest. K-edge subtraction imaging (KES) is one such method and was employed here to improve contrast enhance tumor imaging. Tumor bearing mice were intratumorally injected with BaNPs (30 µl BaNP-120), the animals were sacrificed, and the tumors explanted and embedded in paraffin blocks. The samples were scanned at the ID17 beamline at the European Synchrotron Radiation Facility (ESRF). An exemplary KES image of a BaNP injected tumor is given in Figure 35 A. Since the x-ray contrast is barium specific the tumor itself is not visible. Figure 35 B shows the segmented barium-positive area of the same image. Due to the high specificity, an automatic segmentation can be easily facilitated. Disadvantages of this approach are the need for monochromatic light, x-rays of a specific energy, which can only be produced by synchrotron light sources with reasonable x-ray flux. In addition, two acquisitions at different energies for each sample are required.

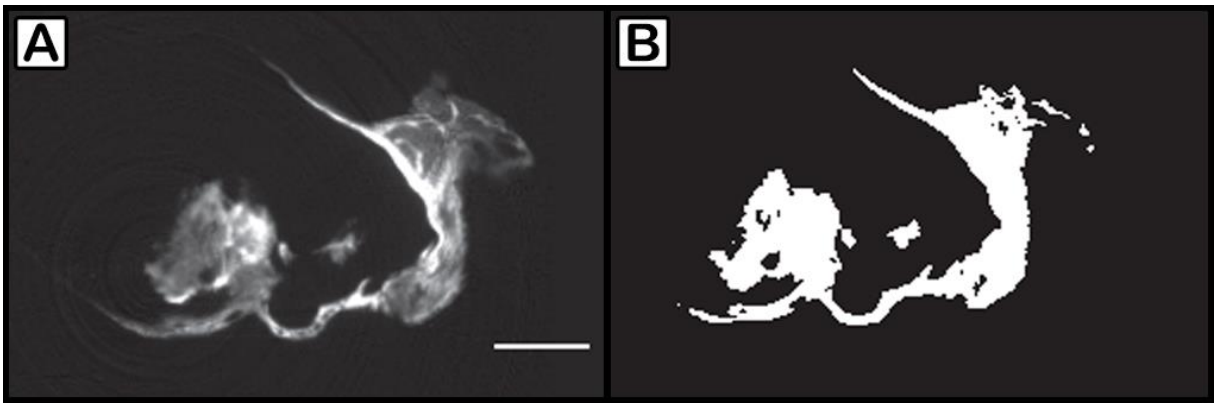

Figure 35: ***KES imaging of BaNP injected pH8N8 mouse breast tumors.***

A) SRμCT of a breast tumor that was intratumorally injected with BaNPs. B) Segmentation of Ba containing areas. The considered gray value threshold was chosen as 5σ, where σ is the standard deviation of the gray levels in the background (scale bar = 2 mm).

To circumvent these disadvantages, I followed a different route using a detector prototype (PIXIRAD Pixie-III), which allows acquiring simultaneous images at two different energy ranges, which leaves half the flux for each channel. Thus, the technique can also be used with classical x-ray tubes employed in clinical CT systems. The application of this technique on a BaNP-120 containing pH8N8 mouse breast tumor embedded in paraffin is demonstrated in Figure 36. In Figure 36 A a slice from the reconstructed low energy channel (cut off at 36.5 keV) is shown, depicting a faint contrast of the NPs (note that since the tumor tissue has not received additional staining it is invisible in the scan). Figure 36 B shows the reconstructed high-energy bin, which shows an improved contrast of the NPs. Figure 36 C shows the subtraction of the two channels. Figure 36 D-F shows 3D renderings of the data sets from A-C. Using KES only the BaNPs are visible and the contrast to noise ratio is improved.

These results were published 2020 in Physics in Medicine & Biology[112].

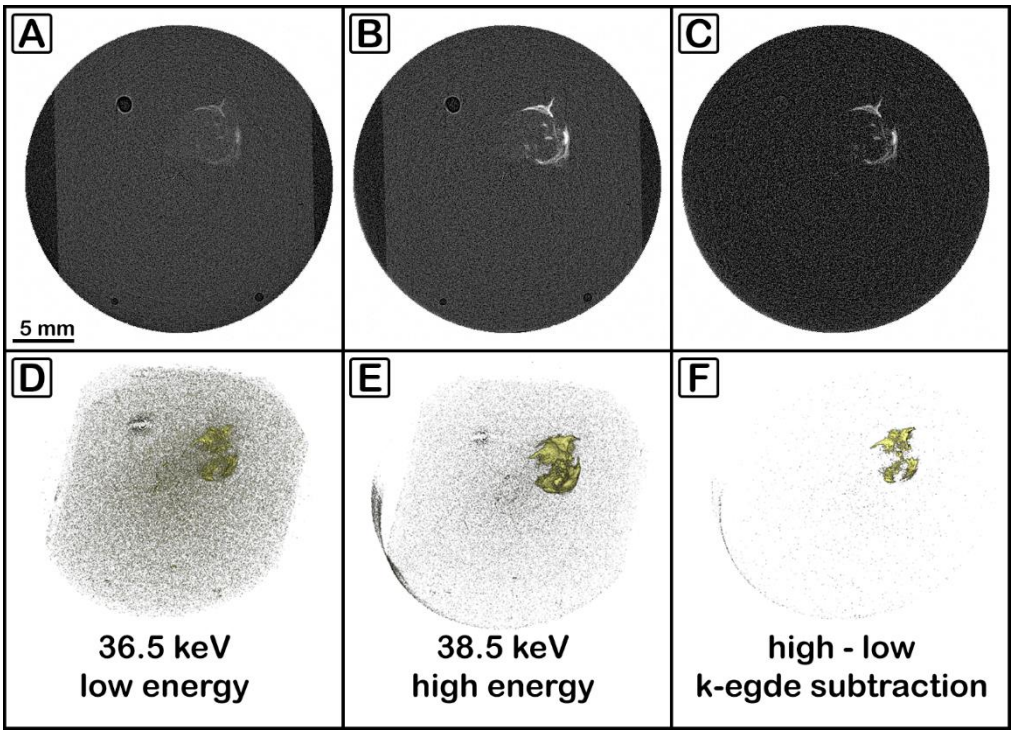

Figure 36: ***KES SRμCT for improved imaging of BaNPs.***

A) low energy CT slice (36.5 KeV). B) high energy CT slice (38.5 KeV). C) subtraction image removing the paraffin and the soft tissue. D) E) F) 3D renderings of the datasets shown in A) B) C) showing a clear improvement in the segmentation of the BaNPs.

4.12 Combined X-ray based virtual histology and classical histology to evaluate NP localization in the tumor tissue

The in vivo NP-based RT experiments showed vastly different results than those performed in vitro, with a strong BaNP dependent enhancement of RT in the cell culture but no significant difference between RT with and without NPs found in animal tests. This discrepancy between the in vitro and in vivo results suggested that the effect of the NPs is limited to tumor cells in close proximity of the BaNPs. It was therefore important to evaluate the exact BaNP location in the tumor tissue. However, we found that the NPs were not visible in classical light microscopy due to their small size of 120 nm. A histological evaluation of the NP localization in irradiated tumors was therefore difficult to achieve. On the other hand, the high CT contrast that the NPs provide, comes as a welcome aid to localize them in the tumor environment by using microCT. A further goal of my thesis was therefore the approach to combine both methods, microCT and (immuno-) histochemistry, to precisely identify the BaNPs in their local tissue environment. Previous studies of our group already established microCT imaging as a supplemental technique to histology and immunohistochemistry[92,94]. However, for the current question of localizing NPs to specific tissue structures or cells, a precise match between histology and microCT data needed to be achieved. Since histology requires sectioning of the tissue specimen it introduces deformations as demonstrated in Albers et al[94], which need to be corrected. In addition, typical soft tissue microCT acquisition enforces heavy metal based staining protocols to boost the contrast. In the context of localizing NPs such an approach would potentially obscure NP locations.

Thus, we developed an elastic registration workflow between label free phase contrast microCT imaging and histology, which was recently accepted for publication in Scientific Reports[113].

For the 3D analysis of pH8N8 breast tumors, the explanted and paraffin embedded tumors were scanned at the SYRMEP beamline of the Italian synchrotron ELETTRA using the phase contrast white beam setup. These data sets are referred to as SRµCT (synchrotron radiation microCT). Subsequently, the samples were cut with a microtome and histological staining as well as IHC was performed. To combine both modalities the developed elastic image registration workflow was used as shown in Figure 37. The workflow is embedded into a software called “Fuxlastix”, which is publicly available under https://github.com/xPITcoding/Fuxlastix. In the first step the virtual plane in the CT data set, which resembles the histological cut section needs to be found and saved as a 2D image. The histological section is recored in tiles with a microscope. These tiles are then automatically

stitched to resemble the entire tumor cross-section. The CT slice (“fixed image”), the histology image (“moving image”) as well as a script file with the general image registration settings (“Elastix parameters”) are used as input information for the software. Since the software was designed as a general tool for 2D image fusion also color images are supported as both the fixed and moving image. In that case the images are split into color channels and the calculation of the registration is based on one of the color channels but is later on applied to the color images. The calculation of the image registration is performed by an embedded tool called *elastix*. Since *elastix* has been found to be incompatible with large images, the images are downscaled by a factor of 10. After *elastix* is successfully performed, the resulting b-spline deformation grid is then upscaled to match the original resolution of the images. Finally, a second embedded tool called *transformix* is applied on each color channel separately. The resulting deformed image is shown in Figure 37 (two bottom images). The blue border (Figure 37, bottom left) indicates the degree of deformation calculated by the registration pipeline. The checkerboard view demonstrates the precision of the registration (Figure 37, bottom right).

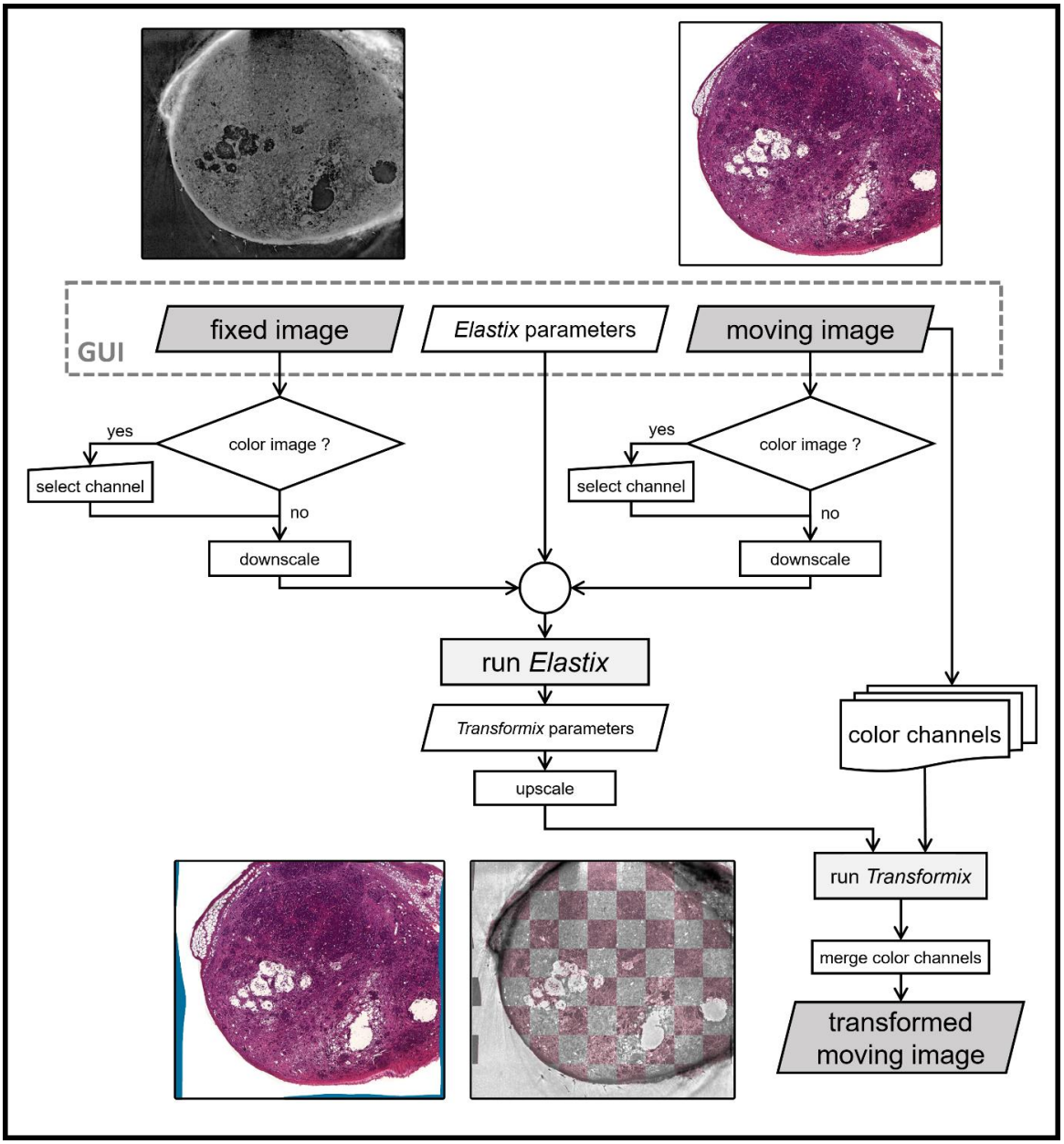

Figure 37: ***Image transformation pipeline using the Fuxlastix frontend.***

The fixed image (non-transformed CT image, top left), the moving image (histology image to be transformed, top right) and the elastix parameter file are chosen manually in the user interface (GUI) of the software. If color images are selected, the user needs to decide manually which color channel should be used for the matching process. In addition, there is a choice to select the average of the color channels as a grey value image and/or to invert the image. The images are downscaled by a factor of 10 and the elastix software is called, which outputs the transformix parameter file, which in turn is modified for the use on the original moving image. Each channel is transformed individually and subsequently merged to receive the final transformed moving image (bottom row, left image). The overlay of the fixed and the transformed overlay can be visualized using a checkerboard pattern (bottom row, right image).

In addition to the 2D overlaid images shown above the co-registration of the histology with virtual slice in SRµCT data at a known location allows to insert the histology information into the 3D context of the SRµCT data set as demonstrated in Figure 38. A 3D rendering of a SRµCT data set of an explanted and paraffin embedded pH8N8 breast tumor is shown. A registered HE stained histological image is embedded into the 3D scene at the correct location (red color). In addition, access to the quantification of 3D features - like the volumes of the vacuoles ("segmented blobs") rendered in green is now accessible. BaNP-positive areas are pseudo-colored in yellow and are easily visible in the 3D SRµCT data set. A precise co-localization of the BaNPs is described in the following chapters.

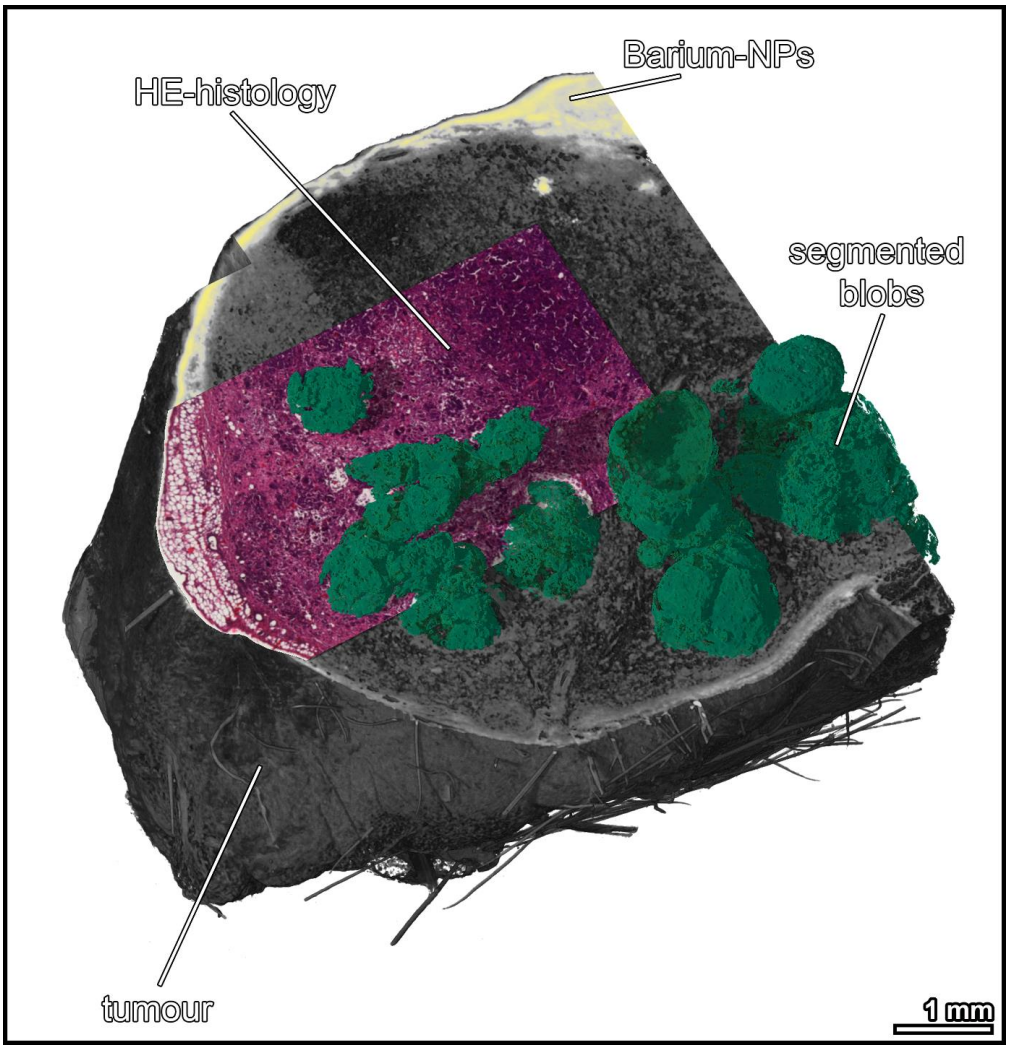

Figure 38: ***Capabilities of CT-based 3D virtual histology.***

3D rendered mouse breast tumor, virtually cut at the position of the matching HE histological section. Barium NPs are depicted in yellow. Necrotic "blobs" inside the tumor are shown in green. The "blobs" were segmented using a region growing algorithm, embedded in VG StudioMAX.

In order to validate the functionality of the image co-registration approach, different staining protocols were applied on consecutive histological sections. Since every histological slice may display different degrees of non-uniform deformation, a direct overlay provides limited information. To correct for various degrees of deformation between the different histological slices, I used an unaltered CT data set as a fixed image template. Figure 39 A shows a slice of the SRμCT data slice which was registered to the MTS histology which is shown in Figure 39 B. MTS staining was applied to depict collagen fibers in blue. Figure 39 E shows a magnification and explicitly demonstrates the continuity of the structures achieved by the registration. Specific structures like the blood vessel were identified through histology and confirmed by tracking the vessel throughout the 3D CT data set. Figure 39 C and D show specific IHC stainings for the macrophage and monocyte marker CD68 and for the SV40 T-Antigen (T-Ag), used as specific tumor marker in the WAP-T tumor mouse model, matched to their corresponding virtual slice. CD68 and T-antigen positive cells are depicted in red. Detailed views of the localization of IHC positive stained cells are visualized by a checkerboard view for the anti-CD68 IHC (Figure 39 F) and an alpha blending overlay of the segmented T-Ag positive tumor cells (Figure 39 G). These findings demonstrate that the proposed workflow was successfully applied for co-registration of SRμCT and histology/IHC data independently of the staining type. In addition, individual corrections of non-uniform deformations for every histological slice allow for effective comparison of the different staining techniques by removing the deformation-based variability between the different serial sections.

This approach enables the selective comparison of cells and structures within specific regions in the different sections, which would not be possible without the co-registration.

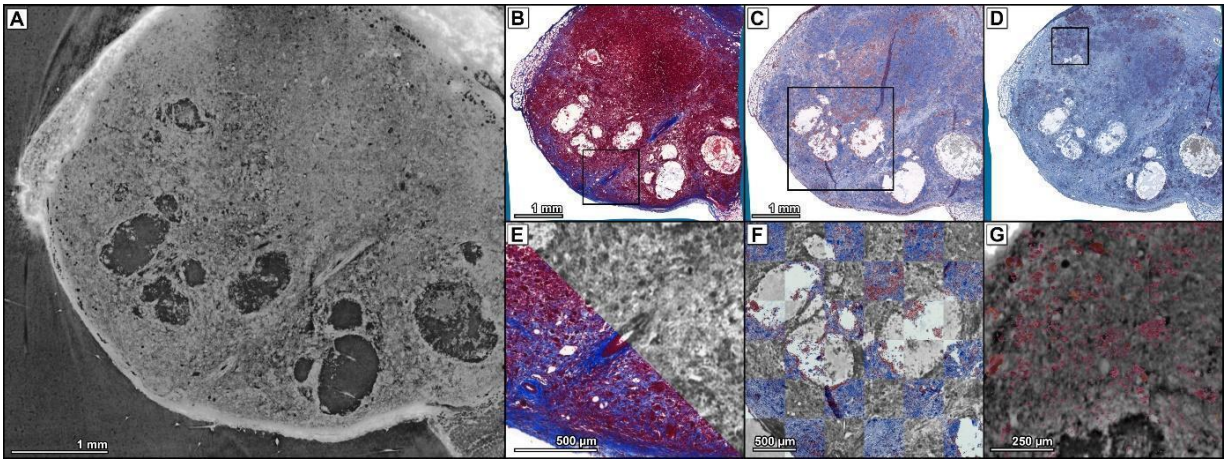

Figure 39: ***Matching of SRµCT data with different histological staining obtained from BaNPs injected mouse breast cancer tissues***

A) SRµCT virtual histology at the plane corresponding to the MTS histology shown in B. B) MTS histology. C) Anti-CD68 immunohistochemistry. D) Anti-T-Ag immunohistochemistry. E) Comparison of MTS staining with the corresponding CT slice of a magnified region as indicated by the black box in B). Gray values are inverted. F) Checkerboard comparison of anti-CD68-IHC staining with the corresponding CT slice of a magnified region as indicated by the black box in C). Gray values are inverted. G) Overlay of segmented T-Ag positive tumor cells with the corresponding CT slice of a magnified region as indicated by the black box in D).

After validating that the image registration can be successfully applied to different staining methods, I used the workflow to localize the BaNPs in their local tumor environment. In Figure 40 this process is exemplary shown for two tumors that showed an intertumoral enrichment of NPs (first row) and a concentration of the particles in the capsule (2nd row). Figure 40 A shows the SRµCT slice. The BaNPs show a strong contrast enhancement (white). Figure 40 B shows an MTS slice, corrected for deformations during the cutting process as indicated by the inhomogeneous boundary regions colored in blue. Figure 40 C shows the same histological slice with the overlaid and segmented BaNPs. The BaNPs were segmented by using a simple thresholding method using Otsu's method implemented in ImageJ. The BaNPs are shown in a yellow pseudo-color, enabling to depict the position of NPs within the tumor.

In the tumor shown here, BaNPs are concentrated in the periphery of necrotic regions, which are characterized by the lack of red staining in MTS. As indicated in the close-up image (Figure 40 D), the registration approach allows to analyses the local environment of small clusters of particles. Since the BaNPs were designed for contrast enhanced radiation therapy, I assume that the visible necrotic regions were most likely formed due to the increased local radiation damage caused by the BaNPs.

The co-registration shown in Figure 40 E depicts another example of a breast tumor where the BaNPs can be allocated only to the tumor capsule, indicating a different pattern of NP distribution after intratumoral injection. Figure 40 F illustrates the corresponding anti-CD68 stained IHC slice after the registration was performed. Furthermore, the fusion with an anti-CD68 IHC stained slice (Figure 40 G) demonstrates that the localization of the NPs coincides with regions of CD68-positive cells, indicative of macrophages that have phagocyted the BaNPs. Figure 40 H shows a magnified detail view of Figure 40 G clearly depicting a co-localization of the BaNPs and phagocytic cells.

These examples neatly demonstrate how the information achieved by classical histology can be supplemented by means of registration with high resolution CT.

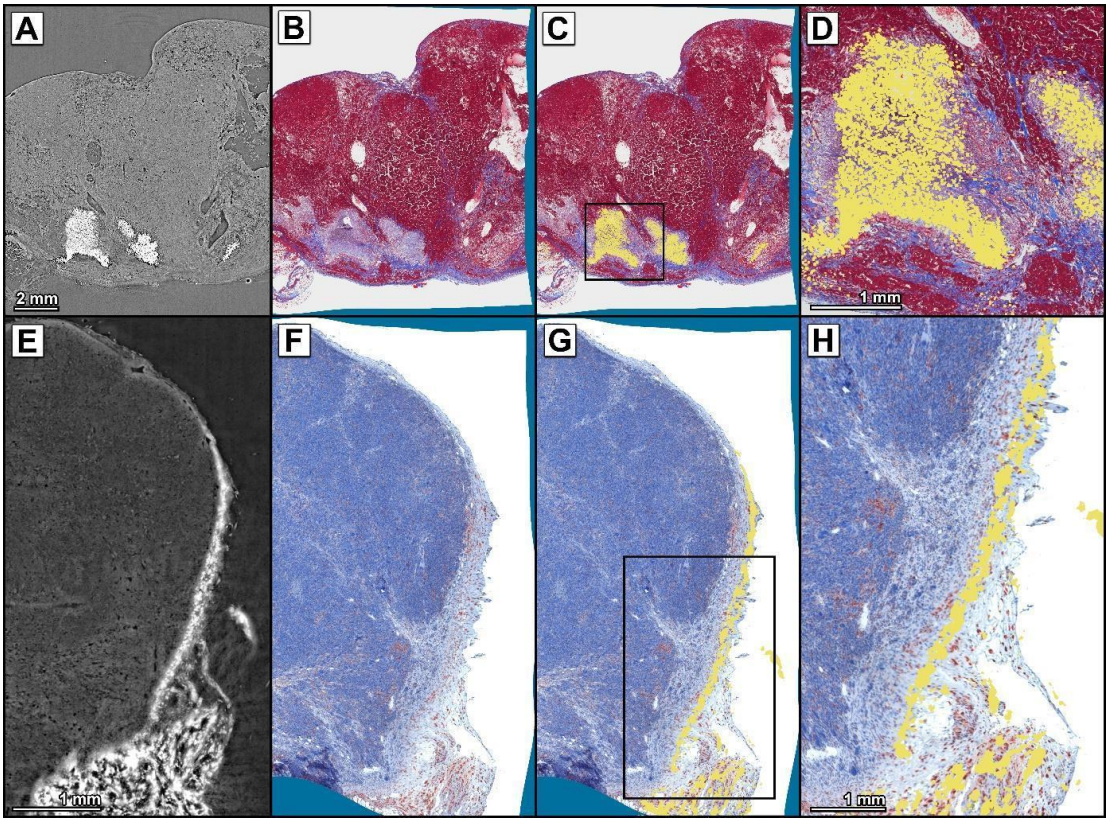

Figure 40: ***Matching of SRμCT datasets with classical histology allows precise localization of BaNPs in histological slices.***

A) SRμCT of a mouse breast tumor. Injected BaNPs can be easily localized within the tumor tissue, due to their high CT contrast. B) Registered MTS-stained histological slice of the tumor in A). Deformation is indicated by the light blue border. C) Image fusion of the MTS staining shown in B) with the segmented BaNPs from A). BaNPs were segmented using a threshold-based approach. D) Magnification of the region indicated by the black box in C). E) SRμCT slice of a second mouse breast tumor. BaNPs are localized in the tumor capsule and in the adjacent fatty tissue. F) Registered anti-CD68 IHC slice of the tumor in E). G) Image fusion of the anti-CD68 IHC image in F) with segmented BaNPs from E). BaNPS are located at the same site as CD68 positive cells indicating an uptake of the BaNPs by these phagocytic cells. H) Magnification of the region indicated by the black box in G).

In summary, I was able to place the location of the NPs into the pathological context of the local tumor environment by using the novel virtual histology workflow. Since BaNPs were found in the periphery of necrotic tumor areas, I hypothesize, that this might be an effect of the combination of BaNPs and RT. However, I could not conclusively answer the question on how far the RT effect of the BaNPs extends into the local environment.

4.13 Quantitative histological analysis of irradiated breast tumors

The analysis of tumor volumes measured in the different RT experiments demonstrated no significant differences in tumor volumes between RT with and without BaNPs. The subsequently performed histological analysis revealed strong differences in the internal structure of the tumors. Some of them contained large necrotic areas, others did not. Since necrosis is typically caused by an insufficient blood supply it can either be a consequence of a rapid tumor growth or a response to the therapy. An analysis of this effect is complicated by the fact that the degree of necrosis is volume dependent and because the necrotic area is irregular in its shape and thus difficult to assess. I therefore developed an additional software that allows to segment and quantify specifically stained regions within the histological sections of the mouse breast tumors. Figure 41 shows the workflow of the software. Stitched microscopy images of whole tumor slices are imported and downscaled. A scaling factor can be chosen individually, but a value of 0.5 was used for the images shown here. Subsequently, the background and smaller tissue structures, such as debris or disconnected parts, are removed using a modified region growing algorithm. The remaining area can then be considered as the tumor area. To segment specifically stained regions, a simple color channel threshold/range approach was used. The user selects a specific range (between 0-255) in each color channel and every pixel that fulfills these criteria is segmented. Since the necrotic areas cannot always be separated from healthy areas only based on their color, an additional homogeneity criterion is used, based on the fact that necrotic areas usually appear to be more “chaotic” and therefore less homogeneous. The software computes the standard deviation in a square of 10 by 10 pixels around the pixel of choice. A high standard deviation was used additionally to the color ranges to identify necrotic regions. For HE staining, the area of vital tumor cells and necrotic areas were segmented. For IHC, the positively strained regions were segmented. For the identification of blue stained fibers in MTS staining a different approach was chosen. The image is split into its color channels and the red channel is subtracted from the blue channel. The resulting image

mainly depicts the blue regions, while depressing red and violet regions. A separate threshold is then used on the result for simple segmentation. The software creates a labeled image with the whole tumor depicted in black and the segmented areas shown in a solid color of choice. In addition, the “tumor area”, “segmented area” and their ratio are exported for further analysis.

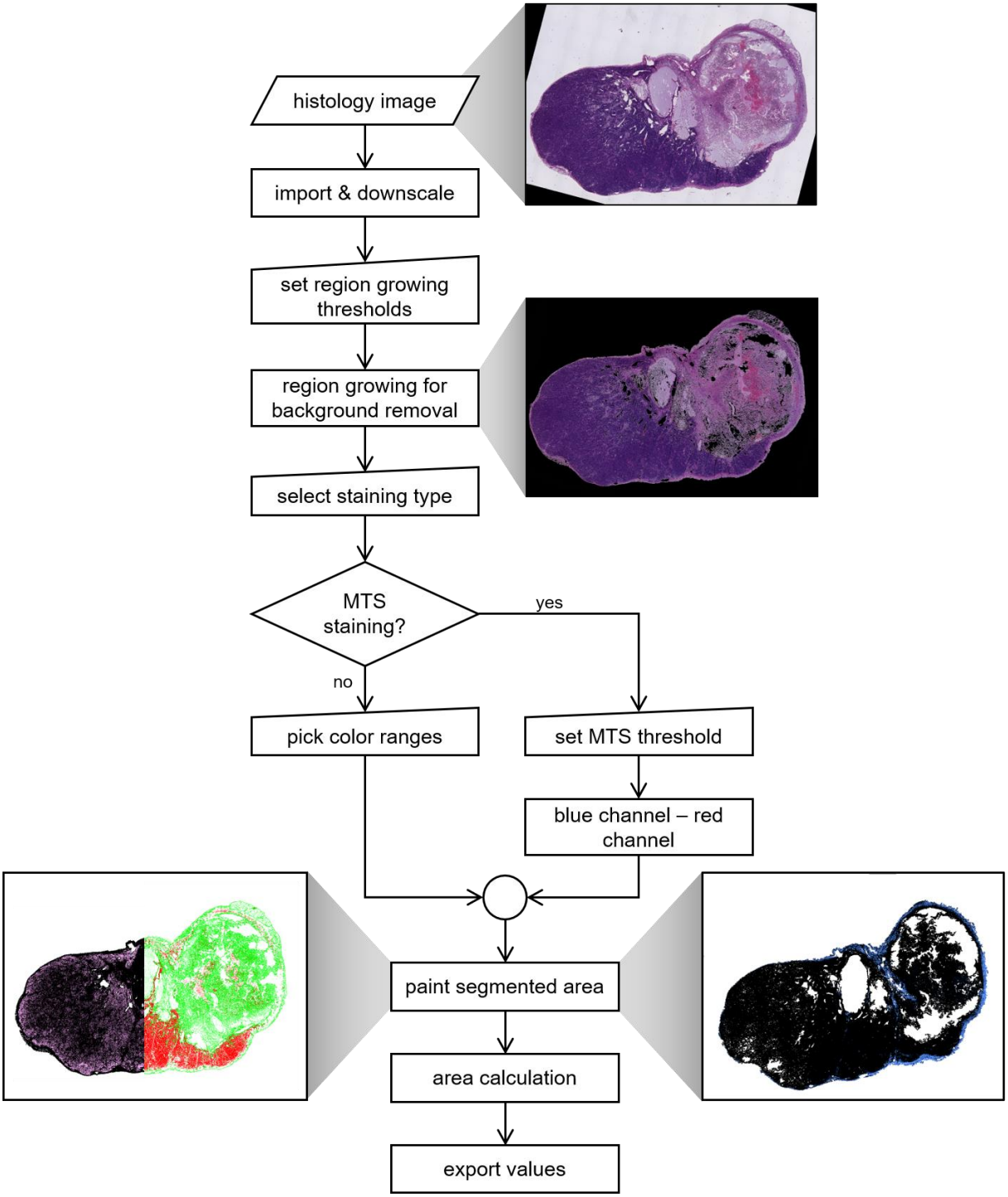

Figure 41: ***Flowchart of the histology segmentation and analysis software.***

Figure 42 shows the outcome of the software analysis for one exemplary tumor and three different stainings. A stitched microscopical image of a HE stained tumor section, which was used as input for the software is illustrated Figure 42 A. Figure 42 B demonstrates the slice after successful segmentation of the tumor area. The labeled tumor regions representing healthy tumor cells are depicted in red, while necrotic areas are shown in green (Figure 42 C). Figure 42 D-F shows the outcome for an MTS stained slice. The blue fiber regions are depicted in blue (Figure 42 F), while the tumor area is shown in black. Figure 42 G-I shows the outcome for an anti T-Ag IHC stained slice. Figure 42 I depicts the segmented IHC-positive regions in pink and the whole tumor area in black.

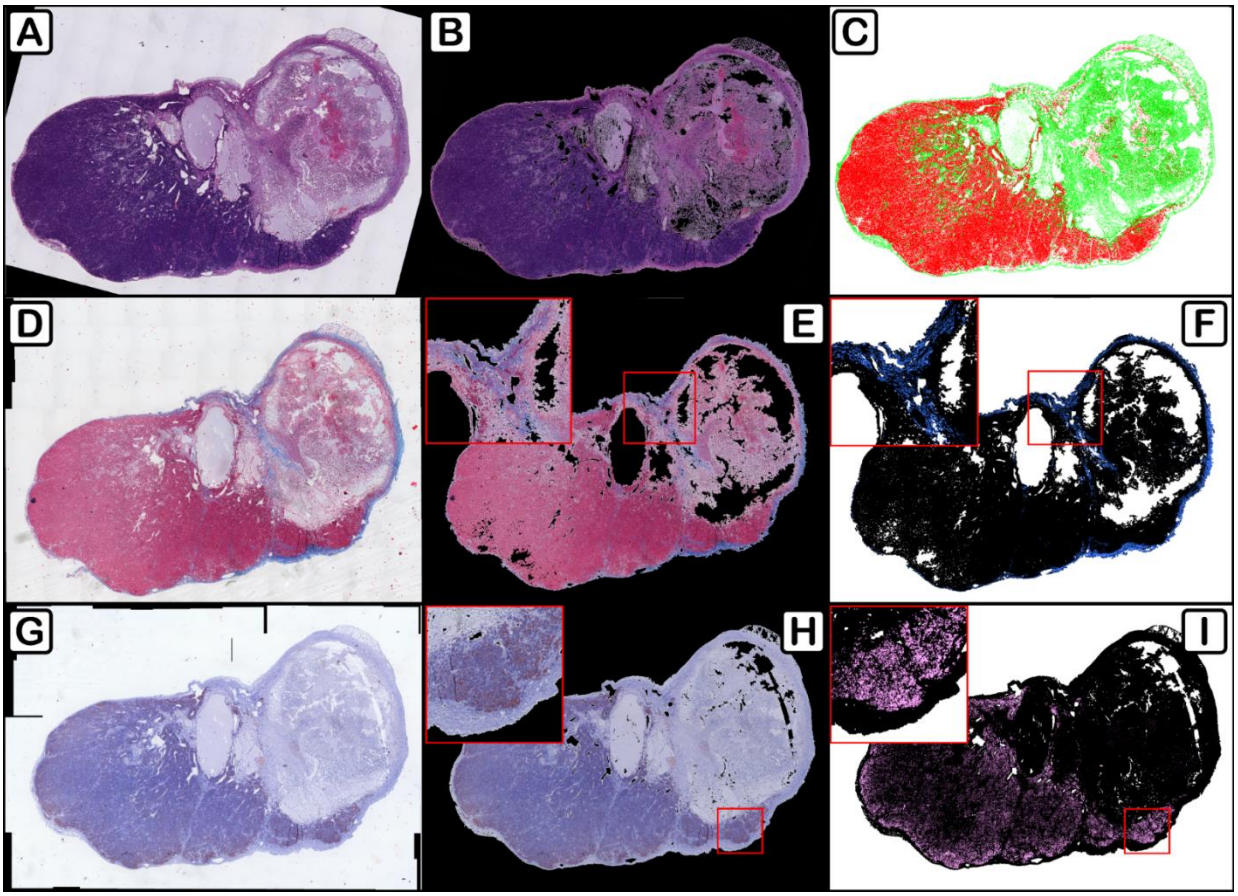

Figure 42: ***Representative images from the histology analysis software for one exemplary tumor.***

A) HE stained input image. B) Segmented tumor area of the HE stained image. C) Labeled tissue regions. Tumor cells are depicted in red, necrotic regions are shown in green. D) MTS stained input image. E) Segmented tumor area of the MTS stained image. F) Fiber regions in the MTS stained image are labeled in blue. G) Anti-T-Ag IHC input image. H) Segmented tumor area of the anti-T-Ag IHC stained image. I) T-Ag positive regions in the anti-T-Ag IHC stained image are labeled in pink. Insets are magnifications of selected red ROI boxes.

Figure 43 shows the results of the proposed histological analysis pipeline applied on pH8N8-BLI tumor sections. The segmented fiber content of the tumors relative to the area of the tumor is represented in Figure 43 A. The tumors of the NP CTRL group had a lower relative fiber content than the irradiated groups. Since the fibers are mainly located in the tumor capsule, the displayed results are rather a consequence of the different tumor sizes than the internal tumor composition. Figure 43 B shows the relative CD68 positive area in the analyzed tumor sections. On average the NP CTRL group displayed the lowest ratio of 1-2% CD68-positive area, while irradiated tumors should values up to 15% CD68-positive area. Figure 43 C shows the relative T-Ag positive area in the analyzed tumor sections. All groups show comparable values in the range of 1-8% T-Ag positive area except for one outlier in the RAD HD group (17% T-Ag positive area).

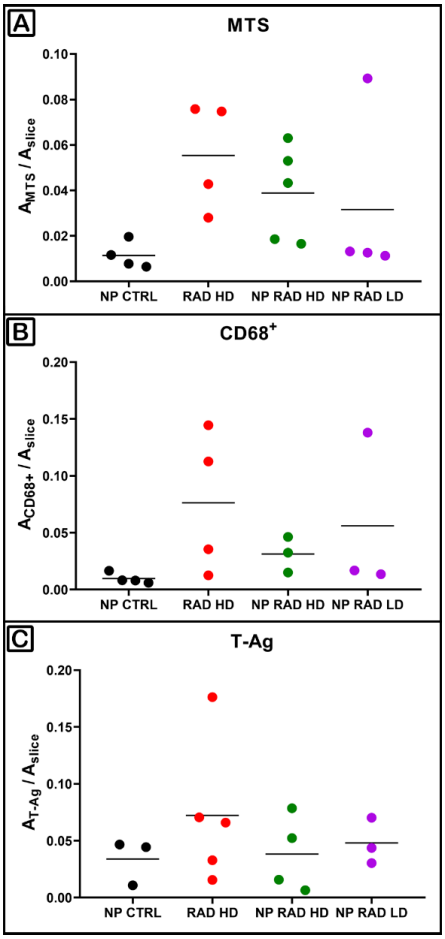

Figure 43: ***Quantitative analysis of microscopic images of whole tumor microscopical images.***

Tumor sections of pH8N8-BLI tumors were quantitatively analyzed using the proposed software. Values are depicted for the following groups: NP CTRL (BaNPs, no irradiation), RAD (no BaNPs, high dose irradiation), NP RAD HD (BaNPs, high dose irradiation) and NP RAD LD (BaNPs, low dose irradiation). A) Quantification of blue fiber content in MTS stained tumor slices. B) Quantification of CD68 positive areas in anti-CD68 IHC slices. C) Quantification of T-Ag positive area in anti-T-Ag IHC slices.

Figure 44 shows the quantification of the tumor cell and necrotic portions in the tumors. Two to three separate HE stained slices per tumor were analyzed. To be able to make a statement about the whole tumor, under the assumption that the analyzed slices were representative, the results were multiplied with the tumor volume, which was measured before tumor explantation. Therefore, Figure 44 A shows the estimated volume of living tumor cells. Both HD therapy groups show significantly lower values around 200 mm^3 in comparison to the NP CTRL group, which had volumes of 400-650 mm^3. But no difference between the RAD HD and NP RAD HD group was detected. Figure 44 B illustrates the estimated necrotic volume of the tumors. The NP CTRL group shows significantly higher amount of necrosis (500-900 mm^3) in comparison to the HD treatment groups. The HD tumors showed very small necrotic regions of less than 100 mm^3, while the LD tumors had necrotic volume of 200-400 mm^3. When both graphs are compared, it becomes apparent, that the differences are bigger in the necrotic volumes than in the volumes of living tumor cells. The hypothesis that the use of BaNPs causes an increased formation of necrotic areas was completely refuted by these results. The main cause of the formation of necrotic areas is an increased tumor volume. The irradiation therapy, with or without BaNPs, is able to keep the tumor volumes low and can therefore effectively prevent necrosis formation. Nevertheless, these findings confirm that an irradiation in an in vivo microCT is effective.

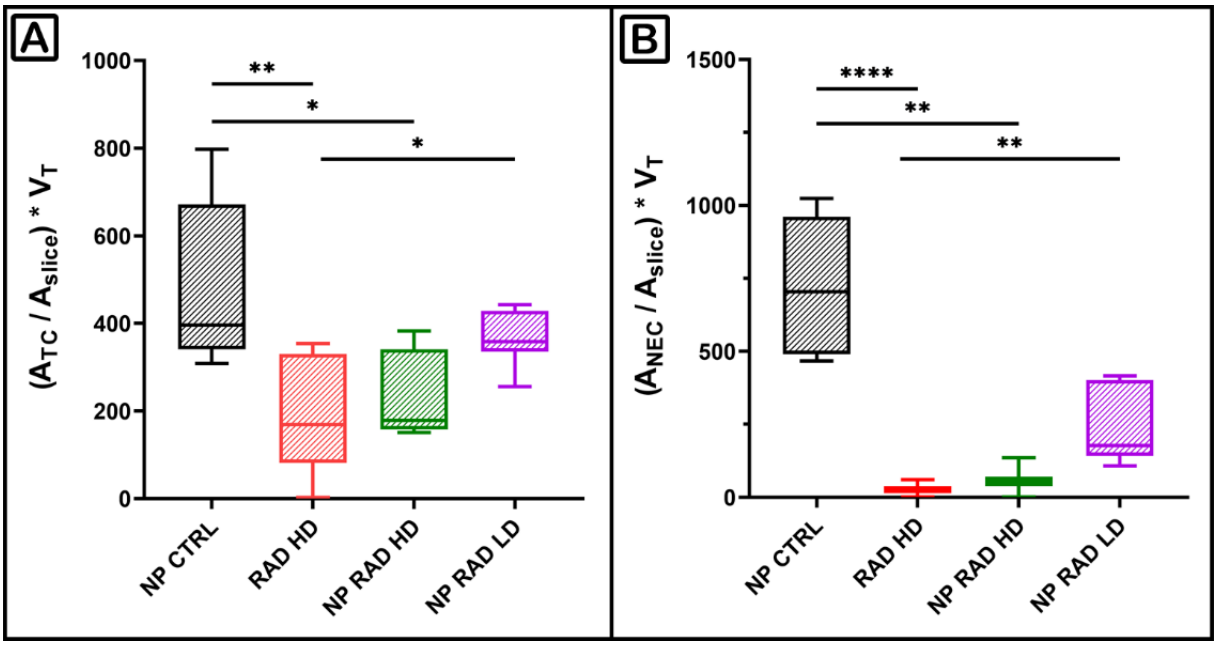

Figure 44: ***Quantification of healthy tumor cells and necrotic area on images of HE stained whole pH8N8-BLI breast tumor sections.***

HE stained tumor sections of pH8N8-BLI tumors were quantitatively analyzed using the proposed software. Values are depicted for the following groups: NP CTRL (BaNPs, no irradiation), RAD (no BaNPs, high dose irradiation), NP RAD HD (BaNPs, high dose irradiation) and NP RAD LD (BaNPs, low dose irradiation). A) Volume of living tumor cells compared for different treatment groups shows a significant decrease in the amount of living tumor cell after high dose irradiation treatment. B) Volume of necrotic regions compared for different treatment groups shows a significant reduction in necrotic regions after high dose irradiation treatment.

5 Discussion:

The aim of this thesis was to evaluate if RT in combination with BaNPs as RT enhancers can be an effective treatment option for TNBC. For this purpose, BaNPs were characterized for their toxicity and their capability to enhance irradiation effects in vitro. To provide evidence that such a therapy could be performed in patients, a proof of concept study using a preclinical mouse model for TNBC were conducted.

In the thesis presented here, I evaluated the possibilities of NP-enhanced low energy RT in a mouse model for TNBC. Characterization of BaNPs revealed that, independent of their diameter in a range from 120-220 nm, no toxic effects on the viability of cells and a high x-ray attenuation. BaNPs displayed a significant enhancement of the irradiation effect as evaluated as measured by capability of the tumor cells to form colonies by utilizing a novel analysis scheme for CFAs. Prior to in vivo RT experiments, the functionality of a self-made irradiation setup in a state-of-the-art in vivo microCT system was validated. Different x-ray dose measurements showed that the dose of 1.3 Gy per 2 min irradiation, is high enough for an efficient therapy and healthy tissue can be successfully shielded. RT experiments showed that low energy irradiation plans can successfully stop tumor growth and are well tolerated by the animals when an optimized treatment schedule, utilizing more therapy sessions with a lowered dose per session, is used. Successfully integrated BLI measurements into the RT provided additional readouts of average tumor bioluminescence intensity and projected bioluminescent tumor area. In contrast to the in vitro results, RT in tumor mouse models showed no benefit of applying BaNPs intratumorally. KES imaging as well as XRF further characterized the inhomogeneous distribution of BaNPs inside the explanted tumors. To gain more insight on the local effects of the BaNPs, I developed a new multimodal analysis approach, which combines high resolution SRµCT with classical histology, enabling a precise co-localization the BaNPs in their local tumor environment. In addition, CD68-positive cells accumulate in close proximity of BaNPs. Histological analysis showed that necrosis inside the breast tumors is a size dependent effect, and not related to the presence of BaNPs.

5.1 Design and characterization of BaNPs as radiation therapy enhancers

The suitability of the newly designed BaNPs for in vivo application was proven by cell viability assays, as no toxic effects on pH8N8 breast cancer cells, 3T3 fibroblasts and MH-S macrophages were observed in vitro. In addition, the BaNPs are characterized by a strong x-ray attenuation as evaluated by microCT analysis and by the ability to enhance the reduced low energy x-ray irradiation effect on pH8N8 murine breast cancer cells as well as human A549 lung cancer cells to form colonies in vitro. The NPs, which were designed to be used in this study had two purposes. On one hand they should improve tumor detection and imaging and on the other hand they should function as a radiation therapy (RT) enhancer. To function as a contrast agent, the physical properties of the NPs had to be compatible with standard CT devices. In addition, (pre-) clinical contrast agents must not be toxic and should not accumulate in non-targeted tissues or organs. Excretion of the contrast agent also must be considered. The BaNPs used in my work exhibited a good CT contrast both in vitro as well as in vivo after intra tumoral application. This was expected as barium-sulphate is commonly used for radiographic examinations of the gastrointestinal tract and therefore its enhancement of x-ray contrast is well known[114,115]. In addition, BaNP containing contrast agents are commonly used in preclinical experiments[116,117]. To enhance RT effects, the NPs must absorb more radiation than the surrounding tissue itself and convert the radiation locally into secondary effects that damage the targeted tumor cells. Based on these requirements NPs with a barium core and hydrodynamic diameters between 120-300 nm were designed to be evaluated in this thesis. The BaNPs were coated with a polymer to reduce toxicity and to enable functionalization with antibodies. This was confirmed as, BaNPs did not have any significant negative on cell viability as measured by WST-assays and therefore are suited for an in vivo application. However, to my knowledge Barium containing NPs have not been tested as RT enhancers in preclinical applications previously. Other NP core elements than barium, have been proposed for radio enhancement. Gold NPs[72,118], gadolinium NPs[119], hafnium NPs[120] or iron oxide NPs[121] displayed an enhancement effect of radiation treatment. The BaNPs used in this work showed a significant enhancement effect, since they did successfully inhibit the formation of colonies after in vitro irradiation.

5.2 Concept of using a CT for radiation therapy

Low energy irradiation treatment with an in vivo microCT in breast cancer bearing mice resulted in tumor regression and significantly reduced tumor growth in comparison to untreated controls. The use of a preclinical in vivo microCT allowed the combination of tumor staging and volume measurement with the actual treatment. Upon optimizing the treatment plan to mimic the strategy which is used for breast cancer patients[30], the side effects of the therapy, assessed by weight measurements of the animals, were reduced drastically in comparison to RT using a higher dose per session. This included the use of more irradiation sessions with a reduction in the single doses from 5.5 to 2.7 Gy per treatment and effective shielding of healthy regions of the mice. The fact that irradiation efficiently reduced tumor volumes, proved that the concept of RT in a CT device can be applied in a mouse model for TNBC.

The concept of low energy RT in a CT device is not used in the clinic, since low energy irradiation will result in high dose deposition in healthy tissue, especially close to the surface of the patient. Standard RT, which has been used for the treatment of cancer for many decades[122], uses energies in the MeV range, which are generated by LINACs. In this energy range, the x-ray absorption of the tissue is low and therefore skin and other healthy tissue located in the radiation path experience no or only minor damage. To reach a sufficient dose deposition within the tumor area, this region is irradiated from different angles resulting in overlapping radiation fields within the tumor (stereotactic RT)[34,35]. For this approach, a precise knowledge of the tumor margins is needed, which is usually provided by a preceding CT or MRI scan[123,124]. The repositioning of the patient from the diagnostic device to the LINAC can change the position of the tumor with respect to its detected location. Moreover, access to LINACs is still much more limited than to CT systems. In addition, RT is an unspecific treatment which is solely based on the assumption that radiation damage is more efficient in tumor cells than in normal cells, due to their impaired DNA repair mechanism[125]. Here I demonstrated successfully that low energy RT in breast cancer bearing mice is feasible. X-ray doses of 2.7 Gy per treatment were able to reverse the growth of pH8N8 breast tumors once the therapy effect took place. Therefore, a combined imaging and therapy approach in an in vivo microCT can be performed. However, based on the results of the here presented preclinical work using mice, the question if CT-based RT would be applicable in humans in the future, cannot be answered and needs further experiments. The main reason for limiting the radiation dose in patients (also for diagnostic purposes) is to minimize the prevalence of so-called stochastic effects, which describe the increase in cancer risk in the rest of the lifespan of the

patient[126]. Since the average mouse life span is about two years and the experiments were terminated weeks after RT onset, stochastic effects could not be evaluated.

Therefore CT-based RT for a patient application needs to be modified to decrease the dose related side effects, including an increased cancer risk. One concept to achieve this goal, would be to locally enhance the dose effect, while simultaneously lowering the overall radiation dose. So-called RT enhancers were proposed for this purpose[127]. The concept of RT enhancers entails the increase of the dose deposition in the tumor and/or the generation of a secondary effect that leads to additional damage of the tumor cells. To achieve these characteristics, all enhancers contain strongly absorbing elements such as barium, which was used in this study. However, in the energy range that is used for clinical RT, these materials are essentially transparent. Thus, low energy RT in the range of keV has been proposed[39–41], which provides better absorption of the enhancers, but at the same time leads to negative effects on the healthy tissue surrounding the tumor. Low energy RT itself is not a new concept and is used for intra-operative irradiation in the clinical practice[128]. If successful therapy concepts, combining RT enhancers with low energy irradiation, were to be developed, treatment and diagnostic scan could be performed in the same CT device. Due to the large availability of CT devices such an RT could be performed in any radiological practice and would immensely increase the capacities of RT. The basis for the translation of such a novel technique is the evidence that specific enhancers lead to substantially increased radio therapy efficiency, allowing the application of lower dose levels - a prerequisite for sparing the healthy tissue from negative radiation effects as is the case for conventional RT.

5.3 Comparison of in vitro and in vivo effectiveness of BaNPs as radio therapy enhancers

The in vitro assessment of different BaNPs as radio enhancers and CT contrast agents revealed no toxic effect of the NPs but a strong increase in radiation damage, especially when irradiation was combined with BaNP-120, which were therefore chosen for the in-vivo studies. However, in all performed in-vivo studies with orthotopically implanted pH8N8 breast cancer cells and subcutaneously implanted A549 lung cancer cells, BaNP-120 failed to significantly reduce tumor volumes RT when compared to low energy RT without NPs.

BaNPs which were added to the tumor cells prior to in vitro irradiation effectively enhanced the irradiation effect on the ability to from colonies. In this setting, the cells were irradiated in

micro reaction tubes, instead after plating them into cell culture well plates, to create an almost spherical shape, which was supposed to mimic the situation in a tumor in vivo. Therefore, in contrast to the in vivo situation, the BaNPs were in a direct vicinity to the cells. For the in vivo RT experiments the BaNPs were directly injected into the tumor to ensure that the BaNP concentration was as high as possible. While this approach hardly represents a clinical therapy approach, it is commonly used in preclinical experiments[129,130]. Even though I tried to improve the distribution of BaNPs inside the tumor, the CT data sets, which were acquired during the RT sessions, reveal a stable but inhomogeneous distribution of the BaNPs inside the tumors. It can be speculated that this is a major factor why BaNPs did not successfully improve the treatment effect in comparison with irradiated control mice, which did not receive any BaNPs. In contrast, several groups have shown an increased RT effect of different NPs in tumor studies using mice. The first proof of concept using NPs as RT enhancers was demonstrated by Hainfeld et al. who used gold nanoparticles (AuNPs) activated by 250 keV x-rays[131]. They used tumors from subcutaneously implanted EMT-6 breast cancer cells. 1.9 nm sized AuNPs were intravenously injected and mice were irradiated once with a dose of 30 Gy. They found a one-year survival of 86% for mice treated with gold and irradiation versus 20% with x-rays alone and 0% with gold alone. An approach which was more comparable to the work of this thesis was presented by Wang et al., who used intratumorally applied barium tungstate nanoparticles ($BaWO_4$)[129]. Due of the presence of tungsten, which is another heavy metal ion, the demonstrated effect cannot be solely based on barium. The authors used subcutaneously implanted 4T1 breast cancer cells in combination with an intra tumoral application of 50 µl PVP-$BaWO_4$. While the NPs could not stop the tumor growth entirely, the combination of the NPs with a single 10 Gy irradiation significantly reduced the tumor growth in comparison with control mice which only received a PBS injection. CT-guided radiotherapy using AuNPs to enhance both CT image contrast and radiation effects in a tumor was studied by Al Zaki et al.[132]. The authors applied retroorbital injected gold-loaded polymeric micelles, which showed a significant increase for tumor CT contrast in comparison to the clinical contrast agent Aurovist, while significantly increasing the survival fraction after irradiation with 6 Gy at 175 kVp in comparison with animals that did not receive any nanoparticles.

In the here presented study the survival of the treated mice was not analyzed, because tumors were explanted and further examined. The therapy outcome was evaluated by comparing the changes in tumor volumes. Since the pH8N8 tumors showed a fibrous capsule formation, and various degrees of intra tumoral necrosis in treated and untreated mice, the tumor volume might not have been an optimal criterion to evaluate therapy success. Bioluminescent tumor cells in

combination with multiple ex-vivo analysis approaches did not reveal any positive effects of using BaNPs. While non-irradiated mice showed the expected correlation between the tumor volume and the BLI signal[133], treated animals showed after an initial increase in the BLI intensity a decrease of the BLI signal, which did not correlate with simultaneously performed caliper-based tumor volume measurements. For the luciferase catalyzed reaction intracellular oxygen as well as adenosine triphosphate (ATP) are needed[134]. Since irradiation produces ROS inside the tumor cells there might be a direct interference of irradiation with the light reaction of the bioluminescent cells[135]. Therefore, my results indicate that BLI does not generate a reliable readout in combination with RT.

In summary, despite all efforts to optimize the in vivo RT to enhance the effect of the BaNPs, no significant improvement of the therapy outcome was found, and the promising results of the in vitro experiments could not be replicated. The main differences between both studies were the BaNP concentration and distribution with respect to the tumor cells.

5.4 Physical principles of NP enhanced radiation therapy

To understand potential reasons why the RT enhancement effect of the BaNPs did not translate from a successful in vitro application into a preclinical setting using an orthotopical breast cancer model for TNBC, it is necessary to understand the physical limitations of the concept of using RT enhancers. Irradiation damage in cells is caused by multiple secondary effects. High energy photon radiation causes enhanced oxidative stress, direct DNA damage and interferes with the cell cycle[63]. The idea of using heavy metal NPs is too amplify these biological effects by the local emission of electrons. There are different physical mechanisms for electron emission. Low energy irradiation (keV range) mainly produces electrons via the so-called photoelectric effect, in which an electron is removed from the electron shell of an atom, due to the energy transfer of an incident photon. Auger electrons are produced by the filling of an inner-shell vacancy of an atom, which is accompanied by the emission of an electron[68,136–138]. High energy irradiation (MeV range), as produced by medical LINACs, mainly causes the so-called Compton effect as well as electron pair production[139]. Therefore, maximization of electron production is the essential property of RT enhancers. The k-edge is the energy level where the strongest bound electron in the k-shell of the atom is emitted. At this energy the probability of x-ray absorption is very high. The k-edge and therefore the x-ray attenuation maximum of barium is at 37.4 keV, which resembles the average of the x-ray energy used in (pre-)clinical CT systems. Had this been the only criterion for a successful therapy, barium

would have been an ideal choice to be used as a RT enhancer in combination with a CT. However, next to the probability of electron emission the travelling distance of the electron is important to maximize biological effects. The kinetic energy of the electron determines its possible travelling distance and equals the energy of the incident x-ray photon minus the binding energy of the electron. Kuncic and Lacombe state an average travelling distance of the photoelectron in water of 200 µm for a kinetic energy of ~120 keV or 9 µm for a kinetic energy of ~20 keV[64]. In my case the average photon energy emitted by the microCT was around 40-45 keV, leaving only 3-8 keV of kinetic energy for the photoelectron. Therefore, the probability of photoelectron emission was very high, but the emitted electrons had a very limited travelling distance. As a consequence, the different results of in vitro and in vivo experiments are plausible. Due to the combination of inhomogeneous distribution and limited effective range of the BaNPs the tumors could not be treated optimally. However, a sufficient increase in photon energy would reduce the x-ray attenuation of the BaNPs and therefore their contrast, which would interfere with the intended bimodality of the BaNPs. In addition, (pre-) clinical CT systems cannot produce high energy irradiation. In summary, this discussion shows that finding a good RT enhancer is a complex problem that depends on multiple factors.

5.5 Tumor targeting and biodistribution of NPs

To guarantee a maximum accumulation of NPs in the tumor as part of the first efficacy evaluation process, intra tumoral administration of the particles was performed to minimize the possibility that RT fails due to a lack of NPs in the tumor. MicroCT data sets revealed a certain accumulation of BaNPs in the tumor, the distribution of the NPs was very inhomogeneous and remained localized at the injection sites of the tumors. This lack of homogenous NP distribution may at least in part be an explanation for the unsuccessful increase in RT efficiency of the NPs. It also must be pointed out that an intra tumoral application would limit the clinical use of the NPs to superficial tumor entities such as skin cancer. A systemic administration, as is possible by i.v. injection, would therefore be more clinically relevant.

A common method for increased targeting of i.v. injected NPs to the tumor is the functionalization with antibodies directed to tumor specific antigens. Fluorescent labeled EpCAM antibodies were found to bind to pH8N8 tumor cells as well as pH8N8 breast tumors as demonstrated by confocal microscopy. EpCAM is a membrane protein that is frequently overexpressed in breast tumors[140]. In contrast, no accumulation of EpCAM-antibody labeled BaNP-120 in the breast tumors was detected after i.v. administration measured by microCT

analysis. However, i.v. administered EpCAM-antibody labeled BaNP-120 strongly increased the x-ray contrast in liver and spleen. Targeting NPs to the tumor site has been a long endeavor of research by exploring different routes of administration and labeling NPs with tumor antigen-specific antibodies[141]. However, most NP-based therapeutic strategies have either not made it into the clinic or have failed to significantly improve patient outcome[142,143]. This is most likely due to the inter-and intra-individual heterogeneity of tumors and to the complexity of tumor and immune response that has been underestimated. For instance, the Enhanced Permeability and Retention (EPR) effect, was widely believed to be a general and homogenous feature of most tumors, a phenomenon caused by leaky vessels by which NPs would predominantly accumulate in the tumor. It has now been recognized that the EPR effect is greatly influenced by a number of parameters, including the tumor microenvironment, vessel density and permeability and stroma composition[144,145]. A sufficient accumulation of NPs in the tumor after i.v. administration assumes a sufficient blood supply of the tumor and even then, typically only 5% of the administered NPs reach the tumor site[75]. A possible reason could have been that the tumors in this study were insufficiently vascularized and that the antibody labeled NPs remained only in the vessels surrounding the tumor without reaching the inner part of the tumor. As reported in many other studies which used i.v. administered of NPs[146–148], I detected a strong accumulation of the NPs in the liver and in the spleen. Within the timeframe of the experiment (24 h) no decay of NP derived x-ray contrast was detected in these organs. These findings are in agreement with other publications stating enhanced liver contrast even months after NP administration[149]. It has been shown by others, that NPs are taken up by macrophages and other phagocytic cells in liver and spleen[150–152]. While a liver or spleen accumulation of NPs is not problematic in preclinical research, due to the short lifespan of mice and because the animals are sacrificed after the experiments. Regarding a clinical translation, this aspect of NP-based therapies should be considered. A possibility for reliable elimination of NPs from the body is the generation of biodegradable particles. While the barium sulphate in the core of the used NPs is very inert, free barium ions act as a muscle poison, causing gastrointestinal, cardiac and skeletomuscular stimulation followed by paralysis[153]. Therefore, for BaNPs, degradability would not be a good approach as it might generate toxic debris. Thus, the NPs need to be inert and stable and will therefore most likely never leave the liver and spleen, which is supported by the fact that we never saw a reduction in the tumor contrast during the time span of our experiments. While an application of the current Ba120 NPs as RT enhancers seems unlikely in patients, the absence of any toxic effects and the strong contrast registered in CT, suggest that the Ba120 NPs could present an interesting contrast agent for preclinical CT studies.

5.6 Ex vivo analysis of BaNPs in their local tumor environment

The fact that in vitro irradiation showed an increase in the irradiation effect in the presence of BaNPs, while intratumorally applied BaNPs did not improve the RT outcome, hints at a small effective radius of the BaNPs. This hypothesis is supported by the fact that the travelling distance emitted photo electrons is very short. Since the BaNPs were not detectable in classical light microscopy[154], a novel co-registration tool for microCT and histology was developed to analyze the BaNPs in their local tumor environment. BaNPs were found to be inhomogeneously distributed and colocalized with CD68-positive phagocytic cells.

For a precise co-localization of the BaNPs visualized by high resolution microCT and the corresponding local tumor environment, depicted in histological sections, a simple overlay of images from both modalities proved to be insufficient. This work among others revealed non-uniform deformation occur during the cutting and staining of the histological slices[155–157]. Therefore, a novel workflow, which used elastic registration to perform image fusion of both modalities was developed. This software has already been applied for multiple other fusion purposes, such as overlapping electron microscopy and histology, subsequently performed histology with different stainings and CT and macroscopic imaging. As co-registration of images from multiple modalities is increasingly important to allow for multiparametric characterization of tissue and cell types, this tool is now available to be used in many more projects in the future.

By utilizing this image registration tool, BaNPs were frequently found in the tumor capsule. This in combination with their limited effective radius, probably prevented a significant RT enhancement effect on the tumor cells themselves. In addition, BaNPs co-localized with tumor areas with an increased occurrence of macrophages and other phagocytic cells, as indicated by a CD68 positive IHC. This leads to the hypothesis of an increased macrophage infiltration into the tumors and their capsule. Therefore, the macrophages might have “shielded” the tumor from the therapy enhancement effect of the BaNPs. This hypothesis is supported by reports from the literature. Chiang et al. found an increase in $CD68^+$ tumor associated macrophages (TAMs) in hypoxic regions of subcutaneously expressed murine astrocytoma after irradiation. Seifert et al. also state an increased TAM infiltration caused by RT[158].

Quantitative histological evaluation of whole tumor histological stainings revealed that the degree of necrosis is dependent on the tumor volume, rather than on the presence of BaNPs, as no difference in necrotic areas was found between irradiated tumors and irradiated tumors, which received BaNPs. This correlation was already reported in the literature before and can

be explained by the fact that the volume increase of the tumor is faster than the subsequent vascularization[159,160]. The application of RT slowed down or stopped the tumor volume increase and therefore prevented the formation of necrosis.

5.7 Alternative strategies for using NPs to enhance RT effects

The BaNPs used in this thesis were not able to efficiently reduce tumor growth kinetics in comparison to tumors which received only irradiation. The BaNPs were designed to locally enhance the x-ray dose effect in the tumors, by converting the incident low energy x-rays into photo electron emission. While this concept was confirmed to be beneficial in increasing irradiation effects on tumor cells in vitro, these findings were not translatable into tumor mouse models. Novel approaches using NPs and RT try to not only use the immediate physical properties of heavy metal NPs but use them to activate secondary (bio-)chemical effects to improve therapy outcome. One way to achieve this is to use NPs to decrease the radio resistance of the tumors[161]. The epidermal growth factor receptor (EGFR), which is commonly upregulated in TNBC[162], would be an optimal target for this purpose, since EGFR upregulation is connected to increased radio resistance[163]. First in vitro studies using NP encapsulated oligo nucleotides have been performed[164], which showed that these NPs were successful in downregulating EGFR expression. The idea of using NPs as carriers for drugs or small molecules is also a reoccurring theme in cancer research[49]. This concept relies on the fact, that the NPs accumulate in the tumor tissue due to functionalization and the EPR effect and can therefore release their active components in close vicinity to the targeted tumor[165]. In addition NPs which are locally "activated" by the biological properties of the tumor such as pH are evaluated[166]. These concepts are also pursued in combination with RT because the incident irradiation can be used as an activator of secondary effects. Zhang et al. used barium peroxide (BaO_2) NPs which are modified with a glutamic acid tetrasodium salt on their surface to decrease cytotoxic effects under physiological conditions[130]. In tumor regions, the hydroxyl radicals generated by irradiation will break the chemical structure of the surface coating and therefore release the barium ions, which then act as cytotoxins. The authors report a significant reduction in tumor volume when RT and BaO_2 NPs are combined in a 4T1 tumor xenograft model. Intra tumoral hypoxia is a key factor for radio resistance of cancer cells[167,168]. Another concept called thermoradiotherapy uses NPs to create local hyperthermia in the tumor and therefore leads to enhanced vascular perfusion and consequent reduced hypoxia[169]. AuNPs were proposed to be used for thermoradiotherapy[170]. Self and Thompson propose a concept which

includes antibodies that can be activated by light[171]. While visible light or UV-light has a limited penetration depth in biological tissues x-rays can easily penetrate soft tissue. Therefore, the use of NPs which can convert x-ray into lower energetic light could solve this issue and could locally activated i.v. administered antibodies or compounds at the tumor site.

6 Conclusion

In the presented thesis, I confirmed that low energy RT can successfully reduce tumor growth in a mouse model for TNBC. BaNPs enhanced the effect of irradiation on tumor cells in vitro but did not however improve the radiotherapeutic effect on tumor growth in vivo. Future studies aim at evaluating if BaNPs can be used to enhance classical high energy RT using linear accelerators. To achieve the proposed concept of NP enhanced RT using a CT system, the NPs should be redesigned to activate secondary effects.

7 Bibliography

1. Roser, M. & Ritchie, H. Cancer. *Our World Data* (2015).
2. Becker, S. A historic and scientific review of breast cancer: The next global healthcare challenge. *Int. J. Gynecol. Obstet.* **131**, S36–S39 (2015).
3. Murawa, P., Murawa, D., Adamczyk, B. & Połom, K. Breast cancer: Actual methods of treatment and future trends. *Rep. Pract. Oncol. Radiother.* **19**, 165–172 (2014).
4. Dall, G. V. & Britt, K. L. Estrogen Effects on the Mammary Gland in Early and Late Life and Breast Cancer Risk. *Front. Oncol.* **7**, (2017).
5. Mørch, L. S. *et al.* Contemporary Hormonal Contraception and the Risk of Breast Cancer. *N. Engl. J. Med.* **377**, 2228–2239 (2017).
6. White, N. D. Hormonal Contraception and Breast Cancer Risk. *Am. J. Lifestyle Med.* **12**, 224–226 (2018).
7. Global cancer statistics 2018: GLOBOCAN estimates of incidence and mortality worldwide for 36 cancers in 185 countries - Bray - 2018 - CA: A Cancer Journal for Clinicians - Wiley Online Library. https://acsjournals.onlinelibrary.wiley.com/doi/full/10.3322/caac.21492.
8. Elston, C. W. & Ellis, I. O. Pathological prognostic factors in breast cancer. I. The value of histological grade in breast cancer: experience from a large study with long-term follow-up. *Histopathology* **19**, 403–410 (1991).
9. Harmer, M., Denoix, P. & Hamperl, H. Das TNM-System zur Klassifikation von Tumorkrankheiten. *Klin. Wochenschr.* **46**, 1181–1185 (1968).
10. Prat, A. & Perou, C. M. Deconstructing the molecular portraits of breast cancer. *Mol. Oncol.* **5**, 5–23 (2011).
11. Corben, A. D. Pathology of Invasive Breast Disease. *Surg. Clin. North Am.* **93**, 363–392 (2013).
12. Bland, K. I., Copeland, E. M., Klimberg, V. S. & Gradishar, W. J. *The Breast: Comprehensive Management of Benign and Malignant Diseases*. (Elsevier Inc, 2017). doi:10.1016/C2014-0-01946-6.
13. Piccart-Gebhart, M. J. *et al.* Trastuzumab after Adjuvant Chemotherapy in HER2-Positive Breast Cancer. *N. Engl. J. Med.* **353**, 1659–1672 (2005).
14. Breast cancer pathogenesis and histologic vs. molecular subtypes | McMaster Pathophysiology Review. http://www.pathophys.org/breast-cancer/breastcancer-copy/.
15. Denkert, C., Liedtke, C., Tutt, A. & von Minckwitz, G. Molecular alterations in triple-negative breast cancer-the road to new treatment strategies. *Lancet Lond. Engl.* **389**, 2430–2442 (2017).
16. Li, X. *et al.* Triple-negative breast cancer has worse overall survival and cause-specific survival than non-triple-negative breast cancer. *Breast Cancer Res. Treat.* **161**, 279–287 (2017).
17. Foulkes, W. D., Smith, I. E. & Reis-Filho, J. S. Triple-negative breast cancer. *N. Engl. J. Med.* **363**, 1938–1948 (2010).
18. Waks, A. G. & Winer, E. P. Breast Cancer Treatment: A Review. *JAMA* **321**, 288–300 (2019).
19. Schneeweiss, A. *et al.* Diagnosis and Therapy of Triple-Negative Breast Cancer (TNBC) – Recommendations for Daily Routine Practice. *Geburtshilfe Frauenheilkd.* **79**, 605–617 (2019).

20. Arbeitsgemeinschaft der Wissenschaftlichen Medizinischen Fachgesellschaften e.V. (AWMF) , der Deutschen Krebsgesellschaft e.V. (DKG) und der Deutschen Krebshilfe. S3-Leitlinie Mammakarzinom. *Leitlinienprogramm Onkol.* 469 (2020).

21. Yao, Y., Chu, Y., Xu, B., Hu, Q. & Song, Q. Radiotherapy after surgery has significant survival benefits for patients with triple-negative breast cancer. *Cancer Med.* **8**, 554–563 (2019).

22. Schopper, D. & de Wolf, C. How effective are breast cancer screening programmes by mammography? Review of the current evidence. *Eur. J. Cancer* **45**, 1916–1923 (2009).

23. O'Connell, A. *et al.* Cone-Beam CT for Breast Imaging: Radiation Dose, Breast Coverage, and Image Quality. *Am. J. Roentgenol.* **195**, 496–509 (2010).

24. Lindfors, K. K. *et al.* Dedicated Breast CT: Initial Clinical Experience1. *Radiology* **246**, 725–733 (2008).

25. Brennan, S., Liberman, L., Dershaw, D. D. & Morris, E. Breast MRI Screening of Women With a Personal History of Breast Cancer. *Am. J. Roentgenol.* **195**, 510–516 (2010).

26. Heywang-Köbrunner, S. H. *et al.* International investigation of breast MRI: results of a multicentre study (11 sites) concerning diagnostic parameters for contrast-enhanced MRI based on 519 histopathologically correlated lesions. *Eur. Radiol.* **11**, 531–546 (2001).

27. O'Connell, A. M., Karellas, A. & Vedantham, S. The Potential Role of Dedicated 3D Breast CT as a Diagnostic Tool: Review and Early Clinical Examples. *Breast J.* **20**, 592–605 (2014).

28. Wienbeck, S., Fischer, U., Luftner-Nagel, S., Lotz, J. & Uhlig, J. Contrast-enhanced cone-beam breast-CT (CBBCT): clinical performance compared to mammography and MRI. *Eur. Radiol.* **28**, 3731–3741 (2018).

29. Harris, J. R., Lippman, M. E., Osborne, C. K. & Morrow, M. *Diseases of the Breast*. (Lippincott Williams & Wilkins, 2012).

30. National Comprehensive Cancer Network. NCCN Guidelines for breast cancer therapy. *NCCN* https://www.nccn.org/login?ReturnURL=https://www.nccn.org/professionals/physician_gls/pdf/breast.pdf.

31. Gillette, E. L. & Gillette, S. M. Principles of radiation therapy. *Semin. Vet. Med. Surg. (Small Anim.)* **10**, 129–134 (1995).

32. Baskar, R., Lee, K. A., Yeo, R. & Yeoh, K.-W. Cancer and Radiation Therapy: Current Advances and Future Directions. *Int. J. Med. Sci.* **9**, 193–199 (2012).

33. Farkona, S., Diamandis, E. P. & Blasutig, I. M. Cancer immunotherapy: the beginning of the end of cancer? *BMC Med.* **14**, 73 (2016).

34. Lambrecht, M., Nevens, D. & Nuyts, S. Intensity-modulated radiotherapy vs. parotid-sparing 3D conformal radiotherapy: Effect on outcome and toxicity in locally advanced head and neck cancer. *Strahlenther. Onkol.* **189**, 223–229 (2013).

35. Leong, T. *et al.* 3D Conformal radiotherapy for gastric cancer—results of a comparative planning study. *Radiother. Oncol.* **74**, 301–306 (2005).

36. Davis, A. T., Palmer, A. L. & Nisbet, A. Can CT scan protocols used for radiotherapy treatment planning be adjusted to optimize image quality and patient dose? A systematic review. *Br. J. Radiol.* **90**,.

37. Wang, J., Wang, H. & Qian, H. Biological effects of radiation on cancer cells. *Mil. Med. Res.* **5**, (2018).

38. Anschel, D. J., Bravin, A. & Romanelli, P. Microbeam radiosurgery using synchrotron-generated submillimetric beams: a new tool for the treatment of brain disorders. *Neurosurg. Rev.* **34**, 133–142 (2011).

39. Peter Bernhardt, Eva Forssell-Arons. Low-energy Electron Emitters for Targeted Radiotherapy of Small Tumours. *Acta Oncol.* **40**, 602–608 (2001).

40. Buonanno, F. *et al.* Rotational radiotherapy of breast cancer with polyenergetic kilovoltage X-ray beams: An experimental and Monte Carlo phantom study. *Phys. Med.* **62**, 63–72 (2019).

41. Di Lillo, F. *et al.* Synchrotron radiation external beam rotational radiotherapy of breast cancer: proof of principle. *J. Synchrotron Radiat.* **25**, 857–868 (2018).

42. Valentin, J. Relative biological effectiveness (RBE), quality factor (Q), and radiation weighting factor (wR): ICRP Publication 92: Approved by the Commission in January 2003. *Ann. ICRP* **33**, 1–121 (2003).

43. Vande Velde, G. *et al.* Longitudinal in vivo microcomputed tomography of mouse lungs: No evidence for radiotoxicity. *Am. J. Physiol.-Lung Cell. Mol. Physiol.* **309**, L271–L279 (2015).

44. McKeever, S. W. S., Moscovitch, M. & Townsend, P. D. Thermoluminescence dosimetry materials: properties and uses. (1995).

45. Willemink, M. J. & Noël, P. B. The evolution of image reconstruction for CT—from filtered back projection to artificial intelligence. *Eur. Radiol.* **29**, 2185–2195 (2019).

46. Vert, M. *et al.* Terminology for biorelated polymers and applications (IUPAC Recommendations 2012). *Pure Appl. Chem.* **84**, 377–410 (2012).

47. Pelaz, B. *et al.* Diverse Applications of Nanomedicine. *ACS Nano* **11**, 2313–2381 (2017).

48. Gao, W., Hu, C.-M. J., Fang, R. H. & Zhang, L. Liposome-like Nanostructures for Drug Delivery. *J. Mater. Chem. B Mater. Biol. Med.* **1**, (2013).

49. Patra, J. K. *et al.* Nano based drug delivery systems: recent developments and future prospects. *J. Nanobiotechnology* **16**, 71 (2018).

50. Nune, S. K. *et al.* Nanoparticles for biomedical imaging. *Expert Opin. Drug Deliv.* **6**, 1175–1194 (2009).

51. Ramos-Gomes, F. *et al.* Single- and two-photon imaging of human micrometastases and disseminated tumour cells with conjugates of nanobodies and quantum dots. *Sci. Rep.* **8**, 4595 (2018).

52. Bruchez, M., Moronne, M., Gin, P., Weiss, S. & Alivisatos, A. P. Semiconductor nanocrystals as fluorescent biological labels. *Science* **281**, 2013–2016 (1998).

53. Popovtzer, R. *et al.* Targeted gold nanoparticles enable molecular CT imaging of cancer. *Nano Lett.* **8**, 4593–4596 (2008).

54. Kim, D., Park, S., Lee, J. H., Jeong, Y. Y. & Jon, S. Antibiofouling polymer-coated gold nanoparticles as a contrast agent for in vivo X-ray computed tomography imaging. *J. Am. Chem. Soc.* **129**, 7661–7665 (2007).

55. Galperin, A. *et al.* Radiopaque iodinated polymeric nanoparticles for X-ray imaging applications. *Biomaterials* **28**, 4461–4468 (2007).

56. Larsson, E. *et al.* Dual-modal CT and MRI functional and anatomical imaging using barium sulphate and gadolinium nanoparticle loaded macrophages in a preclinical asthma mouse model. (2015).

57. Sardar, R., Funston, A. M., Mulvaney, P. & Murray, R. W. Gold Nanoparticles: Past, Present, and Future†. https://pubs.acs.org/doi/pdf/10.1021/la9019475 (2009) doi:10.1021/la9019475.

58. Nealon, G. L. *et al.* Liquid-crystalline nanoparticles: Hybrid design and mesophase structures. *Beilstein J. Org. Chem.* **8**, 349–370 (2012).

59. Chaudhuri, R. G. & Paria, S. Core/Shell Nanoparticles: Classes, Properties, Synthesis Mechanisms, Characterization, and Applications. https://pubs.acs.org/doi/pdf/10.1021/cr100449n (2011) doi:10.1021/cr100449n.

60. Ngoune, R., Peters, A., von Elverfeldt, D., Winkler, K. & Pütz, G. Accumulating nanoparticles by EPR: A route of no return. *J. Controlled Release* **238**, 58–70 (2016).

61. Bogdanov, A. A., Weissleder, R. & Brady, T. J. Long-circulating blood pool imaging agents. *Adv. Drug Deliv. Rev.* **16**, 335–348 (1995).

62. Jannasch, K. *et al.* Detection of different tumor growth kinetics in single transgenic mice with oncogene-induced mammary carcinomas by flat-panel volume computed tomography. *Int. J. Cancer* **125**, 62–70 (2009).

63. Choi, J., Kim, G., Cho, S. B. & Im, H.-J. Radiosensitizing high-Z metal nanoparticles for enhanced radiotherapy of glioblastoma multiforme. *J. Nanobiotechnology* **18**, 122 (2020).

64. Kuncic, Z. & Lacombe, S. Nanoparticle radio-enhancement: principles, progress and application to cancer treatment. *Phys. Med. Biol.* **63**, 02TR01 (2018).

65. Liu, Y. *et al.* Metal-based NanoEnhancers for Future Radiotherapy: Radiosensitizing and Synergistic Effects on Tumor Cells. *Theranostics* **8**, 1824–1849 (2018).

66. *Nanotechnology-Based Precision Tools for the Detection and Treatment of Cancer*. (Springer International Publishing, 2015). doi:10.1007/978-3-319-16555-4.

67. Ku, A., Facca, V. J., Cai, Z. & Reilly, R. M. Auger electrons for cancer therapy – a review. *EJNMMI Radiopharm. Chem.* **4**, 27 (2019).

68. Yokoya, A. & Ito, T. Photon-induced Auger effect in biological systems: a review. *Int. J. Radiat. Biol.* **93**, 743–756 (2017).

69. Chang, M.-Y. *et al.* Increased apoptotic potential and dose-enhancing effect of gold nanoparticles in combination with single-dose clinical electron beams on tumor-bearing mice. *Cancer Sci.* **99**, 1479–1484 (2008).

70. Coulter, J. A. *et al.* Cell type-dependent uptake, localization, and cytotoxicity of 1.9 nm gold nanoparticles. *Int. J. Nanomedicine* **7**, 2673–2685 (2012).

71. Zhang, X.-D. *et al.* Size-dependent radiosensitization of PEG-coated gold nanoparticles for cancer radiation therapy. *Biomaterials* **33**, 6408–6419 (2012).

72. Chen, Y., Yang, J., Fu, S. & Wu, J. Gold Nanoparticles as Radiosensitizers in Cancer Radiotherapy. *Int. J. Nanomedicine* **15**, 9407–9430 (2020).

73. Duan, X., Wang, J., Yu, L., Leng, S. & McCollough, C. H. CT scanner x-ray spectrum estimation from transmission measurements. *Med. Phys.* **38**, 993–997 (2011).

74. National Institute of Standards and Technology. https://physics.nist.gov/cgi-bin/XrayTrans/search.pl?download=column&element=All&trans=Kedge&lower=8000&upper=200000&units=eV.

75. Bae, Y. H. & Park, K. Targeted drug delivery to tumors: Myths, reality and possibility. *J. Controlled Release* **153**, 198–205 (2011).

76. Medina, D. The mammary gland: a unique organ for the study of development and tumorigenesis. *J. Mammary Gland Biol. Neoplasia* **1**, 5–19 (1996).

77. Cardiff, R. D. & Wellings, S. R. The Comparative Pathology of Human and Mouse Mammary Glands. *J. Mammary Gland Biol. Neoplasia* **4**, 105–122 (1999).

78. McNally, S. & Stein, T. Overview of Mammary Gland Development: A Comparison of Mouse and Human. *Methods Mol. Biol. Clifton NJ* **1501**, 1–17 (2017).

79. Schulze-Garg, C., Löhler, J., Gocht, A. & Deppert, W. A transgenic mouse model for the ductal carcinoma in situ (DCIS) of the mammary gland. *Oncogene* **19**, 1028–1037 (2000).

80. Maenz, C. *et al.* Epithelial-mesenchymal plasticity is a decisive feature for the metastatic outgrowth of disseminated WAP-T mouse mammary carcinoma cells. *BMC Cancer* **15**, 178 (2015).

81. Wegwitz, F. *et al.* Tumorigenic WAP-T mouse mammary carcinoma cells: a model for a self-reproducing homeostatic cancer cell system. *PloS One* **5**, e12103 (2010).

82. Otto, B. *et al.* Low-grade and high-grade mammary carcinomas in WAP-T transgenic mice are independent entities distinguished by Met expression. *Int. J. Cancer* **132**, 1300–1310 (2013).

83. Wegwitz, F. Entdeckung, Charakterisierung und Modulation des Tumorstammzellsystems im WAP-T Mammakarzinom-Mausmodell. *Discovery, characterization and modulation of the tumor stem cell system in the WAP-T mammary carcinoma mouse model* (2010).

84. Albers, J. *et al.* X-ray-Based 3D Virtual Histology—Adding the Next Dimension to Histological Analysis. *Mol. Imaging Biol.* **20**, 732–741 (2018).

85. Dullin, C. *et al.* μCT of ex-vivo stained mouse hearts and embryos enables a precise match between 3D virtual histology, classical histology and immunochemistry. *PLoS ONE* **12**, (2017).

86. Missbach-Guentner, J. *et al.* 3D virtual histology of murine kidneys –high resolution visualization of pathological alterations by micro computed tomography. *Sci. Rep.* **8**, 1407 (2018).

87. Kommoss, F. K. *et al.* Three-dimensional virtual histology of benign and malignant endometrial stromal neoplasms: a new perspective on why morphology matters. *Int. J. Gynecol. Cancer* ijgc–2020–002313 (2021) doi:10.1136/ijgc-2020-002313.

88. Metscher, B. D. MicroCT for comparative morphology: simple staining methods allow high-contrast 3D imaging of diverse non-mineralized animal tissues. *BMC Physiol.* **9**, 11 (2009).

89. Metscher, B. D. MicroCT for developmental biology: A versatile tool for high-contrast 3D imaging at histological resolutions. *Dev. Dyn.* **238**, 632–640 (2009).

90. Metscher, B. A simple nuclear contrast staining method for microCT-based 3D histology using lead(II) acetate. *J. Anat.* **n/a**,.

91. Busse, M. *et al.* Three-dimensional virtual histology enabled through cytoplasm-specific X-ray stain for microscopic and nanoscopic computed tomography. *Proc. Natl. Acad. Sci.* **115**, 2293–2298 (2018).

92. Saccomano, M. *et al.* Synchrotron inline phase contrast μCT enables detailed virtual histology of embedded soft-tissue samples with and without staining. *J. Synchrotron Radiat.* **25**, 1153–1161 (2018).

93. Dullin, C. *et al.* MÖNCH detector enables fast and low-dose free-propagation phase-contrast computed tomography of in situ mouse lungs. *J. Synchrotron Radiat.* **25**, 565–569 (2018).

94. Albers, J., Markus, M. A., Alves, F. & Dullin, C. X-ray based virtual histology allows guided sectioning of heavy ion stained murine lungs for histological analysis. *Sci. Rep.* **8**, 7712 (2018).

95. Cooper, D. M. L. *et al.* Three dimensional mapping of strontium in bone by dual energy K-edge subtraction imaging. *Phys. Med. Biol.* **57**, 5777–5786 (2012).

96. Panahifar, A. *et al.* Three-dimensional labeling of newly formed bone using synchrotron radiation barium K-edge subtraction imaging. *Phys Med Biol* 13 (2016).

97. Bayat, S. *et al.* Quantitative functional lung imaging with synchrotron radiation using inhaled xenon as contrast agent. *Phys. Med. Biol.* **46**, 3287–3299 (2001).

98. Widder, E. A. Bioluminescence. in *Adaptive Mechanisms in the Ecology of Vision* (eds. Archer, S. N., Djamgoz, M. B. A., Loew, E. R., Partridge, J. C. & Vallerga, S.) 555–581 (Springer Netherlands, 1999). doi:10.1007/978-94-017-0619-3_19.

99. Fleiss, A. & Sarkisyan, K. S. A brief review of bioluminescent systems (2019). *Curr. Genet.* **65**, 877–882 (2019).

100. Manni, I., de Latouliere, L., Gurtner, A. & Piaggio, G. Transgenic Animal Models to Visualize Cancer-Related Cellular Processes by Bioluminescence Imaging. *Front. Pharmacol.* **10**, (2019).

101. Sekar, T. V. & Paulmurugan, R. Chapter 6 - Bioluminescence Imaging of Cancer Therapy. in *Cancer Theranostics* (eds. Chen, X. & Wong, S.) 69–93 (Academic Press, 2014). doi:10.1016/B978-0-12-407722-5.00006-2.

102. Zellproliferationsreagenz CELLPRORO. *Sigma-Aldrich* https://www.sigmaaldrich.com/catalog/product/roche/cellproro.

103. Franken, N. A. P., Rodermond, H. M., Stap, J., Haveman, J. & van Bree, C. Clonogenic assay of cells in vitro. *Nat. Protoc.* **1**, 2315–2319 (2006).

104. Brun, F. *et al.* SYRMEP Tomo Project: a graphical user interface for customizing CT reconstruction workflows. *Adv. Struct. Chem. Imaging* **3**, 4 (2017).

105. Paganin, D., Mayo, S. C., Gureyev, T. E., Miller, P. R. & Wilkins, S. W. Simultaneous phase and amplitude extraction from a single defocused image of a homogeneous object. *J. Microsc.* **206**, 33–40 (2002).

106. Klein, S., Staring, M., Murphy, K., Viergever, M. A. & Pluim, J. P. W. elastix: A Toolbox for Intensity-Based Medical Image Registration. *IEEE Trans. Med. Imaging* **29**, 196–205 (2010).

107. Shamonin, D. P. *et al.* Fast Parallel Image Registration on CPU and GPU for Diagnostic Classification of Alzheimer's Disease. *Front. Neuroinformatics* **7**, (2014).

108. Brown, M. B. & Forsythe, A. B. Robust Tests for the Equality of Variances. *J. Am. Stat. Assoc.* **69**, 364–367 (1974).

109. Olejnik, S. F. & Algina, J. Type I Error Rates and Power Estimates of Selected Parametric and Nonparametric Tests of Scale. *J. Educ. Stat.* **12**, 45–61 (1987).

110. Kruskal, W. H. & Wallis, W. A. Use of Ranks in One-Criterion Variance Analysis. *J. Am. Stat. Assoc.* **47**, 583–621 (1952).

111. Reinhardt, O. Untersuchungen zur Chemotherapieresistenz von H8N8-Tumorzellen nach Cyclophosphamid-, Doxorubicin- und 5-Fluouraciltherapie im syngenen WAP-T-Mammakarzinom-Mausmodell. (Georg-August-Universität Göttingen, 2019).

112. Brun, F. *et al.* Single-shot K-Edge Subtraction X-ray discrete Computed Tomography (KES-CT) with a polychromatic source and the Pixie-III detector. **14**, 8 (2015).

113. Albers, J. *et al.* Elastic transformation of histological slices allows precise co-registration with microCT data sets for a refined virtual histology approach. *Sci. Rep.* (2021) doi:10.21203/rs.3.rs-208394/v1.

114. Anderson, W., Harthill, J. E., James, W. B. & Montgomery, D. Barium sulphate preparations for use in double contrast examination of the upper gastrointestinal tract. *Br. J. Radiol.* **53**, 1150–1159 (1980).

115. O'Connor, S. D. & Summers, R. M. Revisiting Oral Barium Sulfate Contrast Agents. *Acad. Radiol.* **14**, 72–80 (2007).

116. Meagher, M. J. *et al.* Dextran-encapsulated barium sulfate nanoparticles prepared for aqueous dispersion as an X-ray contrast agent. *J. Nanoparticle Res.* **15**, 2146 (2013).

117. Ashton, J. R., West, J. L. & Badea, C. T. In vivo small animal micro-CT using nanoparticle contrast agents. *Front. Pharmacol.* **6**, (2015).

118. Hainfeld, J. F., Smilowitz, H. M., O'Connor, M. J., Dilmanian, F. A. & Slatkin, D. N. Gold nanoparticle imaging and radiotherapy of brain tumors in mice. *Nanomed.* **8**, 1601–1609 (2013).

119. Toward an Image-Guided Microbeam Radiation Therapy Using Gadolinium-Based Nanoparticles | ACS Nano. https://pubs.acs.org/doi/abs/10.1021/nn202797h.

120. Maggiorella, L. *et al.* Nanoscale radiotherapy with hafnium oxide nanoparticles. *Future Oncol. Lond. Engl.* **8**, 1167–1181 (2012).

121. Choi, G.-H. *et al.* Photon activated therapy (PAT) using monochromatic Synchrotron x-rays and iron oxide nanoparticles in a mouse tumor model: feasibility study of PAT for the treatment of superficial malignancy. *Radiat. Oncol.* **7**, 184 (2012).

122. Gianfaldoni, S. *et al.* An Overview on Radiotherapy: From Its History to Its Current Applications in Dermatology. *Open Access Maced. J. Med. Sci.* **5**, 521–525 (2017).

123. Castro Pena, P. *et al.* Anatomical, clinical and radiological delineation of target volumes in breast cancer radiotherapy planning: individual variability, questions and answers. *Br. J. Radiol.* **82**, 595–599 (2009).

124. Yin, Y. *et al.* Dosimetric research on intensity-modulated arc radiotherapy planning for left breast cancer after breast-preservation surgery. *Med. Dosim.* **37**, 287–292 (2012).

125. Thoms, J. & Bristow, R. G. DNA repair targeting and radiotherapy: a focus on the therapeutic ratio. *Semin. Radiat. Oncol.* **20**, 217–222 (2010).

126. Choudhary, S. Deterministic and Stochastic Effects of Radiation. *Cancer Ther. Oncol. Int. J.* **12**, 31–32 (2018).

127. Pottier, A., Borghi, E. & Levy, L. The future of nanosized radiation enhancers. *Br. J. Radiol.* **88**, (2015).

128. Herskind, C., Griebel, J., Kraus-Tiefenbacher, U. & Wenz, F. Sphere of Equivalence—A Novel Target Volume Concept for Intraoperative Radiotherapy Using Low-Energy X Rays. *Int. J. Radiat. Oncol.* **72**, 1575–1581 (2008).

129. Wang, R. *et al.* Barium tungstate nanoparticles to enhance radiation therapy against cancer. *Nanomedicine Nanotechnol. Biol. Med.* **28**, 102230 (2020).

130. Zhang, M. *et al.* Radiation-assisted metal ion interference tumor therapy by barium peroxide-based nanoparticles. *Mater. Horiz.* **6**, 1034–1040 (2019).

131. Hainfeld, J. F., Slatkin, D. N. & Smilowitz, H. M. The use of gold nanoparticles to enhance radiotherapy in mice. *Phys. Med. Biol.* **49**, N309–N315 (2004).

132. Al Zaki, A. *et al.* Gold-Loaded Polymeric Micelles for Computed Tomography-Guided Radiation Therapy Treatment and Radiosensitization. *ACS Nano* **8**, 104–112 (2014).

133. Rehemtulla, A. *et al.* Rapid and Quantitative Assessment of Cancer Treatment Response Using In Vivo Bioluminescence Imaging. *Neoplasia N. Y. N* **2**, 491–495 (2000).

134. Thorne, N., Inglese, J. & Auld, D. S. Illuminating insights into firefly luciferase and other bioluminescent reporters used in chemical biology. *Chem. Biol.* **17**, 646–657 (2010).

135. Czupryna, J. & Tsourkas, A. Firefly Luciferase and Rluc8 Exhibit Differential Sensitivity to Oxidative Stress in Apoptotic Cells. *PLoS ONE* **6**, (2011).

136. Coulter, J. A., Hyland, W. B., Nicol, J. & Currell, F. J. Radiosensitising nanoparticles as novel cancer therapeutics--pipe dream or realistic prospect? *Clin. Oncol. R. Coll. Radiol. G. B.* **25**, 593–603 (2013).

137. Lechtman, E. *et al.* A Monte Carlo-based model of gold nanoparticle radiosensitization accounting for increased radiobiological effectiveness. *Phys. Med. Biol.* **58**, 3075–3087 (2013).

138. Douglass, M., Bezak, E. & Penfold, S. Monte Carlo investigation of the increased radiation deposition due to gold nanoparticles using kilovoltage and megavoltage photons in a 3D randomized cell model. *Med. Phys.* **40**, 071710 (2013).

139. Mundt, A. J., Roeske, J. C., Chung, T. D. & Weichselbaum, R. R. Physical Basis of Radiation Therapy. *Holl.-Frei Cancer Med. 6th Ed.* (2003).

140. Osta, W. A. *et al.* EpCAM is overexpressed in breast cancer and is a potential target for breast cancer gene therapy. *Cancer Res.* **64**, 5818–5824 (2004).

141. Attarwala, H. Role of antibodies in cancer targeting. *J. Nat. Sci. Biol. Med.* **1**, 53–56 (2010).

142. Hernández-Camarero, P. *et al.* Clinical failure of nanoparticles in cancer: mimicking nature's solutions. *Nanomed.* **15**, 2311–2324 (2020).

143. Anselmo, A. C. & Mitragotri, S. Nanoparticles in the clinic: An update. *Bioeng. Transl. Med.* **4**, (2019).

144. Shi, Y., van der Meel, R., Chen, X. & Lammers, T. The EPR effect and beyond: Strategies to improve tumor targeting and cancer nanomedicine treatment efficacy. *Theranostics* **10**, 7921–7924 (2020).

145. Dasgupta, A., Biancacci, I., Kiessling, F. & Lammers, T. Imaging-assisted anticancer nanotherapy. *Theranostics* **10**, 956–967 (2020).

146. Ray, K. Clearance of nanomaterials in the liver. *Nat. Rev. Gastroenterol. Hepatol.* **13**, 560–560 (2016).

147. Baboci, L. *et al.* The Dual Role of the Liver in Nanomedicine as an Actor in the Elimination of Nanostructures or a Therapeutic Target. *J. Oncol.* **2020**, e4638192 (2020).

148. Oswald, P., Clement, O., Chambon, C., Schouman-Claeys, E. & Frija, G. Liver positive enhancement after injection of superparamagnetic nanoparticles: Respective role of circulating and uptaken particles. *Magn. Reson. Imaging* **15**, 1025–1031 (1997).

149. Boll, H. *et al.* Micro-CT Based Experimental Liver Imaging Using a Nanoparticulate Contrast Agent: A Longitudinal Study in Mice. *PLOS ONE* **6**, e25692 (2011).

150. Wang, H. *et al.* Diagnostic imaging and therapeutic application of nanoparticles targeting the liver. *J. Mater. Chem. B* **3**, 939–958 (2015).

151. Monitoring macrophage migration in the liver in vivo with Contrast Enhanced micro CT. http://www.wmis.org/abstracts/2013/data/papers/SS126.htm.

152. Tsoi, K. M. *et al.* Mechanism of hard-nanomaterial clearance by the liver. *Nat. Mater.* **15**, 1212–1221 (2016).

153. Oskarsson, A. Chapter 29 - Barium. in *Handbook on the Toxicology of Metals (Fourth Edition)* (eds. Nordberg, G. F., Fowler, B. A. & Nordberg, M.) 625–634 (Academic Press, 2015). doi:10.1016/B978-0-444-59453-2.00029-9.

154. Heintzmann, R. & Ficz, G. Chapter 22 - Breaking the Resolution Limit in Light Microscopy. in *Methods in Cell Biology* (eds. Sluder, G. & Wolf, D. E.) vol. 114 525–544 (Academic Press, 2013).

155. Ohnishi, T. *et al.* Deformable image registration between pathological images and MR image via an optical macro image. *Pathol. - Res. Pract.* **212**, 927–936 (2016).

156. Rueckert, D. *et al.* Nonrigid registration using free-form deformations: application to breast MR images. *IEEE Trans. Med. Imaging* **18**, 712–721 (1999).

157. Čapek, M. *et al.* Volume reconstruction of large tissue specimens from serial physical sections using confocal microscopy and correction of cutting deformations by elastic registration. *Microsc. Res. Tech.* **72**, 110–119 (2009).

158. Chiang, C.-S. *et al.* Irradiation Promotes an M2 Macrophage Phenotype in Tumor Hypoxia. *Front. Oncol.* **2**, (2012).

159. Milross, C. G. *et al.* The Effect of Tumor Size on Necrosis and Polarographically Measured pO_2. *Acta Oncol.* **36**, 183–189 (1997).

160. Kuroe, T. *et al.* Evaluation of the morphological features and unfavorable prognostic impact of dirty necrosis in renal cell carcinoma. *J. Cancer Res. Clin. Oncol.* **147**, 1089–1100 (2021).

161. Kwatra, D., Venugopal, A. & Anant, S. Nanoparticles in radiation therapy: a summary of various approaches to enhance radiosensitization in cancer. *Transl. Cancer Res.* **2**, (2013).

162. Costa, R. *et al.* Targeting Epidermal Growth Factor Receptor in triple negative breast cancer: New discoveries and practical insights for drug development. *Cancer Treat. Rev.* **53**, 111–119 (2017).

163. Chakravarti, A., Dicker, A. & Mehta, M. The contribution of epidermal growth factor receptor (EGFR) signaling pathway to radioresistance in human gliomas: a review of preclinical and correlative clinical data. *Int. J. Radiat. Oncol. Biol. Phys.* **58**, 927–931 (2004).

164. Ping, Y. *et al.* Inhibition of the EGFR with nanoparticles encapsulating antisense oligonucleotides of the EGFR enhances radiosensitivity in SCCVII cells. *Med. Oncol. Northwood Lond. Engl.* **27**, 715–721 (2010).

165. Kutova, O. M., Guryev, E. L., Sokolova, E. A., Alzeibak, R. & Balalaeva, I. V. Targeted Delivery to Tumors: Multidirectional Strategies to Improve Treatment Efficiency. *Cancers* **11**, (2019).

166. Palanikumar, L. *et al.* pH-responsive high stability polymeric nanoparticles for targeted delivery of anticancer therapeutics. *Commun. Biol.* **3**, 1–17 (2020).

167. Hennessey, D. *et al.* Exposure to hypoxia following irradiation increases radioresistance in prostate cancer cells. *Urol. Oncol. Semin. Orig. Investig.* **31**, 1106–1116 (2013).

168. Klein, C. *et al.* Overcoming hypoxia-induced tumor radioresistance in non-small cell lung cancer by targeting DNA-dependent protein kinase in combination with carbon ion irradiation. *Radiat. Oncol.* **12**, 208 (2017).

169. Song, C. W., Shakil, A., Osborn, J. L. & Iwata, K. Tumour oxygenation is increased by hyperthermia at mild temperatures. *Int. J. Hyperthermia* **25**, 91–95 (2009).

170. Kennedy, L. C. *et al.* A New Era for Cancer Treatment: Gold-Nanoparticle-Mediated Thermal Therapies. *Small* **7**, 169–183 (2011).

171. Self, C. H. & Thompson, S. Light activatable antibodies: Models for remotely activatable proteins. *Nat. Med.* **2**, 817–820 (1996).

Acknowledgements

The here presented thesis would not have been possible without the great supervision and endless support of my supervisor Prof. Dr. Frauke Alves. She always gave helpful suggestions, ideas and input on how to perform and optimize the presented experiments, while at the same time allowing me to pursue my own ideas.

I also would like to acknowledge the members of my Thesis Committee, Prof. Dr. Dörthe M. Katschinski and Prof. Dr. Hubertus Jarry for participating in my PhD thesis committee meetings and for the nice and fruitful discussions of my data and experiments.

The biggest thanks must go to PD Dr. Christian Dullin, who is not only a great mentor and teacher but has also become a good friend in the last years. He always offered his extensive knowledge and endless patience to solve any problem that I was confronted with on my way to completing my thesis.

In addition, I would also like to thank all the people who contributed to this work, without your help this would not have been possible. I would like to thank Bärbel Heidrich for her great help in cell culture and animal experiments. Sabine Wolfgramm and Bettina Jeep for excellent help in histological sectioning and staining, as well as Sarah Garbode and Regine Kruse for assistance in the animal experiments. I would also like to thank everyone else in the AG Alves, especially Dr. Andrea Markus for helpful discussions to plan my experiments and tireless help in writing various publications. I also want to thank Dr. Joanna Napp and Jakub Mitrega for providing me with the bioluminescent breast cancer cells as well as for always having a friendly ear for me. Another thank you goes to Dr. Fernanda Ramos-Gomes for her assistance in confocal microscopy. Dr. Giuliana Tromba also deserves a special acknowledgement for assisting with the synchrotron measurements, as well as Marius Reichardt for performing XRF measurements. Another thank you needs to go to Dr. Alexander Kraupner and the whole team of nanoPET pharma for providing the nanoparticles that were used in my thesis.

I would also like to display my gratitude to Prof. Joachim Lotz and the whole department of Diagnostic and Interventional Radiology for letting me become a member of the department.

A special thank you goes to Angelika Svetlove, who came to our group for a lab rotation and who I can now proudly call my best friend.

Finally, I would like to thank my family and close friends, who always supported my journey to becoming a researcher.